BIAXIAL MECHANICAL TESTING OF NATIVE AND GLYCOSAMINOGLYCAN-DEPLETED PORCINE AORTIC WALL

by

DAYNA ZUNDER

Thesis submitted to the University of Ottawa
in partial fulfillment of the requirements for the
Master of Applied Science in Biomedical Engineering

The Ottawa-Carleton Institute for Biomedical Engineering
University of Ottawa
November 2021

Abstract

A recent focus in the biomedical engineering field has been on developing models of *in-vivo* tissue responses to help better predict aortic wall mechanics, through numerical methods and simulation, towards improved prediction of aortic wall rupture. The structural influence of both collagen and elastin, integral components within the aortic wall, has been studied and is largely understood, but the contribution of glycosaminoglycans (GAGs) is still unclear. While it has been suggested that the swelling properties of GAGs may participate in the regulation of residual stresses in the aortic wall, whether or not GAGs affect the mechanical properties of the aortic wall is completely unknown. The present study was divided into two experiments: Experiment 1 ($n=9$) utilized planar biaxial testing to characterize arterial wall mechanics in native porcine aortas. The results of Experiment 1 highlight: (i) decreased tissue thickness moving distally, away from the heart; (ii) increased stiffness from the ascending aorta to the thoracic descending aorta; (iii) no difference in morphometry or stress-strain behaviour between samples excised from the anterior, posterior, and/or left and right lateral walls. Experiment 2 ($n=8$) employed identical testing parameters to characterize partial and fully enzymatically GAG-depleted tissue, to determine the influence of this macromolecule on aortic wall mechanics. The results of Experiment 2 highlight: (i) GAG content in the porcine aorta does not affect tissue mechanical properties measured from biaxial testing; (ii) enzymatic removal of GAGs does not influence morphometric parameters, including thickness and area. These findings will contribute to improving the fundamental understanding of aortic tissue mechanics by helping to determine the relationship between spatial dependency and mechanical response, and the relationship between individual aortic wall constituents and the overall mechanical behaviour of the aorta.

Résumé

Dans le domaine du génie mécanique biomédical, le développement de modèles pour les tissus *in-vivo* a reçu récemment beaucoup d'attention pour aider à prévoir le comportement mécanique de la paroi aortique, avec des méthodes numériques et des simulations, afin d'améliorer la prédiction des ruptures. L'influence structurelle du collagène et de l'élastine, des composantes intégrales de la paroi aortique, est bien comprise, mais la contribution des glycosaminoglycanes (GAGs) n'est pas encore claire. Bien qu'il ait été suggéré que les propriétés de gonflement des GAGs puissent participer à la régulation des contraintes résiduelles dans la paroi aortique, la contribution des GAGs aux propriétés mécaniques de la paroi aortique est complètement inconnue. L'étude présente a été divisée en deux expériences: l'expérience 1 ($n = 9$) a utilisé des essais biaxiaux plans pour caractériser le comportement mécanique de la paroi aortique dans les aortes porcines natives. Les résultats de l'expérience 1 démontrent: (i) une diminution distale de l'épaisseur des tissus; (ii) une augmentation de la rigidité entre l'aorte ascendante à l'aorte thoracique descendante; (iii) aucune différence de morphométrie ou du comportement contrainte-déformation entre les tissus des parois latérales antérieure, postérieure et/ou gauche et droite. L'expérience 2 ($n = 8$) a utilisé les mêmes paramètres d'essais pour caractériser des tissus dont les GAGs étaient partiellement ou entièrement digérés, afin de déterminer l'influence de ces macromolécules sur le comportement mécanique de la paroi aortique. Les résultats de l'expérience 2 indiquent que: (i) la teneur en GAGs dans l'aorte porcine n'affecte pas les propriétés mécaniques des tissus mesurées à partir des essais biaxiaux; (ii) l'élimination enzymatique des GAGs n'influence pas les paramètres morphométriques, incluant l'épaisseur et la surface. Ces résultats contribueront à améliorer la compréhension fondamentale de la mécanique des tissus aortiques en aidant à déterminer la relation entre la dépendance spatiale et la réponse mécanique, et la relation entre les constituants individuels de la paroi aortique et le comportement mécanique global de l'aorte.

Acknowledgements

First and foremost, I would like to express my sincere gratitude to my supervisors, Dr. Michel Labrosse and Dr. Jean-Philippe St-Pierre. Over the last two years, their expertise, input and dedication to my project were invaluable. A heartfelt thank you for their patience, guidance and unwavering support.

Special thanks go to my lab-mates in the St-Pierre Biomaterials Group for contributing their experience and know-how in the lab. Noor Ghadie, thank you for dedicating your time to patiently teach me both in and out of the lab, for listening to my late-night rants, and for your advice, wisdom and friendship.

Lastly, it is my privilege to thank my family: my mother and father, Karen and Ian, for their unyielding support, encouragement, and love (especially on my moody days), my brothers, Jordan and Adam, for setting the bar high, my grandparents, John and Gladys, for inspiring me to pursue engineering, and my Bubbie Lillian, for our daily chats and everything in between. This small milestone is dedicated to you.

Table of Contents

List of Figures

List of Tables

1 Introduction

According to the World Health Organization, cardiovascular diseases (CVDs) are the leading cause of death globally, with an estimated 31% of all deaths worldwide (World Health Organization, 2017). These CVDs refer to conditions that affect heart structure, function, and blood vessels. In particular, ruptured aortic aneurysms and dissections are life threatening pathologies with a mortality rate thought to exceed 90% (Jonker et al., 2010). Current interventions for aortic aneurysm include monitoring yearly expansion rates and surgical treatment recommended with aneurysm diameter > 5.5 cm; these approaches are not considered adequate (Carpenter & Best, 2013) as many ruptures occur suddenly and below clinical guidelines for treatment. Hence, standards of medical care are shifting from a curative to a preventative approach by adopting an evidence-based medicine practice. A recent focus in the biomedical engineering field has been on developing models of *in-vivo* tissue responses to help better predict aortic wall mechanics through numerical methods and simulation towards improved prediction of aortic wall rupture.

The structural influence of both collagen and elastin, integral components within the aortic wall, has been studied and is largely understood, but the contribution of glycosaminoglycans (GAGs) is still unclear. While it has been suggested that the swelling properties of GAGs may participate in the regulation of residual stresses in the arterial wall—stresses essential in maintaining aortic homeostasis and developed to reduce stress gradients across the wall (Azeloglu et al., 2008; Chuong & Fung, 1986), whether or not GAGs affect the mechanical properties of the aortic wall is completely unknown. Therefore, the current study aims to investigate the influence of GAGs on the mechanical behaviour of the porcine aorta. The porcine aorta is used as a model for translational research on the human aorta because of their similar anatomical and physiological

features (de Beaufort et al., 2018). While significant structural and material differences have been observed between the porcine and aged human aorta, due to underlying mechanisms that govern alterations in stiffness and age, such as extracellular matrix (ECM) remodelling, the young porcine aorta shows good correspondence with young healthy human tissue.

While the possible link between the aortic wall components, including GAGs, and residual stresses is currently under detailed investigation in a different research project by the same laboratory, the tissue preparation necessary for biaxial testing used in the present work destroys the native circular shape of the aortic wall, and therefore makes it is impossible to assess the residual stresses that may exist in the unloaded aorta.

The present study hypothesises that GAG content in the porcine aorta does not affect tissue mechanical properties measured from biaxial testing. To test this hypothesis, we will: (i) characterize arterial wall mechanics in native porcine aortas using planar biaxial testing; (ii) repeat the characterization for partially and fully enzymatically GAG-depleted tissue, to determine the influence of this macromolecule on arterial wall mechanics. In addition, possible regional and directional variations in stress-strain behaviour of the porcine aorta will be investigated.

These findings will contribute to improving the fundamental understanding of aortic tissue mechanics by helping to determine the relationship between individual aortic wall constituents and the overall mechanical behaviour of the aorta.

2 Literature Review

The following chapter was used to analyze and assess published literature on the structure and function of the aorta, cardiovascular mechanics and soft tissue behaviour.

2.1 The Cardiovascular System

The primary function of the cardiovascular system is mass transport within the body which is mediated by the heart in a coordinated and continuous effort to circulate oxygen, carbon dioxide, nutrients and waste products. The cardiovascular system consists of three components: (i) the heart, the central muscular pump; (ii) the vasculature, the network through which the blood flows to all parts of the body and; (iii) the blood, the conducting medium (Humphrey & McCulloch, 2003). Furthermore, the vasculature is divided into three major categories: (i) arteries, vessels which transport blood away from the heart to the body; (ii) veins, which carry blood from the body to the heart; (iii) and capillaries, microscopic vessels which connect arteries and veins. This review is focused on the largest vessel in the body, the main systemic artery, the aorta (Figure 1).

2.2 Anatomy and Physiology of the Aorta

As the largest vessel in the body, the aorta's main function is to carry oxygen-rich blood from the left ventricle of the heart to the systemic circulation system, supplying organs, tissues and cells. The aorta acts as a pressure reservoir and the cardiac cycle is defined by two phases: systole and diastole. The former includes left ventricular contraction, causing ventricular pressure to increase rapidly, resulting in the opening of the aortic valve, while the latter is defined by relaxation following contraction. The blood flow through the aorta causes it to expand and pressure to rise (Guyton, 1981). Initially, expansion is limited to the proximal portion of the aorta due to the inertia of blood, which prevents movement of blood into peripheral arteries on the arterial tree. As

pressure increases, distal portions of the aorta become distended (Ganong, 1981). At the end of systole, elastic recoil maintains pressure within the aorta, even during diastole (Guyton, 1981).

The aorta can be divided into major anatomical regions including: the aortic root, the ascending aorta (Asc.), the aortic arch (Arc.) and the descending aorta (Tho.); the latter includes the thoracic descending and the abdominal aorta (Collins et al., 2014), refer to Figure 1. The aortic root includes the aortic valve and aortic sinuses, and is defined as the segment between the ventriculo-arterial attachment and the sinotubular junction (STJ) (Ladich et al., 2016). The ascending aorta originates at the STJ, below which the coronary arteries branch off the aortic sinuses to supply oxygenated blood to the cardiac tissue, and ends at the ostium of the brachiocephalic artery, commonly referred to as the innominate artery (Collins et al., 2014). The aortic arch makes a cane-shaped curve that begins at the brachiocephalic artery and ends at the aortic isthmus, a section just distal to the origin of the left subclavian artery (Kelley et al., 2021). In humans, the aortic arch contains three major branches: the brachiocephalic trunk, which bifurcates into the right subclavian and the right common carotid artery, the left common carotid artery and the left subclavian artery; the first, second, and third branches along the aortic arch, respectively (Guyton, 1981). The aforementioned branches provide oxygen-rich blood to the upper extremities, including the head, neck and arms (Collins et al., 2014; Kelley et al., 2021). The thoracic descending aorta is the continuation of the aortic arch; it begins distal to the aortic isthmus and terminates at the aortic hiatus, the crux of the diaphragm. Branches from the thoracic descending aorta include bronchial arteries, supplying oxygenated blood to various chest structures, and the third through eleventh posterior intercostal arteries. The first and second intercostal arteries originate from the highest intercostal artery, which arises from the costocervical trunk, a branch off the subclavian artery (Collins et al., 2014; Cramer, 2014). The

abdominal aorta extends from the diaphragm to the aortic bifurcation into the left and right common iliac arteries (Teo & Isselbacher, 2019), providing oxygenated blood to abdominal organs and lower extremities.

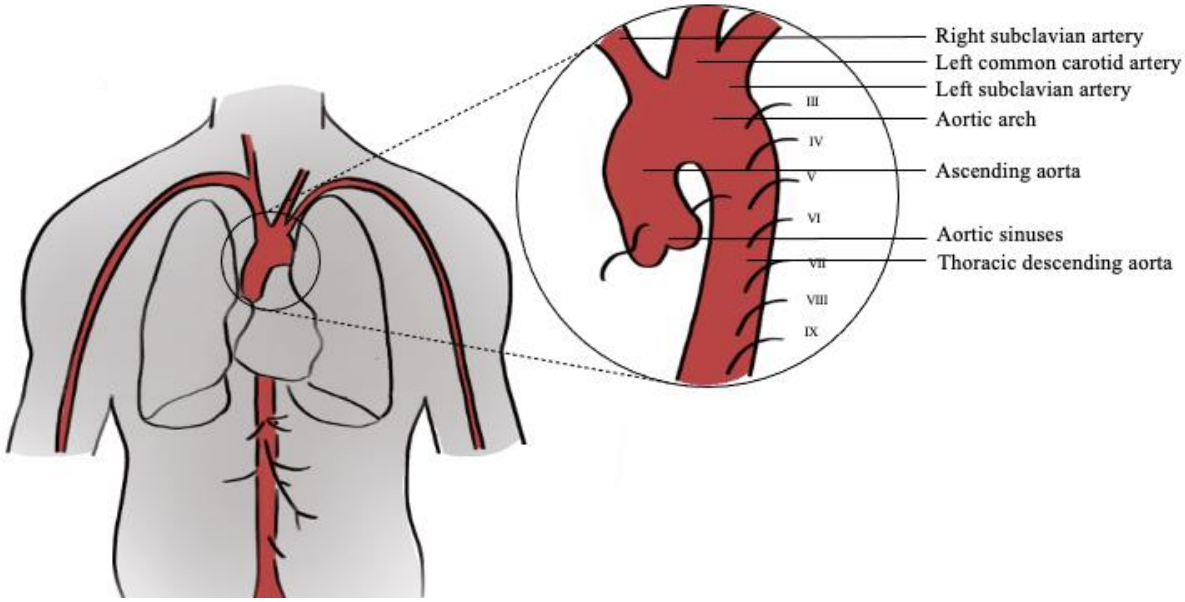

Figure 1 – Anatomy of the aorta: Anatomically relevant regions including the ascending aorta, aortic arch and thoracic descending are identified. Roman numerals are used to denote posterior intercostal arteries. Images adapted from (Mayo Clinic, 2016; UAB Medicine, n.d.).

2.3 The Normal Arterial Wall

Arteries are categorized into two groups: elastic and muscular. Elastic arteries are found closer to the heart and are typically larger in diameter, while muscular arteries tend to be smaller-diameter vessels located at the periphery, closer to the arterioles (Cowin & Humphrey, 2001; Humphrey, 2002). The main systemic artery, the aorta, is classified as elastic; the vessel's wall composition provides the mechanical properties essential for regulating left ventricular performance, myocardial perfusion and arterial function (Sokolis, 2007). The composition, microstructure and biomechanical behaviour of the arterial wall varies with location along the vascular tree (Humphrey, 2002). Fiber distribution and orientation of ECM components are associated with unique mechanical behaviour and response (Holzapfel et al., 2000). Regardless of location and

artery type, the microscopic structure of arterial walls consists of three distinct tissue layers: (i) tunica intima; (ii) tunica media; (iii) and tunica adventitia, Figure 2. A detailed description of each of these layers is provided below.

2.3.1 The Intima

The intima is the innermost and thinnest layer of the vascular wall, accounting for <1% of total wall thickness (Jana et al., 2019). Its microscopic structure and composition includes a monolayer of endothelial cells (ECs), resting on a basement membrane (*basal lamina*) (Holzapfel et al., 2000). ECs are flat cells oriented in the direction of blood flow, with the exception of bifurcations where blood flow is complex; shape and size of ECs varies along the length of the vascular tree, but generally these cells are approximately 0.1 to 10 μm thick, specifically 1 μm in the aorta (Aird, 2007), 10 to 30 μm wide, and 50 to 70 μm long, and line the interior surface of the vessel (Félétou, 2011; Humphrey, 2002). The intima serves as a semi-permeable barrier between the vessel wall and blood; permitting some small molecules to cross, according to concentration gradients, while the passage of larger molecules and cells may only occur via vesicles and receptors, or damaged endothelial junctions (Mundi et al., 2018). Furthermore, the endothelial layer aids with coagulation and inflammation regulation (Brown et al., 2017). The basement membrane is a highly specialized ECM network composed mainly of type IV collagen, laminin, fibronectin, perlecan and heparan sulfate proteoglycans (Humphrey, 2002; Jana et al., 2019), within which GAGs represent approximately 0.56% dry tissue weight (Katsumi Murata et al., 1975). While the basement membrane does not contribute to the structural support of the arterial wall, it provides an instructive support which facilitates adhesion of ECs, permitting growth, and regulates migration, proliferation and cell survival (Jana et al., 2019). In young healthy individuals, the tunica intima

is so thin that its contribution to solid mechanics and arterial wall behaviour is considered negligible (Holzapfel et al., 2000).

2.3.2 The Media

The intima and media are separated by the internal elastic lamina (IEL), which serves as an interface between the two layers, and is often considered a component of the media (Jana et al., 2019). The media is the middle layer of the arterial wall and consists of a three-dimensional network of smooth muscle cells (SMCs) embedded in an extracellular network of elastin and collagen fibrils (types I, III and V) (Holzapfel et al., 2000; Humphrey, 2002). Morphology of arterial SMCs are species-specific, such that SMCs derived from the porcine aortic media exhibit a spindle-shaped phenotype, while SMCs from young human aorta (25-60 years) are elongated, asymmetric, polygonal and stellate (Hao et al., 2003). The SMCs are approximately 200 μm long and 5 μm in diameter (Wilson, 2011); these cells are oriented circumferentially, within the concentric elastic laminae, which are approximately 5 to 15 μm thick layers, separated by 3 μm thick fenestrated elastin sheets. Approximately 40-70 concentric layers of SMCs and elastic laminae are present in the elastic artery medial layer (Humphrey, 2002). Medial fibers are also oriented nearly circumferentially, providing structural support (specifically collagen type I and III) to tolerate high systemic pressures of left ventricle contraction (Jana et al., 2019). The concentration of glucuronic acid in the media is approximately 0.39% by dry weight, indicating GAG concentration decreases from the intima to the media (Katsumi Murata et al., 1975). In terms of biomechanical influence, the media is considered the most significant arterial layer (Holzapfel et al., 2000).

2.3.3 The Adventitia

The external elastic lamina (EEL) acts as a barrier between the media and the adventitia, the outermost layer, which comprises approximately 10% of the arterial wall in elastic arteries (Holzapfel et al., 2000). The adventitia is composed mainly of fibroblasts (FBs), fibrocytes, elastin fibrils, a network of type I collagen fibers, nerves and the vasa vasorum, which produce a fibrous tissue outer layer (Holzapfel et al., 2000; Humphrey, 2002). FBs aid in regulating type I collagen connective tissue, while the vasa vasorum is responsible for transporting gases, nutrients, waste and metabolites from the inner surface to the adventitia. Undulated collagen fibrils form helical structures, which contribute to the structural integrity and stability of the artery. The concentration of GAGs in the outermost layer is approximately 0.30% by dry weight (Katsumi Murata et al., 1975).

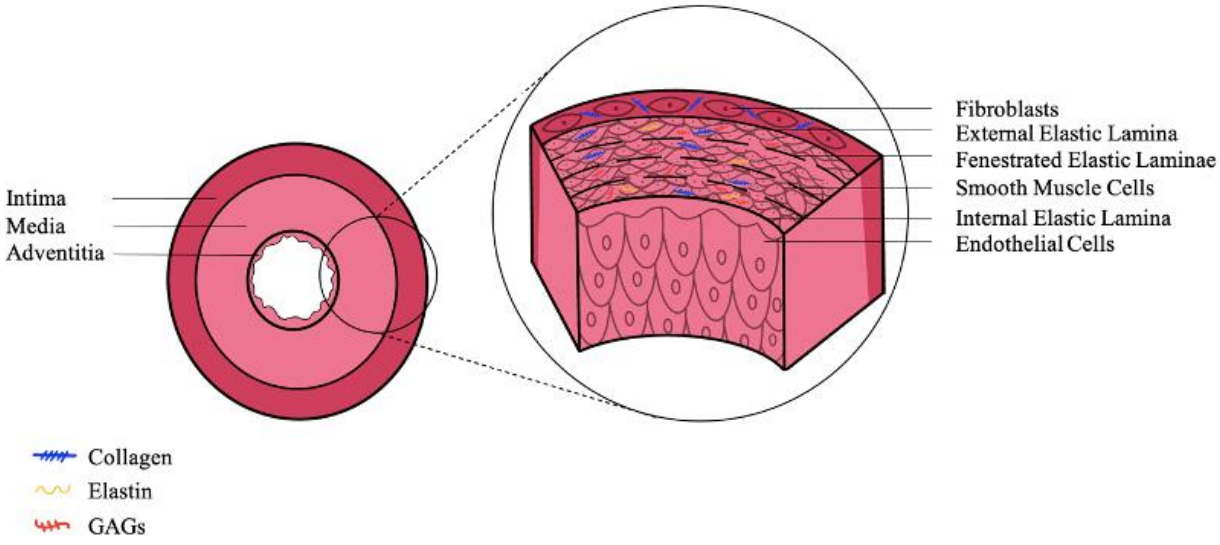

Figure 2 – Model of the major components of the elastic artery, composed of three layers the (i) intima, (ii) media, (iii) adventitia.

2.4 The Extracellular Matrix

The ECM is the non-cellular component of tissue, composed primarily of a highly hydrated plexus of proteins and polysaccharides (Frantz et al., 2010). Vascular wall ECM is composed of two main

types of macromolecules: proteoglycans (PGs) and fibrous proteins (Frantz et al., 2010). PGs are defined as GAG chains covalently bound to a protein core, while fibrous proteins include collagen and elastin. These macromolecules compose approximately 2-5% and 50% of the dry weight of larger arteries, respectively (Jana et al., 2019; Wight, 1980). Typically, tissues subjected to large compressive forces are proteoglycan-laden, as high water content aids in the resistance to compression, while tissues that withstand large tensional forces contain high levels of collagen, which increase tissue stiffness (Ayad et al., 1998).

Functions of tissue ECM include endowing the tissue with biomechanical characteristics, including compressive and tensile strength, maintaining tissue shape, providing a scaffold on which cells can adhere, proliferate, and differentiate, and providing an aqueous medium. This medium permits the diffusion of nutrients, waste, hormones and metabolites in and out of the tissue. Cell signaling helps regulate tissue homeostasis and remodelling throughout life, through controlled secretion and degradation (Frantz et al., 2010; Humphrey, 2002).

Based on continuum mechanics theory, the intrinsic mechanical properties of a material are based on the quantity, distribution, orientational, and intercellular junctions of its internal constituents (Humphrey, 2002). Variations in the composition and organization of the ECM result in differences in both structure and function of the tissue. The following section discusses the major non-cellular components of the ECM, which contribute to the maintenance, structure and function of aortic wall mechanics, including collagen, elastin and GAGs.

2.4.1 Collagen

Collagen is the most abundant protein in the body, accounting for approximately 25-30% of all proteins, with common forms within the human aortic vascular wall being type I, III and V, 69-91%, 20-30%, and 8-15% by dry weight of collagen, respectively (Humphrey, 2002; Jana et al.,

2019; Mccullagh & Balian, 1975; K. Murata et al., 1986; Shekhonin et al., 1985). Collagen is an inherently stiff protein; its main function is to limit vessel wall distention and overstretching, and it is responsible for providing wall support and resisting tensile forces (Avril, 2018).

Specialized groups of glycoproteins constitute collagen; whereby 28 unique types have been identified, with type I fibrillar as the most abundant. The collagen molecule is formed from a hierarchical, staged assembly to produce a triple helix composed of three polypeptide (α) chains, each with a left-handed helical configuration, wound to create a right-handed superhelix. Each α chain contains approximately 1,300 - 1,700 amino acid residues; the simplest amino acid, glycine, occupies every third residue, due to its inherently small size and ability to occupy the centre of the triple helix without distortion (Ayad et al., 1998). The triple helix is the product of repeating units of amino acids, $[Glycine\text{-}X\text{-}Y]_n$: where X and Y may be one of 19 other amino acids, however, likely proline and hydroxyproline (Ayad et al., 1998; Humphrey, 2002). Differences in the assembly stage, including different amino acids or different chains composing the triple helix, result in different types of collagen fibers with unique mechanical properties. Procollagen, the precursor to collagen, is synthesized and undergoes extracellular modifications required for alignment and self-assembly, to create functional fibers (Humphrey, 2002; Peltonen et al., 1985). The polymerization of collagen molecules form 4-8 nm diameter microfibrils, which include four to five groups of staggered and offset molecules (Humphrey, 2002). Following the formation of microfibrils, the collagen is organized into larger fibrils, approximately 10-500 nm diameter, and finally into fibers with 1-500 μm diameter (Humphrey, 2002).The non-helical ends of the collagen molecules experience intramolecular covalent cross-links which provide additional molecular structural support. Vascular collagen has a half-life of approximately 60-70 days (Martufi & Gasser, 2012), hence maintenance includes a balance between collagen synthesis and degradation.

2.4.2 Elastin

Elastin is a major constituent of the arterial wall ECM, accounting for approximately 35-50% tissue dry weight (Martyn & Greenwald, 1997; Tsamis et al., 2013), and provides the mechanical properties that permit vessel expandability and recoil. Due to the nature of elastin, fibers can undergo recoverable extensions up to 150% (relative to 10% for collagen) (Humphrey, 2002); a function of hyperelasticity, which permits elastic response even when subjected to large elastic deformations, within physiological ranges. In addition to providing resilience to the vessel wall, elastin facilitates cell adhesion and promotes proliferation (Ayad et al., 1998). Elastic fibers are extremely stable, with a half-life of 40 years. These fibers aid in maintaining proper tissue form; however, have limited repair mechanisms when damaged and/or degraded (Avril, 2018). Similar to collagen, the formation of elastin is promoted by a complex cell-mediated process. Elastin is an insoluble and hydrophobic protein, synthesized through cross-linking of its precursor, tropoelastin, a soluble and single polypeptide chain (Xu & Shi, 2014) composed of approximately 786 amino acid residues (mainly glycine, alanine and proline) (Humphrey, 2002). Within the ECM, cells secrete single chains, which interact with microfibrillar components to synthesize elastic fibers (Ayad et al. 1998). These proteins become highly cross-linked through their lysine residues, to stabilize the fibers (Frantz et al., 2010). Desmosine and isodesmosine, amino acids specific to elastic fibers, are responsible for covalent cross-linking between fibers (Ayad et al., 1998; Humphrey, 2002). The high degree of cross-linking is essential for the recoil properties of the arterial wall and is responsible for protein insolubility (Wagenseil & Mecham, 2009), producing a meshwork capable of recoverable responses with large extensions (Humphrey, 2002). Elastic fibers are complex structures which are composed of both elastin (amorphous component) and microfibrils, synthesized by SMCs within the media and FBs in the adventitia (Wagenseil &

Mecham, 2009; Xu & Shi, 2014). These fibers are deposited between the IEL and EEL where they create the lamellar unit, concentric elastic laminae between concentric rings of SMCs.

2.4.3 Cross-Linking in the ECM

Collagen and elastin cross-links within the ECM of the aortic wall are essential in providing mechanical stability of the artery. In collagen, cross-links provide tensile strength and mechanical stability, while in elastin, cross-links play an important role in elastic recoil (Brüel et al., 1998; Watanabe et al., 1996). The cross-links are mediated by the enzyme lysyloxidase, and stabilize both collagen and elastin fibers via the formation of covalent bonds (Rodriguez et al., 2008). During early growth and development, mature trivalent cross-links, pyridinoline and deoxyprydinoline, are formed between collagen, through the oxidative deamination of lysl- or hydroxylysl-residues by lysyloxidase. The deamination forms lysyl- and hydroxylysl-aldehydes, permitting the spontaneous formation of divalent cross-links, dehydro-hydroxylysinonorleucine (DHLNL) and dehydro-dihydroxylysinonoreleucine (HLNL) (Brüel et al., 1998). The concentration of mature cross-links, pyridinoline and deoxyprydinoline, tend to increase during development, providing mechanical stability to the aorta, while concentrations of DHLNL and HLNL decrease (Brüel et al., 1998); the formation and concentration of the aforementioned cross-links has been shown to vary with age and pathological condition (Brüel et al., 1998; Carmo et al., 2002; Watanabe et al., 1996). Similarly, cross-links are initiated in elastin through the oxidative deamination of lysyl-residues to lysyl-aldehydes via spontaneous condensation reactions to form desmosine and isodesmosine (Brüel et al., 1998).

The biomechanical properties of the aorta develop with age, a function of ECM remodelling. The formation of elastin cross-links in human aortas have been reported to increase in infancy, with rapid production in childhood (2-5 years), followed by a decrease in the rate of

formation in adult life (Watanabe et al., 1996); consistent with the sequence observed in short-lived species such as rats (Watanabe et al., 1996). Furthermore, decreased quantity of intralaminar elastin cross-links has also been associated with increased age, shifting mechanical behaviour from an elastin- to collagen-dominant response (Kohn et al., 2015). In addition to the lower rates of cross-link formation and decrease in cross-link quantity, major mechanical instability is associated with low turnover rate of elastin *in-vivo*, permitting the accumulation of age-related fragmentation, degradation, and progressive lysis of elastic fibers (Kohn et al., 2015); ultimately contributing to an increase in wall stiffness, limiting vessel wall distention.

Age-related amino acid changes result in decreased concentrations of desmosine and isodesmosine, and their associated cross-links (Kohn et al., 2015). In contrast to a constant elastin content with increased age (Tsamis et al., 2013), collagen concentration and cross-linking via non-enzymatic glycation increases in the aortic wall (Kohn et al., 2015). Remodelling of the rat ECM through the inhibition of collagen cross-links, via β-aminoprpionitrile, suggests that the lack of mature collagen cross-linking was responsible for arterial wall destabilization, yielding an increased aortic diameter and reduced material strength and stiffness (Brüel et al., 1998).

2.4.4 ECM Fiber Orientation

The passive mechanical properties of the aorta are determined mainly by the constituents of the arterial ECM: collagen and elastin. It is well established that the helical fibers in the aorta have a very low pitch in the luminal layers, yielding a near circumferential orientation (Driessen et al., 2004; Flamini et al., 2013; Gasser et al., 2006; Mattson & Zhang, 2017; Schriefl et al., 2012). In human aortas, two distinct fiber families exist in the arterial wall, in the intima, media and adventitia; furthermore, often a third and fourth fiber family are present in the intima in the circumferential and longitudinal directions (Schriefl et al., 2012). The orientation of medial elastin,

medial collagen and adventitial collagen fibers at 0, 5 and 10% strain are summarized in Table 1. A ratio greater than 1 indicates more circumferentially oriented fibers. Medial elastin is more longitudinally oriented at all strains, while the medial and adventitial collagen is circumferentially oriented at all strains (Mattson & Zhang, 2017).

Table 1 – Ratio of circumferentially : longitudinally oriented collagen and elastin in the porcine descending thoracic aorta, adapted from (Mattson & Zhang, 2017).

	Fiber Ratio (Circumferential/Longitudinal)		
Strain (%)	Medial Elastin	Medial Collagen	Adventitial Collagen
0	0.98	2.29	3.00
5	0.97	2.27	2.23
10	0.97	2.18	3.25

2.4.5 Proteoglycans and Glycosaminoglycans

GAGs are long chains composed of unbranched repeating disaccharide units found in the ECM of mammalian tissue (Casale & Crane, 2020; Mattson et al., 2017). As the name suggests, *glycol-* refers to galactose or a uronic sugar connected to an aminoglycan or an amino sugar (Casale & Crane, 2020). GAGs can be classified into four distinct groups: hyaluronan/hyaluronic acid (non-sulfated), chondroitin sulfate, heparan sulfate, and keratan sulfate. GAGs are highly negatively charged with a high affinity for water molecules, which provide hydration to the ECM. They serve to resist deformation and compression, retain growth factors and help bind and stabilize other ECM components (Avril, 2018). GAGs are typically not present in the ECM on their own, with the exception of hyaluronic acid (Avril, 2018), and are covalently bonded to a core protein to form proteoglycans (PGs); distinct PGs are classified by the GAG associated with the core protein. Both small and large PGs exist in the ECM and include: decorin, biglycan and fibromodulin, and aggregan, versican, neurocan and brevican, respectively (Iozzo & Schaefer, 2015).

While GAGs are present in relatively low concentrations within the arterial wall, accounting for approximately 2-5% by dry weight (Wight, 1980), they play an important role in influencing viscoelasticity and providing residual stress in the unloaded state (Azeloglu et al., 2008; Wight, 1980)—especially since the contribution of elastin in residual stress formation has recently been disputed (Azeloglu et al., 2008; Wagenseil et al., 2005). From a biomechanical perspective, residual stresses, and their associated residual strains, are the stresses that remain following the removal of external loads. These factors contribute and influence arterial homeostasis (Azeloglu et al., 2008; Mattson et al., 2017). Opening angle measurements are introduced as a method to assess the presence of significant circumferential residual stress; a closed ring tends to open, when cut radially, refer to Figure 3 (Azeloglu et al., 2008).

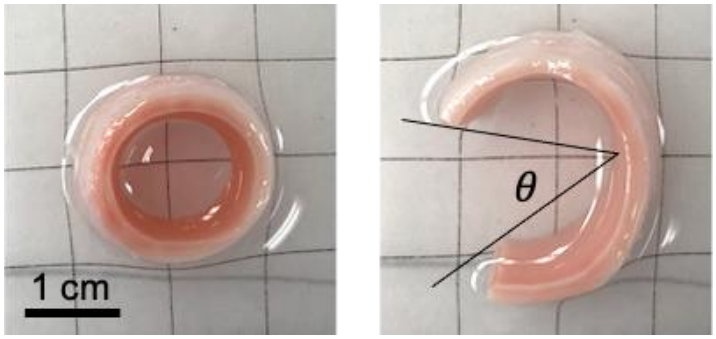

Figure 3 – Representative figure of an uncut aortic ring and opening angle measurement.

2.4.5.1 Hyaluronic Acid

Hyaluronic acid (HA) is the simplest GAG consisting of alternating glucuronic acid and *N-acetylglucosamine*, joined by β1-3 linkage (Ayad et al., 1998). Since HA is not sulfated, non-covalent bonds via link-proteins help HA bind to the core protein of PGs, to form aggregates. HA is a structural macromolecule that functions *in-vivo* as a free carbohydrate. The kinked and resulting coil structure of this molecule provides the ECM with increased viscosity (Ayad et al., 1998). Hyaluronic acid supports and promotes both cell proliferation and migration and can be degraded in the presence of hyaluronidases. HA is synthesized within the cell plasma membrane

and is secreted by the cell into the ECM space, unaltered, and is best known for attracting water molecules (Casale & Crane, 2020).

2.4.5.2 Heparan Sulfate

Heparan sulfate (HS) consists of repeating disaccharide units of glucuronic acid joined to *N-acetylglucosamine* (Ayad et al., 1998). Interaction with key constituents of the ECM, including collagen, laminin and fibronectin promotes cell-cell and cell-ECM adhesion (Casale & Crane, 2020). HS aids in the organization of the ECM and growth factor signaling.

2.4.5.3 Chondroitin Sulfate

Chondroitin sulfate (CS) is similar to HS and is composed of repeating disaccharide units formed from glucuronic acid joined to *N-acetylgalactosamine* and hexuronic acids, joined by β1-3 linkage (Ayad et al., 1998; Casale & Crane, 2020).

2.4.5.4 Keratan Sulfate

Keratan sulfate (KS) is the only GAG not covalently bound to a protein core by a tetrasaccharide link (Casale & Crane, 2020). KS is formed by repeating units of galactose joined to *N-acetylglucosamine* by a β1-4 linkage (Ayad et al., 1998). The degree of sulfation determines the function and specific use of keratan sulfate. KS is used to regulate collagen fibril spacing and ECM organization (Casale & Crane, 2020).

2.5 Soft Tissue Behaviour

Biological soft tissues are described as fiber-reinforced composites, which display nonlinear, anisotropic response, high flexibility, and time-dependent properties (Humphrey & McCulloch, 2003; Labrosse et al., 2016). Soft tissues can be differentiated from hard tissues, such as bone, due to their lack of mineralization and gelatinous ECM. Tendons, ligaments, blood vessels, skin and

articular cartilage are some common examples of soft tissues (Holzapfel, 2008); however, the focus herein is on aortic tissue.

Mechanical response is influenced by the concentration and structural organization of constituents within the arterial wall, topographical site and function (Holzapfel, 2000). Since the treatment of aortic pathologies, including aneurysm, is fundamentally mechanobiological (Avril, 2018), understanding the contribution of each component of the wall is essential. Quantity of elastin and collagen varies within the ECM depending on function; aortic tissue is composed of approximately 25-30% collagen and 35-50% elastin, by dry weight (Humphrey, 2002; Martyn & Greenwald, 1997; Tsamis et al., 2013). The high elastin content contributes to the overall behaviour of the aorta, permitting large elastic (recoverable) deformations in response to pulsatile flow, resisting distention and preventing overstretching and rupture. In contrast, tendons and connective tissue contain approximately 65-80% collagen and <3% elastin by dry weight (Kannus, 2000), because their main function is support, facilitating the transfer of load from muscle to bone.

Unlike engineered materials which begin to exhibit plastic deformation at approximately 0.2% strain (Krauss, 2001), biological soft tissues can experience large deformations during normal physiological conditions, while maintaining shape and structure. Ultimate tensile strain of the aorta has been reported between 50-100% (Holzapfel, 2000). Materials which can withstand large deformations without internal energy dissipation are classified as hyperelastic (Chaves, 2013).

2.5.1 Nonlinear Elasticity

Soft tissues exhibit large deformations at relatively small forces, and small deformations at relatively large forces as a result of material stiffening and a nonlinear response to loading. Figure 4 exhibits the *J-shaped* tensile stress-strain behaviour of biological soft tissues—due to elastic

nonlinearity—and collagen fiber arrangement under load, which is divided into three phases (I, II, III) (Holzapfel, 2008; Wells, 2013). Stiffness refers to the local slope of the stress-strain curve; because of the nonlinear response, stiffness information needs to indicate under which stress or strain it was obtained.

Collagen, the stiffest protein within the ECM, displays an undulated and crimped rhombic-shaped pattern in the unloaded state. At low stress, elastin fibers are responsible for tissue stretching and load-bearing, while collagen fibers remain crimped, unstretched and do not contribute to the mechanical response of the tissue (Region 1). In this phase, the mechanical response is approximately linear. As load increases in Region 2, the collagen fibers begin to gradually elongate and align themselves in the direction of load, interacting with the hydrated ECM (Holzapfel et al., 2000). At high tensile stresses (Region 3), the wavy nature of the collagen fiber is non-existent; fibers are completely aligned in the direction of load (Holzapfel et al., 2000). The tissue becomes stiffer due to the resistance of collagen fibers and the stress-strain relationship is once again linear. Once the fibers can no longer bear the applied load, following fiber alignment and elongation, the ultimate tissue tensile strength is reached, non-elastic deformation will occur and the fibers will break. In summary, arterial distention depends on elastic fibers at low pressure, and collagen fibers at high pressure; the stress-strain curve for soft tissues indicates the state of the elastic fibers in the toe region, and reflects collagen in the final slope (Avril, 2018).

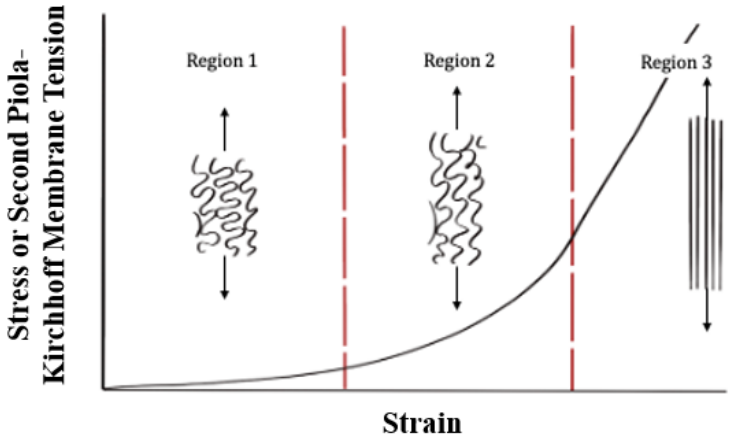

Figure 4 – Schematic diagram of typical tensile stress-strain response, with associated fiber arrangement. Image adapted from (Holzapfel, 2000).

2.5.2 Tissue Anisotropy

The term anisotropy is used to describe directional dominance of a material. The mechanical response to loading of soft tissues is dependent on the load direction, due to the orientation of fibers within the ECM (Figure 5). Fibers, including collagen and elastin, tend to orient themselves along the main load path, in the local circumferential plane; this direction will be dubbed the fiber direction (FD) in this thesis. Fibers within the ECM are also oriented in other directions which help reduce tissue shearing and promote mechanical stability. The direction normal to the fiber direction is known as the cross-fiber direction (XD), and refers to the longitudinal direction of the aorta, in this thesis. Biological soft tissues exhibit different mechanical responses in every orientation, which makes soft tissue description and modelling difficult. Due to the preferential orientation of collagen and elastin fibers within the porcine aorta, the circumferential direction accounts for greater stiffness than the longitudinal direction (Deplano et al., 2016; Gundiah et al., 2008; Martin et al., 2011), helping maintain aortic structure and function.

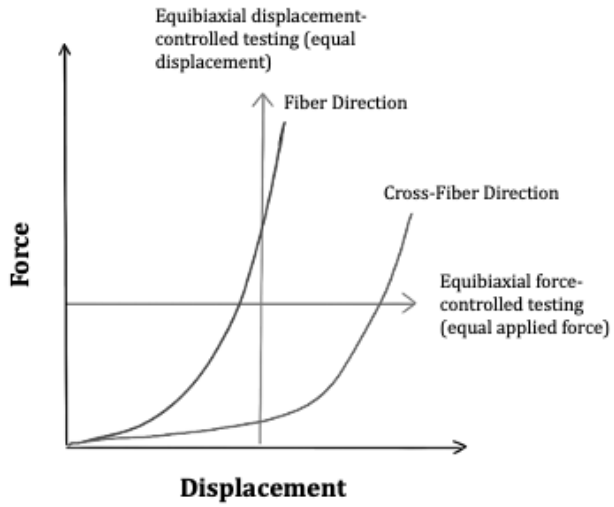

Figure 5 – Soft tissue response to loading. Biaxial tensile tests employ displacement (DC) or force-controlled (FC) testing. The upward turn of the XD force-displacement curve may be missed employing DC testing. Image adapted from (Labrosse et al., 2016)

2.6 Structural and Mechanical Heterogeneity

Morphological (specifically thickness), structural, and compositional variations are present within the aortic wall, both locally and regionally.

2.6.1 Circumferential Variations

While it has been established in the literature that the mechanical properties of blood vessels vary along the length of the vascular tree (Guo & Kassab, 2003; Sokolis, 2007), studies on the circumferential variations have been limited. Biomedical imaging has revealed non-uniform deformation within the aortic wall in healthy individuals (van Prehn et al., 2009), which begs the question: are circumferential variations present within the arterial wall to accommodate for asymmetric strain from pulsatile distention?

Aortic wall thickness changed gradually along the circumference in the porcine thoracic descending aorta, where the anterior region was thickest, while the posterior region was the thinnest, as reported by (Kim & Baek, 2011). An inversely proportional relationship was found between thickness and stiffness between the anterior, posterior and left and right lateral locations.

It was established that material stiffness was greater in the posterior portion, compared to the anterior location, in both proximal and distal regions of the descending aorta (Kim et al., 2013). However, no significant changes were detected between proximal and distal regions with respect to the anterior sample (Kim et al., 2013). A decreased stiffness in the anterior region, compared to all other regions, was also established in diseased human tissue (Iliopoulos et al., 2009), consistent with the findings of (Kim et al., 2013; Kim & Baek, 2011).

2.6.2 Regional Variations

Segmental changes exist in the structure, function and mechanical behaviour of the aorta moving distally away from the heart (Sokolis, 2007), consistent with classic textbooks on vascular physiology (Fung, 1993; Humphrey, 2002) and published literature on other animal models (Guo & Kassab, 2003; Tanaka & Fung, 1974). The stiffness of the porcine aorta increases along the length of the vascular tree, in the range of physiological conditions, and under low and high pressures. Furthermore, aortic distension decreases from the proximal to the distal aorta, due to structural heterogeneity of the arterial wall (van Prehn et al., 2009).

Regional heterogeneity along the vessel includes structural variations and arterial wall compositional changes. While the tunica intima is nearly negligible in the thoracic aorta, it increases thickness along the abdominal aorta, whereas the adventitia is inversely correlated. The media exhibits the greatest regional variations in both thickness and internal composition; thickness decreases from the proximal to distal aorta, in order to maintain a constant wall thickness-to-lumen ratio (Jana et al., 2019). Within the ECM, the quantity of elastin fibers decreases distally from the heart, as the expansion and recoil response to pulsatile flow of the cardiac cycle is dampened further from the heart (Jana et al., 2019).

2.7 Biomechanical Role of GAGs

Historically, the biomechanical role of GAGs in the aorta has been overlooked, while other ECM constituents including elastin and collagen have been extensively investigated. Although GAGs/PGs have often been neglected, their functional and regulatory significance has emerged as key influencers in the fields of cell biology and human disease and pathology (Mattson et al., 2019), due to their effect on soft tissue mechanics. GAGs have been enzymatically degraded from a variety of soft tissues, including aortic valve (AV) leaflets, lungs, tendons and arteries; the results of these studies have often been tissue-specific and contradictory. For example, the removal of GAGs from AV leaflets yielded a decrease in hysteresis (Eckert et al., 2013), while cartilage, tendons and ligaments exhibited more pronounced viscoelastic behaviour, with increased hysteresis. Similarly, in a study exposing parenchymal lung strips to similar degrative enzymes, hysteresivity was increased (Al Jamal et al., 2001; Eckert et al., 2013). While some studies have proposed that GAGs may influence dynamic viscoelastic tendon properties (Robinson et al., 2004), it has been contradicted and determined by others that GAGs have no effect on tendon viscoelasticity and/or tensile tendon mechanics (Fessel & Snedeker, 2009). Areas of contention have been identified upon comparing the mechanical response of GAGs/PGs in varying soft tissues, ultimately yielding tissue-specific responses.

The pertinent literature on the influence of GAGs/PGs on the arterial wall was reviewed, and it appears that both deficiencies and degradation, as well as accumulation and pooling of GAGs and PGs within the arterial wall may lead to an increased risk of dissection and rupture (Heegaard et al., 2007; Humphrey, 2002; Humphrey & Tellides, 2019); the result of variations in tissue stiffness in diseased states (Wells, 2013). The sequential engagement of ECM fibers in the arterial wall revealed a link between GAGs/PGs and elastin and collagen in response to mechanical

loading; indirectly influencing the biomechanical function of the porcine thoracic aorta (Mattson et al., 2017). The complete enzymatic digestion of GAGs from within the artery resulted in earlier stiffening behaviour (i.e. occurring at lower strain), suggesting the removal of GAGs is associated with earlier fiber recruitment of ECM fibers and earlier straightening of the undulated collagen fibers (Mattson et al., 2017). The earlier sequential engagement of collagen and elastin contributed to a shift in the transition point of nonlinear stress strain curves. This shows the structural and functional relationship among ECM constituents, GAGs, and the passive mechanical properties of arterial tissue; developing the framework behind the indirect role which GAGs play in arterial wall mechanics, through the engagement of collagen fibers (Mattson et al., 2017). The work by Mattson et al. (2017) strengthens the theory proposed by Linka et al. (2016). Linka et al. (2016) argue that PGs protect surrounding collagen fibers from overstretching, rather than transmitting load between them. In addition to earlier collagen fiber recruitment at lower levels of stretch, the preferential circumferential orientation of fibers was diminished with the degradation of GAGs; suggesting the role of GAG contribution to collagen fiber organization. This resulted in greater variation in fiber orientation, likely a contributor to earlier tissue stiffening (Mattson et al., 2019). Similarly, Heegaard et al. (2007) reported structural abnormalities in collagen fibrils, and reduced tensile strength of the mouse arterial wall, initiated by an artificial biglycan deficiency; spontaneous aortic dissection and rupture ensued due to this deficiency in male specimens. The PG deficiency revealed distinct abnormalities in collagen fibers, including variations in shape and size, while the wall thickness and diameter of the aorta remained unchanged (Heegaard et al., 2007). Changes in the size and shape of collagen within the ECM yielded a lower maximum stiffness, influencing the passive mechanical behaviour of the arterial wall. Although both Mattson et al. (2017) and Heegaard et al. (2007) report changes to the passive mechanical behaviour of the arterial wall, due

to the degradation of GAGs/PGs, their findings are somewhat contradictory; the maximum load withstood by biglycan depleted tissue was significantly lower compared to the control (Heegaard et al., 2007), whereas the treated tissue in Mattson et al. (2017) yielded an earlier transition to the nonlinear mechanical response, however, not absolute stiffening and/or earlier failure of the tissue. Consistent with the reported mechanical changes associated with GAG/PG degradation and deficiency, the pooling and accumulation of GAGs/PGs in the aorta have also been associated with mechanical failure. It is suggested that the pooling of these macromolecules decreases the tensile strength of the affected arterial wall (Cattell et al., 1994; Humphrey, 2002; Nataatmadja, 2006). The accumulation of GAGs within the arterial wall results in increased Gibbs-Donnan swelling, with pressures equal to or greater than normal arterial wall compressive strengths. This swelling has been reported to separate lamellae within the media, resulting in a decreased tensile carrying capacity of the affected wall due to increased disorder, promoting local delamination (Humphrey, 2002). The increased swelling pressure causes internal inhomogeneities within the ECM, and may lead to increased stress concentrations and wall weakening (Humphrey, 2002). Consistent with these findings, Cattell et al. (1994) and Nataatmadja (2006) reported increased accumulations of GAGs/PGs, contributing to aneurysm and dissection in human aorta. Furthermore, GAGs have been associated with matrix metalloproteinases (MMPs) (specifically 3 and 7)—the accumulation of GAGs has led to an increased presence of MMP-3 and -7, endopeptidases known to degrade elastin and collagen III; indicating the potential of further medial degradation and decreased wall strength (Humphrey, 2002).

Both the deficiency and accumulation of GAGs/PGs have been reported to indirectly influence the mechanical strength of the wall, either through: the earlier sequential engagement of elastin and collagen fibers in GAG depleted tissues, variations in shape and size of arterial

collagen, GAG accumulation causing increased Donnan swelling pressure, disturbing connections within the ECM, decreasing the tensile strength of the wall and development of stress concentrations. Further studies are required to determine the influence of GAGs/PGs on the arterial wall; however, it is clear that both accumulation and degradation results in dysregulated wall homeostasis. Despite these earlier findings, the tensile tissue mechanics attributable to GAGs are not fully understood.

2.8 Theoretical Framework

Continuum mechanics is founded on the theory that a material's macrostructure can be defined by locally averaged material properties, provided the length scale of the microstructure is less than that of the material. Continuum-based relationships describe a material's overall behaviour, a characteristic dependent on both internal composition and applied load. Material characterization for biological soft tissues which are heterogeneous, nonlinear, anisotropic *solid-like* materials, need a specific approach, as described in the next sections.

2.8.1 Constitutive Equations

A constitutive equation is a relationship that describes material response and distinguishes a material's behaviour. Arterial mechanics is concerned with the formation of stresses and strains when a soft tissue is exposed to external factors including forces and displacements. This section focuses on constitutive equations for nonlinear, hyperelastic material models. The goal is to relate the second Piola Kirchhoff (PK) stress tensor and the Green strain tensor, which form the basis of analytical models for hyperelastic materials. The governing field equations, including conservation of mass, linear momentum, angular momentum, and the first and second laws of thermodynamics are important; however, it is the constitutive equations which are essential in calculating unknown field variables. The constitutive equations discussed in this section will describe material

behaviour through equations that are dependent on the transformation (or deformation) gradient tensor $\boldsymbol{F}$.

2.8.2 Mechanical Deformation

Deformations are mathematically described as functions that transform a particle with a position in the reference configuration to one in the current configuration, at a given time, *t*. The transformation gradient $\boldsymbol{F}$, a second order tensor, is introduced as:

$$\boldsymbol{F} = \frac{\partial \boldsymbol{x}}{\partial \boldsymbol{X}} \qquad \text{Equation 1}$$

the derivative of the position vector $\boldsymbol{x}$ in the current configuration, with respect to the position vector $\boldsymbol{X}$, in the reference configuration. If the material is undeformed, the reference and current configurations are the same and the deformation gradient is equal to the identity tensor $\boldsymbol{I}$. The determinant of the deformation gradient is defined as the Jacobian determinant *J*. Biological soft tissues are considered incompressible and isochoric, therefore it is assumed that *J*=1.

The first law of thermodynamics introduces the concept of energy conservation. This law states that the rate of increase in energy of a system is the sum of the rate of heat supply to the system and the rate of work done by external forces on the system, such as applied forces.

$$\rho_0 \left(\frac{d\varepsilon}{dt}\right) = \boldsymbol{P}^T : \left(\frac{d\boldsymbol{F}}{dt}\right) - \nabla_0 \cdot \boldsymbol{q_0} + \rho_0 g, \qquad \text{Equation 2}$$

where ρ_0 is the mass density of the material in the current configuration (β_t), ε is the internal energy per unit mass, $\boldsymbol{P}$ is the first PK stress tensor, $\boldsymbol{F}$ is the deformation gradient relating the current configuration to the undeformed state (β_0), $\nabla_0 = \frac{\partial}{\partial \boldsymbol{X}}$ is the referential del operator, $\boldsymbol{q_0}$ is the referential heat flux vector, and g is the heat addition defined per unit mass. This theoretical framework focuses on isothermal processes and therefore with no heat transfer, $\boldsymbol{q_0} = 0$ and $g = 0$.

$$-\rho_0\left(\frac{d\varepsilon}{dt}\right)+\boldsymbol{P}^T:\frac{d\boldsymbol{F}}{dt}=0. \qquad \text{Equation 3}$$

Internal energy of a material can be represented by the relationship between Helmholtz potential (ψ), a thermodynamic potential that measures the amount of useful work obtained in an isothermal and isochoric system, and entropy (η), as a function of temperature (T).

$$\varepsilon=\psi+\eta T \qquad \text{Equation 4}$$

Therefore, the second law of thermodynamics, known as the entropy inequality, is:

$$-\rho_0\left(\left(\frac{d\psi}{dt}\right)+\eta\left(\frac{dT}{dt}\right)\right)+\boldsymbol{P}^T:\frac{d\boldsymbol{F}}{dt}-\frac{1}{T}\boldsymbol{q_0}\cdot\nabla_o T\geq 0 \qquad \text{Equation 5}$$

This referential form of the second law is referred to as the Clausius-Duhem equation and ensures that entropy has a positive value. However, because constant temperature and no heat-flux is assumed, Equation 5 reduces to:

$$-\rho_0\left(\frac{d\psi}{dt}\right)+\boldsymbol{P}^T:\frac{d\boldsymbol{F}}{dt}\geq 0 \qquad \text{Equation 6}$$

Equation 6 is critical for the development of constitutive relations for hyperelastic materials because both ψ and $\boldsymbol{P}$ depend on $\boldsymbol{F}$. Elastic and recoverable deformation force the inequality in Equation 6 to be replaced with an equality,

$$-\rho_0\left(\frac{d\psi}{dt}\right)+\boldsymbol{P}^T:\frac{d\boldsymbol{F}}{dt}=0 \qquad \text{Equation 7}$$

with reversible responses, $\psi=\psi(\boldsymbol{F})$, and the presence of $\boldsymbol{F}$ can be forced:

$$\frac{d\psi}{dt}=\frac{\partial\psi}{\partial\boldsymbol{F}}:\frac{d\boldsymbol{F}}{dt} \qquad \text{Equation 8}$$

Substituting Equation 8 into Equation 7 yields:

$$-\rho_0\left(\frac{\partial\psi}{\partial\boldsymbol{F}}:\frac{d\boldsymbol{F}}{dt}\right)+P^T:\frac{d\boldsymbol{F}}{dt}=0 \qquad \text{Equation 9}$$

The second law of thermodynamics is satisfied if the first PK stress is equal to the partial derivative of the Helmholtz potential for any transformation gradient $\boldsymbol{F}$. This yields:

$$\boldsymbol{P}^T = \rho_0 \left(\frac{d\psi}{d\boldsymbol{F}}\right) \qquad \text{Equation 10}$$

or

$$\boldsymbol{P} = \rho_0 \left(\frac{d\psi}{d\boldsymbol{F}^T}\right)$$

Equation 10 reveals a relationship between the first PK stress tensor and the Helmholtz potential, such that these are not independent constitutive equations. Therefore, based on the relationship expressed in Equation 10, only one constitutive function is required to completely describe the hyperelastic behaviour of homogeneous solids under isothermal conditions. To specify a material's response under mechanical loads, it is necessary to specify how the stress and Helmholtz potential depend on the applied fields (Bergström, 2015). Describing material behaviour can be accomplished through one constitutive function: either $\psi=\psi(\boldsymbol{F})$ or strain energy $W=W(\boldsymbol{F})$. According to the first law of thermodynamics, strain energy is related to the Helmholtz potential, such that

$$\rho_0 \psi(\boldsymbol{F}) = W(\boldsymbol{F}) \qquad \text{Equation 11}$$

where, ψ is measured per unit mass and W is measured per unit initial volume. In an isothermal system, the first PK stress can be directly related to the strain energy function. Equation 11 reveals that stress is related to either the Helmholtz potential or the strain energy function, with respect to the deformation gradient. This is why we will only focus on the strain energy function W in the remainder of the text.

It is important to note that the deformation gradient contains information on rigid body contributions; however, strain at a material point should not be influenced by rigid body motion.

Therefore, it is critical to define deformation independent of rigid body motion. From the polar decomposition theorem, $\boldsymbol{F} = \boldsymbol{R} \cdot \boldsymbol{U}$ and $\boldsymbol{F} = \boldsymbol{V} \cdot \boldsymbol{U}$ where $\boldsymbol{R}$ is a two-point tensor that represents rigid body motion, while the right stretch tensor ($\boldsymbol{U}$) defines stretch in the reference configuration and the left stretch tensor ($\boldsymbol{V}$) defines stretch in the current configuration, the latter both one-point tensors. Soft tissue deformation is also described in terms of the right ($\boldsymbol{C}$) Cauchy-Green stress tensor defined in the current configuration.

$$\boldsymbol{C} = \boldsymbol{F}^T \cdot \boldsymbol{F} \qquad \text{Equation 12}$$

Consequently,

$$\boldsymbol{C} = \boldsymbol{U}^T \cdot \boldsymbol{R}^T \cdot \boldsymbol{R} \cdot \boldsymbol{U} = \boldsymbol{U}^2 \qquad \text{Equation 13}$$

The right Cauchy-Green tensor successfully removes rigid body contributions from the transformation gradient $\boldsymbol{F}$. The strain energy function can then be related to deformation in the reference configuration using the right Cauchy-Green deformation tensor (symmetric) $\boldsymbol{C}$. As shown in Equation 11, W depends on the deformation gradient; the goal is to relate W and $\boldsymbol{F}$, sans rigid body motion, such that the appearance for $\boldsymbol{C}$ is forced: $W=W(\boldsymbol{C})$. Substituting Equation 13 into Equation 10, the first PK stress becomes:

$$\boldsymbol{P} = 2\left(\frac{\partial W}{\partial \boldsymbol{C}}\right) \cdot \boldsymbol{F}^T \qquad \text{Equation 14}$$

with $\boldsymbol{C} = \boldsymbol{C}^T$. The first PK stress tensor, referred to as the nominal stress, is a **non-symmetric** second-order tensor. Motivation to find a symmetric tensor defined in terms of the reference configuration stems from the computational difficulty associated with non-symmetric tensors. The second PK stress tensor is related to the first PK stress tensor through the inverse transpose of the deformation gradient (Humphrey, 2002):

$$\boldsymbol{S} = \boldsymbol{P} \cdot \boldsymbol{F}^{-T} \qquad \text{Equation 15}$$

Substituting Equation 14 into Equation 15 reduces to:

$$\boldsymbol{S} = 2\left(\frac{\partial W}{\partial \boldsymbol{C}}\right) \qquad \text{Equation 16}$$

The second PK stress is a convenient metric for hyperelastic constitutive formulas (Humphrey, 2002). Material stiffness is defined as a change in stress associated with a change in strain; in biomechanics, it is important to relate both stress and strain. The right Cauchy-Green stress tensor can be related to the Green strain tensor such that

$$\boldsymbol{E} = \frac{1}{2}(\boldsymbol{C} - \boldsymbol{I}) \qquad \text{Equation 17}$$

The strain energy function can be made dependent on the Green strain: $W = W(\boldsymbol{E})$, where $\boldsymbol{S} = 2\left(\frac{1}{2}\left(\frac{\partial W}{\partial \boldsymbol{E}}\right)\right)$, which reduces to:

$$\boldsymbol{S} = \frac{\partial W}{\partial \boldsymbol{E}} \qquad \text{Equation 18}$$

2.8.3 Strain Energy Functions

The main objective of material characterization and numerical simulations is to describe mathematically the behaviour of a material under specific conditions. In particular, an accurate model is essential to represent a material and predict its behaviour *in-vivo*, for patient-specific conditions, where the material's geometry, boundaries, loading conditions and behaviour must be considered. Early mechanics contributors, including Cauchy, Green, St-Venant, Almansi and Hamel recognized the nonlinear relationship between strains and the deformation gradient for finite deformations, leading to the development of nonlinear constitutive equations for hyperelastic materials.

The concept of a *strain potential*, commonly referred to as *strain energy function* is introduced to represent bodies subjected to finite deformations. Many nonlinear strain energy functions have been developed and proposed to model the mechanical behaviour of soft biological tissues. Different models have different capabilities; some assume isotropy, while others assume orthotropy. The strain energy function, W, measured per unit mass of the tissue, may be defined in terms of the Green strain components $E_{11}, E_{22}, E_{33}, E_{12}, E_{21}, E_{23}, E_{32}, E_{13}, E_{31}$. Symmetrical components include: $E_{12} = E_{21},\ E_{13} = E_{31},\ E_{23} = E_{32}$. From the strain energy function, stress can be obtained through differentiation (i.e. $\frac{\partial W}{\partial \boldsymbol{E}}$).

Preconditioning is a cyclic loading and unloading process which results in a steady state and reduces hysteresis; the internal structure of the tissue does not change unless the cyclic loading routine is altered. Hysteresis is a function of a material's viscoelasticity, and the stabilized mechanical response does not exhibit hysteresis post-preconditioning (Figure 6) (Avril, 2018). Tissues are history-dependent materials and the differentiation between these two cycles eliminates the influence of past deformations on current tissue behaviour. To establish the nonlinear stress-strain relationships, for biological soft tissues, (Fung, 1993) proposed a major simplification and introduced the concept of pseudoelasticity, whereby characterization of the material can be divided into two components—the loading and unloading phases. As such, the hyperelastic material models used in the following, namely Fung's and Guccione's, do not account for viscoelastic aspects.

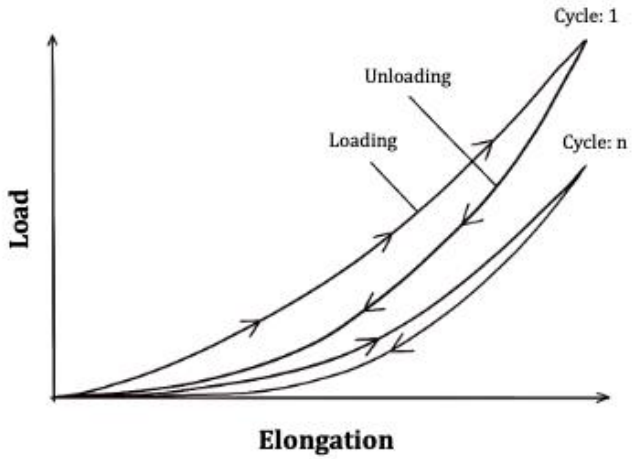

Figure 6 – The goal of preconditioning is to restore the tissue to its physiological/in-vivo state. Representative figure of a hysteresis loop, including the loading and unloading paths, image adapted from (Woo et al., 2016).

2.8.4 Specific Forms of W(C)

2.8.4.1 Fung Model

One of the most widely used hyperelastic model for soft tissue is the exponential, orthotropic constitutive model proposed by Fung (1993), and in particular, its two-dimensional (2D) equation for in-plane shear strains (Fung, 1993; Han & Fung, 1995; Sun & Sacks, 2005).

$$W_F = \frac{c_1}{2}[exp(Q_F) - 1] \qquad \text{Equation 19}$$

where Q_F is a quadratic function which accounts for in-plane shear strains and $c_i, i = 1 \dots 7$ are material constants. Full expansion of quadratic terms of Q_F yields a 7-parameter equation:

$$Q_F = c_2E_{11}^2 + c_3E_{22}^2 + 2c_4E_{11}E_{22} + c_5E_{12}^2 + 2c_6E_{11}E_{12} + 2c_7E_{22}E_{12} \qquad \text{Equation 20}$$

The strains in the fiber and cross-fiber directions, and in-plane shear are defined by E_{11}, E_{22} and E_{12}, respectively. c_1 represents a scaling factor, measured herein in terms of membrane tension, N/m, while $c_i, i = 2 \dots 7$ are dimensionless material constants. Although the experimental data can be fitted with these values, it is important to note that these constants have little physical meaning and are potentially sensitive to small changes in experimental data (Han & Fung, 1995).

Stress-strain relationships are essential in understanding material behaviour. The second PK stress ***S*** is the first partial derivative of the strain energy function, such that:

$$S_{11} = \frac{\partial W}{\partial E_{11}} = \frac{\partial W}{\partial Q_F}\frac{\partial Q_F}{\partial E_{11}} = c_1\, exp(Q_F)\,[c_2E_{11} + c_4E_{22} + c_6E_{12}] \qquad \text{Equation 21}$$

$$S_{22} = \frac{\partial W}{\partial E_{22}} = \frac{\partial W}{\partial Q_F}\frac{\partial Q_F}{\partial E_{22}} = c_1 \exp(Q_F)\,[c_3E_{22} + c_4E_{11} + c_7E_{12}]$$

$$S_{12} = \frac{\partial W}{\partial E_{12}} = \frac{\partial W}{\partial Q_F}\frac{\partial Q_F}{\partial E_{12}} = c_1 \exp(Q_F)\,[c_5E_{12} + c_6E_{11} + c_7E_{22}]$$

represent the in-plane (S_{11}, S_{22}) and shear (S_{12}) stresses of the Fung model. Refer to Appendix A.1.1 for calculations of the tangent modulus, the second partial derivative of the Fung strain energy function. The tangent modulus, also known as stiffness, can be evaluated at different levels of strain or stress.

2.8.4.2 Guccione Model

Guccione et al (1991) developed a Fung-type strain energy function with a new form for polynomial Q, which assumes three-dimensional transverse isotropy with respect to a fiber coordinate system. The Guccione model is composed of four parameters, written in terms of E_{11}, E_{22}, E_{33} and E_{12}:

$$W_G = \frac{c_1}{2}\,[exp(Q_G) - 1] \qquad \text{Equation 22}$$

where,

$$Q_G = c_2E_{11}^2 + c_3(E_{22}^2 + E_{33}^2) + 2c_4E_{12}^2 \qquad \text{Equation 23}$$

However, the Guccione model can be simplified using the material incompressibility assumption, such that E_{33} can be written in terms of E_{11} and E_{22}:

$$E_{33} = \tfrac{1}{2}\left(\tfrac{1}{\Delta} - 1\right) \text{ and } \Delta = (2E_{11} + 1)(2E_{22} + 1). \qquad \text{Equation 24}$$

Therefore, the quadratic portion of the strain energy function can be expressed as

$$Q_G = c_2 E_{11}^2 + c_3 \left(E_{22}^2 + \left(\frac{1}{2} \left(\frac{1}{(2E_{11}+1)(2E_{22}+1)} \right) \right)^2 \right) + 2c_4 E_{12}^2 \qquad \text{Equation 25}$$

The material coefficients are constant values, independent of both deformation and position within the material, which assign mechanical responses to the tissue along the fiber and cross-fiber directions (Nasopoulou et al., 2017). c_1 is the scaling factor measured in terms of membrane tension, N/m, while c_2, c_3 and c_4 are dimensionless coefficients. Increasing the values of c_2 and c_3 alters the stiffness in the fiber and cross-fiber directions, respectively, while c_4 influences fiber and cross-fiber in plane shear (Guccione et al., 1991). The second PK stress $\boldsymbol{S}$ is the first partial derivative of the strain energy function such that,

$$S_{11} = \frac{\partial W}{\partial E_{11}} = \frac{\partial W}{\partial Q_G}\frac{\partial Q_G}{\partial E_{11}} = c_1\, exp(Q_G)\left[c_2 E_{11} - \left(\frac{c_3}{2\Delta(2E_{11}+1)} \right)\left(\frac{1}{\Delta} - 1 \right) \right] \qquad \text{Equation 26}$$

$$S_{22} = \frac{\partial W}{\partial E_{22}} = \frac{\partial W}{\partial Q_G}\frac{\partial Q_G}{\partial E_{22}} = c_1 \exp(Q_G)\left[c_3 E_{22} - \left(\frac{c_3}{2\Delta(2E_{22}+1)} \right)\left(\frac{1}{\Delta} - 1 \right) \right]$$

$$S_{12} = \frac{\partial W}{\partial E_{12}} = \frac{\partial W}{\partial Q_G}\frac{\partial Q_G}{\partial E_{12}} = c_1 \exp(Q)\, c_4 E_{12}$$

Represent the in-plane and shear stresses. The stiffness is determined by the tangent modulus, refer to Appendix A.1.2 for calculations of the tangent modulus, the second partial derivative of the Guccione strain energy function.

2.9 Fundamentals of Biaxial Testing

The fundamental goal of constitutive modelling is to predict the mechanical behaviour and response of a material under loading. Experimentation is required to produce material constants and evaluate the model's predictive capabilities. Planar biaxial testing (Figure 7) provides an excellent foundation toward material characterization.

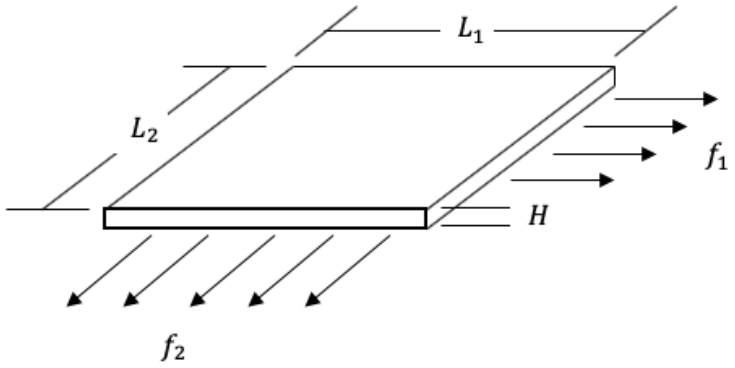

Figure 7 – Schematic of biaxial testing setup. Let f_1 and f_2 be defined as the force applied to the specimen in two orthogonal direction. L_1 and L_2 are the initial lengths and H is the undeformed thickness.

Let the undeformed (unloaded, stress-free) domain in the reference configuration (β_0) be defined as:

$$-\frac{L_1}{2} \leq X_1 \leq \frac{L_1}{2} \qquad -\frac{L_2}{2} \leq X_2 \leq \frac{L_2}{2} \qquad -\frac{H}{2} \leq X_3 \leq \frac{H}{2} \qquad \text{Equation 27}$$

where L_1 and L_2 are defined as the side lengths and H is the thickness of the specimen. Upon deformation, the undeformed domain, X_1, X_2, X_3 can be mapped to x_1, x_2 and x_3. λ_i, the stretch ratio, is assumed to be constant for each deformed configuration (homogeneous deformations, away from biaxial attachment rig).

$$x_1 = \lambda_1 X_1 + F_{12} X_2 \qquad x_2 = \lambda_2 X_2 + F_{21} X_1 \qquad x_3 = \lambda_3 X_3 \qquad \text{Equation 28}$$

The deformation gradient aids in mapping the reference configuration to the current configuration. The physical components of $\boldsymbol{F}$ written in matrix form are described by the following matrix.

$$\begin{bmatrix} \frac{\partial x_1}{\partial X_1} & \frac{\partial x_1}{\partial X_2} & \frac{\partial x_1}{\partial X_3} \\ \frac{\partial x_2}{\partial X_1} & \frac{\partial x_2}{\partial X_2} & \frac{\partial x_2}{\partial X_3} \\ \frac{\partial x_3}{\partial X_1} & \frac{\partial x_3}{\partial X_2} & \frac{\partial x_3}{\partial X_3} \end{bmatrix} = \begin{bmatrix} \lambda_1 & F_{12} & 0 \\ F_{21} & \lambda_2 & 0 \\ 0 & 0 & \lambda_3 \end{bmatrix} \qquad \text{Equation 29}$$

Biaxial testing results in planar deformation in the 1, 2 planes. The F_{i3} and F_{3j} components are reduced to zero and λ_3 is the stretch in the thickness, normal to the 1, 2 planes. Since $\det[\boldsymbol{F}] = 1 = J$:

$$1 = \lambda_1\lambda_2\lambda_3 - F_{12}F_{21}\lambda_3 \qquad \text{Equation 30}$$

from which

$$\lambda_3 = \frac{1}{\lambda_1\lambda_2 - F_{12}F_{21}}$$

Considering only in-plane deformations, the determinant of $\boldsymbol{F}$ becomes

$$det[F_{2D}] = \lambda_1\lambda_2 - F_{12}F_{21} \text{ and } J_{2D} = \lambda_1\lambda_2 - F_{12}F_{21}. \qquad \text{Equation 31}$$

The current thickness can be measured in terms of measurable quantities:

$$\lambda_3 = \frac{h}{H} = \frac{1}{J_{2D}}; h = \frac{H}{J_{2D}}. \qquad \text{Equation 32}$$

2.9.1 Stress Equilibrium

As discussed above, a sample under planar biaxial testing is acted on only by in-plane external forces, f_1 and f_2 in orthogonal directions 1 and 2, respectively. The in-plane first PK stresses are assumed to be zero for $P_{i3}, i = 1,2,3$.

$$[\boldsymbol{P}] = \begin{bmatrix} P_{11} & P_{12} & 0 \\ P_{21} & P_{22} & 0 \\ 0 & 0 & 0 \end{bmatrix} = \begin{bmatrix} \frac{f_1}{HL_2} & 0 & 0 \\ 0 & \frac{f_2}{HL_1} & 0 \\ 0 & 0 & 0 \end{bmatrix} \qquad \text{Equation 33}$$

Since the applied loads are aligned with the coordinate axes, $P_{12} = P_{21} = 0$. It is then assumed that the first PK stresses do not vary significantly through the undeformed thickness, *H*. Therefore, the components of the first PK membrane tension tensor, $\boldsymbol{T}^P$, can be written as:

$$T_{\alpha\beta}^{P} = \int_{-\frac{H}{2}}^{\frac{H}{2}} P_{\alpha\beta} dX_3 \qquad \text{Equation 34}$$

$$T_{\alpha\beta}^{P} = P_{\alpha\beta} H$$

Using this equation, the membrane tension at P_{11} and P_{22} in plane 1 and 2, respectively, becomes:

$$T_{11}^{P} = H\left(\frac{f_1}{HL_2}\right) = \frac{f_1}{L_2} \qquad T_{22}^{P} = H\left(\frac{f_2}{HL_1}\right) = \frac{f_2}{L_1} \qquad \text{Equation 35}$$

Planar biaxial testing allows applied forces f_1 and f_2 to be controlled, especially during proportional loading. The second PK stress tensor, in matrix notation is written as:

$$[\boldsymbol{S}] = \frac{1}{J_{2D}} \begin{bmatrix} \frac{f_1}{HL_2} & 0 & 0 \\ 0 & \frac{f_2}{HL_1} & 0 \\ 0 & 0 & 0 \end{bmatrix} \begin{bmatrix} \lambda_2 & -F_{21} & 0 \\ -F_{12} & \lambda_1 & 0 \\ 0 & 0 & J_{2D}^2 \end{bmatrix} \qquad \text{Equation 36}$$

$$[\boldsymbol{S}] = \frac{1}{J_{2D}} \begin{bmatrix} \frac{\lambda_2 f_1}{HL_2} & -\frac{F_{12} f_1}{HL_2} & 0 \\ -\frac{F_{12} f_2}{HL_1} & \frac{\lambda_1 f_2}{HL_1} & 0 \\ 0 & 0 & 0 \end{bmatrix}$$

with $\frac{F_{21} f_1}{HL_2} = \frac{F_{12} f_2}{HL_1}$ because of matrix symmetry. Similar to the first PK membrane tension, it is assumed that the stress does not vary significantly through the deformed thickness and the PK2 membrane tension becomes $\boldsymbol{T}^{S}$. Note, the superscript changes depending on the stress tensor it describes.

$$T_{\alpha\beta}^{S} = \int_{-\frac{H}{2}}^{\frac{H}{2}} S_{\alpha\beta} dX_3 \qquad \text{Equation 37}$$

$$T_{\alpha\beta}^{S} = S_{\alpha\beta} H$$

Since $S_{11} = \frac{\lambda_2 f_1}{H J_{2D} L_2}$, $S_{22} = \frac{\lambda_1 f_2}{H J_{2D} L_1}$, and $S_{12} = S_{21} = \frac{F_{12} f_2}{H J_{2D} L_1}$, and $T_{21}^{S} = T_{12}^{S}$, the in plane second PK membrane tension becomes:

$$T_{11}^{S} = H\left(\frac{\lambda_2 f_1}{H J_{2D} L_2}\right) = \frac{\lambda_2 f_1}{J_{2D} L_2} \qquad \text{Equation 38}$$

$$T_{22}^{S} = H\left(\frac{\lambda_1 f_2}{H J_{2D} L_1}\right) = \frac{\lambda_1 f_2}{J_{2D} L_1}$$

$$T_{12}^{S} = -H\left(\frac{F_{21} f_1}{H J_{2D} L_2}\right) = -\frac{F_{21} f_1}{J_{2D} L_2} = \frac{F_{12} f_2}{J_{2D} L_1}$$

Similar to $\boldsymbol{T}^{P}$, the applied in-plane loads are oriented in the same direction as the coordinate axes, while the shear components become zero ($F_{12} = F_{21} = 0$). Therefore, T_{11}^{S} and T_{22}^{S} are the only non-zero components of the tensor.

2.10 Material Constant Identification

The motivation behind the identification of material constants is to accurately fit strain energy functions to the experimental data, through nonlinear, multivariate optimization, following preconditioning. The loading phase of each protocol was tracked and used for determination of material constants for Fung and Guccione strain energy functions. To increase the predictive capabilities of a model, the data from 9 proportional loading protocols were fitted simultaneously.

A nonlinear optimization technique was employed to determine the material constants, c_i, by minimizing the differences between the theoretical and experimental second PK membrane tensions, through numerical regressions: $\left\| \left| T_{11_{exp}}^{S} - T_{11_{theo}}^{S} \right| + \left| T_{22_{exp}}^{S} - T_{22_{theo}}^{S} \right| + \left| T_{12_{exp}}^{S} - T_{12_{exp}}^{S} \right| \right\|^2$, where the simulated data is matched to the experimental. Refer to (Labrosse et al., 2016) for details on material constant identification and implementation.

2.11 Summary

As can be gathered from the literature reviewed, understanding the influence of individual ECM constituents will aid in the effective calibration of numerical models and simulations to more reliably predict *in-vivo* behaviour, including mechanical stresses and geometry. In addition, current

areas of contention in the literature include (i) the circumferential variations in mechanical response at a given anatomically relevant regions; and (ii) the influence of GAGs on arterial wall mechanical behaviour. To provide insight into both issues, detailed biaxial testing of porcine aortic tissue will be carried out, and the effect of partial and complete enzymatic degradation on the mechanical properties will be investigated. In so doing, the mathematical developments presented in this chapter will be brought to bear, allowing for the identification of material constants for two hyperelastic constitutive models, which will then allow for the determination of strain and stiffness at specific levels of membrane tensions to further probe the properties of the tissues. Experimental materials and methods, results, and discussion will be presented in the following pages, and used to determine whether or not GAGs and planar biaxial mechanical behaviour of the aortic wall are related.

3 Materials and Methods

3.1 Tissue Preparation

Fresh porcine aortas were collected from a local abattoir (*Tom Henderson's Meats and Abattoir Inc., Chesterville, Canada*) within hours of slaughter. The aortas were harvested from the hearts of 5-6-month-old pigs, weighing approximately 90-105 kg. Tissue preparation varied, depending on analysis. Native porcine tissue used for material characterization ($n=9$) were cleaned of peripheral organs, while connective and fatty tissue remained intact and were removed just prior to mechanical testing. Alternatively, samples prepared for enzymatic digestion ($n=8$) were cleaned of peripheral organs and connective and fatty tissues prior to incubation with enzymes.

The aortas were divided into three regions: the (i) ascending aorta (Asc.); (ii) aortic arch (Arc.); (iii) thoracic descending (Tho.) aorta, Figure 1. A ring of tissue was dissected from each of the regions and opened along its superior edge. Furthermore, for untreated tissues, four regions were designated for mechanical testing: the anterior (A), posterior (P), and left (L) and right (R) lateral walls. This yielded four (4) samples per region, and twelve (12) samples per untreated aorta. For enzymatically digested samples, the A, P, L, and R regions were not identified, rather, three adjacent samples were removed from each ring, for zero digestion, partial digestion and full digestion, respectively. This yielded nine (9) samples per aorta. For both experiments, the samples were cut using parallel steel razor blades, into 9 x 9 mm squares, whose sides were aligned with, or orthogonal to the direction of fiber reinforcement, as determined by the circumferential and longitudinal directions of the aorta, respectively (Figure 8). Untreated samples were mechanically tested within 24 hours of explantation, to minimize tissue decay and changes in mechanical properties. GAG-digested tissues were mechanically tested within 56 hours of harvest; tissues were stored in saline solution at 4ºC between steps.

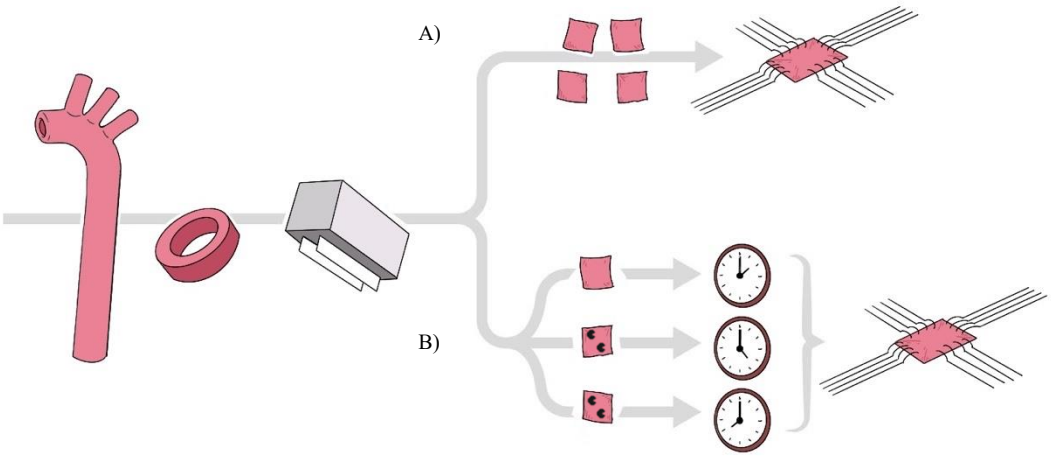

Figure 8 – Schematic of tissue processing steps. A) Parallel steel blades are used to cut 4 square samples (A, P, L, R) from each anatomically relevant region, followed by biaxial testing; B) Parallel steel blades are used to cut 3 square samples which are untreated, partially, and fully enzymatically GAG-depleted and incubated for 0-, 4-, and 48-hours, followed by mechanical testing within 56-hours.

3.2 Biaxial mechanical testing

Prior to biaxial testing, sample thickness was evaluated using an electronic thickness gauge (*Model 700-118-20, Mitutoyo, Japan*). The thickness of each sample was calculated from the average of three different measurements at three different locations. The 5N capacity biaxial testing machine (*BioTester 5000, CellScale, Waterloo, Canada*) was outfitted with four tungsten rakes containing 5 tines each, spaced 0.7 mm apart. The rakes were magnetically mounted to the four goosenecks, and each set of tines were permanently attached to a base; this enabled simultaneous puncture of all attachment points when the platform was manually lifted, and pressure was applied to the sample during the attachment process. An integrated temperature-controlled saline bath, set to 37ºC was located below the goosenecks, and raised into place using a manual lift to immerse the samples 10 minutes prior to tissue preconditioning and during the preconditioning protocol. The saline bath was removed prior to displacement control testing to reduce glare and mitigate effects from water reflections.

A custom displacement-control template was written in Matlab (*Matlab R2013a, The MathWorks, Natick, MA, USA*) by Labrosse et al. (2016) to minimize human-error involved in inputting test parameters including test phase parameters, bath temperature, and image acquisition frequency. The Matlab template integrated with LabJoy software enabled the user to perform testing based on user specifications. According to the protocol outlined by (Labrosse et al., 2016), the system worked best in displacement-control rather than force-control; however, in displacement-control testing, the upward turn of displacement curves can be missed (Figure 5). Therefore, force-control plots were created by adjusting the equibiaxial displacement-controlled protocol to approximate a force-controlled one. The maximum displacement in the x and y directions were identified to yield the same force acting in both axes. An adjusted term was introduced to ensure the maximum force in Protocols 1-4 and 6-9 were similar to the resultant force in Protocol 5, from maximum displacement, for the x and y direction, respectively (Table 2). The samples were subjected to 10 preconditioning protocols at equal force, followed by 9 proportional loading and unloading protocols (Table 2, Figure 9). A range of preconditioning cycles has been reported in the literature, however, 10 preconditioning cycles has been considered sufficient to generate repeatable data (Labrosse et al., 2016)

A)

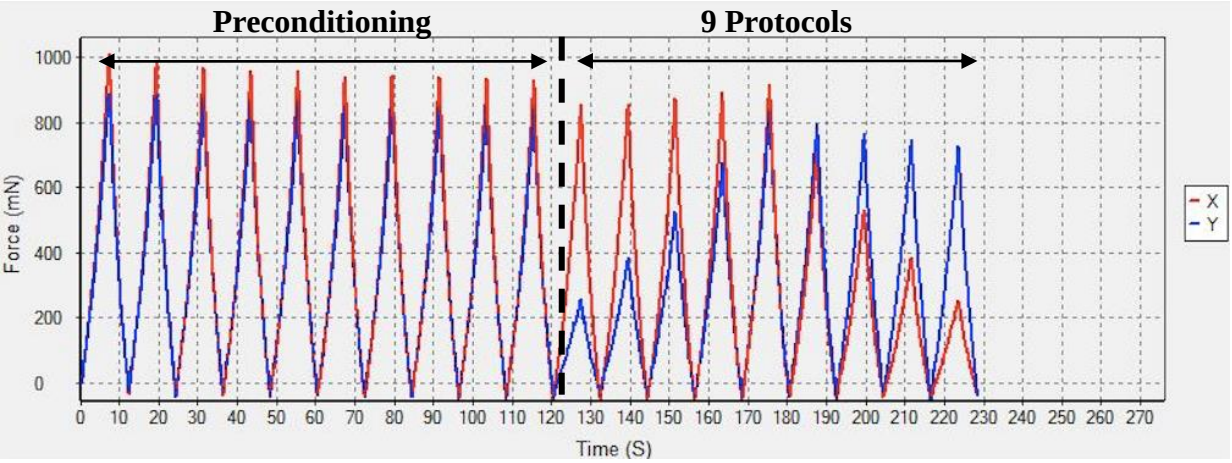

B)

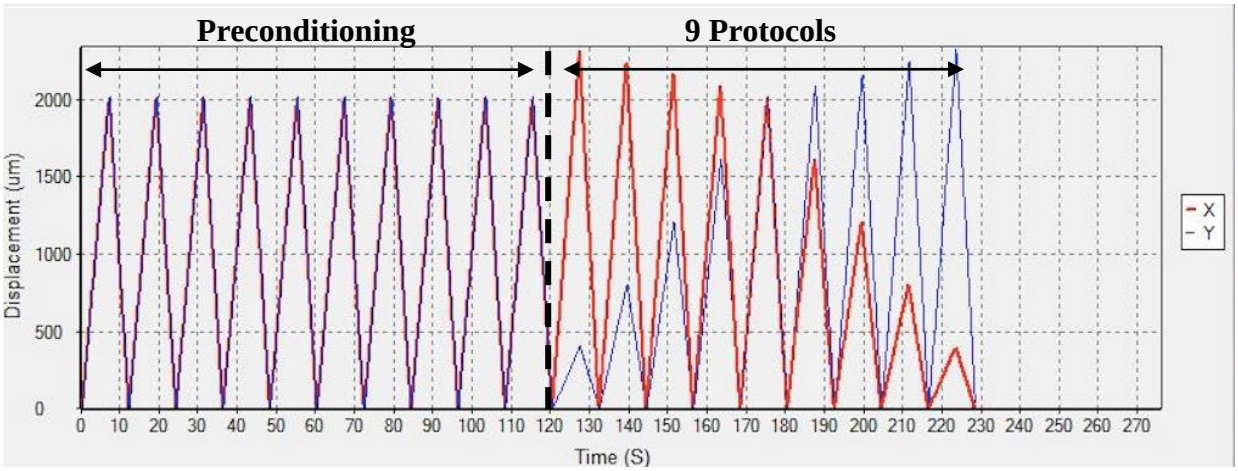

Figure 9 – Representative Labjoy outputs. Directions X (red) and Y (blue) are independent of one another. The samples are preconditioned 10 times, followed by 9 proportional loading and unloading cycles. A) Force vs. time curves; B) Displacement vs. time curves.

Table 2 – Biaxial tensile testing experimental protocol. Adjusted maximum displacement to convert displacement-control setup to mimic force-control. Table adapted from (Labrosse et al., 2016).

Protocol	Maximum displacement	
	X-direction	Y-direction
Preconditioning (10 cycles)	Umax_X (equibiaxial)	Umax_Y (equibiaxial)
1	Umax_X + Uadj_X	1/5Umax_Y
2	Umax_X + 3/4Uadj_X	2/5Umax_Y
3	Umax_X + 1/2Uadj_X	3/5Umax_Y
4	Umax_X + 1/4Uadj_X	4/5Umax_Y
5	Umax_X (equibiaxial)	Umax_Y (equibiaxial)
6	4/5Umax_X	Umax_Y + 1/4Uadj_Y
7	3/5Umax_X	Umax_Y + 1/2Uadj_Y
8	2/5Umax_X	Umax_Y + 3/4Uadj_Y
9	1/5Umax_X	Umax_Y + Uadj_Y

Umax_X, Umax_Y: The maximum displacement in the x and y directions that yield equal force in both axes.
Uadj_X: adjustment in the X-direction such that the force in the X-direction during Protocols 1-4 is similar to the force experienced in Protocol 5—Umax_X.
Uadj_Y: adjustment in the Y-direction such that the force in the Y-direction during Protocols 6-9 is similar to the force experienced in Protocol 5—Umax_Y.

3.3 Enzymatic GAG Digestion

To enzymatically remove GAGs from the porcine aorta, a protocol adapted by (Mattson et al., 2017) was used. Samples were treated with 6-15 U/ml hyaluronidase, 0.075 U/ml chondroitinase

ABC, 0.75 U/ml heparinase I and III blend (*Sigma-Aldrich #H3506, C3667, H3917, St. Louis, USA)* in a 100 mM ammonium acetate buffer, pH 7.0. Samples were submerged in 1 ml of solution and incubated at 37°C for 0-, 4- and 48- hours for zero, partial, and total digestion, respectively—corresponding to approximately 41.4 ± 20.4% and 89.6 ± 3.0% decrease in GAG content, in preliminary experiments. The solution was mixed with an 800 μl pipette 10 times every hour between 1-4, 21-24 and 44-48 hours. Following enzymatic digestion, samples were rinsed and placed in 3 1xPBS baths for 5 minutes each and stored in saline solution at 4°C prior to mechanical testing.

3.4 Determination of Sample Dimensions

Samples were placed on a 1x1 cm grid and photographed prior and following the partial and complete enzymatic degradation of GAGs. Photographs of the samples were captured at 0-, 4-, and 48-hour incubation, respectively. Image Viewer, an application part of the Matlab suite, was used to measure the length and width of the tissue sample and grid. Pixel quantity of the sample length and width, relative to pixel quantity of the 1x1 cm scale, was used to compare dimensions of untreated and treated tissue samples.

3.5 Quantification of Sulfated Glycosaminoglycans

Aortic tissue samples were sectioned using a cryostat (*CM3050-S, Leica, Wetzlar, Germany*) into approximately 300 μm thick segments, from the adventitia to the intima, to quantify the mural distribution of sulfated glycosaminoglycans (s-GAG) through the tissue. Aortic tissue weight was measured using an AB204-S/FACT Classic Plus digital scale (*Mettler Toledo, Columbus, Ohio, USA*) prior to digestion, to normalize s-GAG levels. Enzymatic tissue digestion was performed by immersing porcine tissue in a 40 μg/ml papain digest (*Sigma Aldrich, St-Louis, MO, USA*), in a buffer composed of 5 mM L-cysteine and 5 mM ethylenediaminetetraacetic acid (EDTA), for 48

hours at 65°C. Upon visual inspection, solutions identified with a yellow tint were diluted to 10%; 5 μl sample, 45 μl PBS. Papain digested tissue samples were stored at -20°C until dye-spectrometric analysis could be performed.

The s-GAG content of papain-digested samples was assessed using 1,9-dimethylmethylene blue zinc chloride double salt (DMMB) (*Sigma-Aldrich, St-Louis, MO, USA*). DMMB is a thiazine chromotope agent that yields a colour change from blue to pink when the positively charged DMMB binds to negatively charged s-GAG. The quantification was determined through colour, spectrophotometrically, at 525 and 590 nm using the Epoch microplate spectrophotometer (*BioTek Instruments Inc, Winooski, VT, USA*); the colour change was determined by the resultant s-GAG dye complexes. For calibration, a standard curve was generated using chondroitin sulfate A sodium salt (*Alfa Aesar, Haverhill, MA, USA*) and the ratio of average absorbance; net absorbance values at 525 nm were divided by values at 590 nm. Unlike absorbance readings at a single wavelength, the absorbance ratio produces a linear calibration curve, which can be used to calculate the concentration of an unknown sample (Ernst & Zor, 2010).

3.6 Image Processing of Biaxial Testing Data

Image processing and point-tracking is necessitated by the well-known phenomenon that biological soft tissues and biomaterials may be subjected to less strain than calculated from grip displacements, due to potential tissue tearing and subsequent effects. In order to mitigate these effects, data is post-processed from images obtained from biaxial testing. A central target region is identified, located away from the outer edges, to determine the actual strain distribution within the sample. Within this region, the stress and strain field are assumed to be homogenous such that the elements of the deformation gradient are independent of location (Sacks, 2000).

The images from displacement-controlled testing were analyzed and reviewed in Labjoy. Only the stretching cycle was considered due to the similarity between the loading and unloading paths in both force and displacement curves (Labrosse et al., 2016). The strains within the samples were determined using a 9x9 node grid overlaid on optical markers manually selected for their homogeneous strain and displacement in the central region of the samples, and automatically tracked through the loading phase of each protocol (Protocol 1-9—Figure 9). The resulting information was saved to one file per protocol and later used for determination of material constants. The optical markers on the tissue samples were created with carbon dust and dabbed onto the intima of each sample. These markers, in the unloaded, stress-free, undeformed configuration, were mapped to the deformed configuration, refer to Fundamentals of Biaxial Testing.

3.6.1 Experimental determination of strains

Among the 9x9 node grid mentioned above, four *well-behaved* nodes, defined as nodes with reasonable displacements within the central target region were identified. These nodes were mapped from their real-time position coordinates in the current (deformed) configuration, (x_1, x_2), to their isoparametric coordinates, (r, s), which is the corresponding square parent coordinate system, Figure 10. The displacement gradient, stress and strain were assumed homogenous within the central target region.

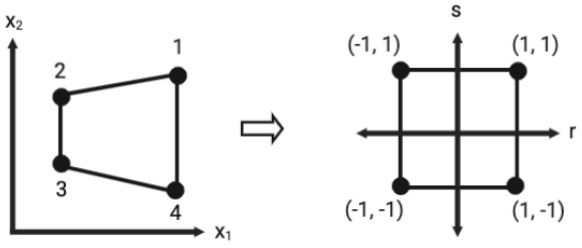

Figure 10 – Mapping carbon markers from the current configuration to the respective isoparametric coordinate system. Diagram adapted from (Sacks, 2000).

In order to compute strain optically, displacements u and v along the coordinate axes, as well as positions X_1 and X_2 of the quad finite element in the reference configuration can be calculated at any time or location within the central target region. The procedure outlined in (Labrosse et al., 2016) summarizes the theoretical principles behind optical strain analysis.

In two dimensions, the deformation gradient can be used to calculate the values of the stretch ratios, whereby $\boldsymbol{x} = \boldsymbol{u} + \boldsymbol{X}$. Determining the displacement with respect to the reference configuration yields, $\frac{\partial \boldsymbol{x}}{\partial \boldsymbol{X}} = \frac{\partial \boldsymbol{u}}{\partial \boldsymbol{X}} + \frac{\partial \boldsymbol{X}}{\partial \boldsymbol{X}}$ which becomes $\boldsymbol{F} = \frac{\partial \boldsymbol{u}}{\partial \boldsymbol{X}} + \boldsymbol{I}$. The deformation gradient $\boldsymbol{F} = \begin{bmatrix} \frac{\partial u}{\partial X_1} + 1 & \frac{\partial u}{\partial X_2} \\ \frac{\partial v}{\partial X_1} & \frac{\partial v}{\partial X_2} + 1 \end{bmatrix} = \begin{bmatrix} \lambda_1 & F_{12} \\ F_{21} & \lambda_2 \end{bmatrix}$ can be used to calculate the stretch ratios at any (r, s).

One method of deriving the Green strain tensor (also known as the St-Venant or Lagrangian strain) $\boldsymbol{E}$, is through the manipulation of the deformation gradient, such that $\boldsymbol{E} = \frac{1}{2}(\boldsymbol{F}^T \cdot \boldsymbol{F} - \boldsymbol{I})$. It is important to note that the Green strain tensor is symmetric by nature due to the absence of rigid body rotation, outlined in (Labrosse et al., 2016).

3.7 Statistical Analysis

The material parameters reported herein are produced from a Matlab code written by (Labrosse et al., 2016), which performs nonlinear optimization techniques based on the *fmincon* function. Each material parameter is produced with a 95% confidence interval, shown in parenthesis and its respective Pearson correlation coefficient for each strain energy function. The strain and stiffness values are averages at each region, Asc., Arc., Tho, with standard deviation, unless reported otherwise. An unpaired t-test, assuming unequal variance, was employed to determine statistical differences between fiber directions. A one-way ANOVA, with Tukey's post-hoc test, was used to determine statistical differences between the anterior, posterior, and left and right lateral samples in each region, changes in mechanical response distally from the heart, and the influence of s-GAG

content on mechanical properties. Statistical significance was determined by $p < 0.05$ for Experiment 1, and $p < 0.025$ for Experiment 2; a more stringent significance threshold was assigned for Experiment 2, to better interpret data and increase confidence in the determination of significance.

4 Results

4.1 Experiment 1: Control Group

Because the material constants of the constitutive models considered do not allow for easy comparisons between materials and their stress-strain curves, strain and stiffness (the local slope of the curve) of porcine aortas under arbitrary membrane tensions of 60 and 120 N/m were used to evaluate circumferential, regional and directional variations in tissue behaviour (Figure 11). The values of 60 and 120 N/m are common reference values in the literature (Martin et al., 2011). The strain and stiffness were computed from the fitted material models, namely Fung and Guccione, to ensure that the ensemble average stress-strain curves were smooth, in contrast to the somewhat jagged average of the experimental stress-strain curves. In addition, to assess the anisotropic nature of the tissues, we evaluated the ratios of strains (*E_FD/E_XD*) and stiffness (*S_FD/S_XD*), both under 60 and 120 N/m membrane tensions. Ratios different from unity would denote non-isotropic behaviour.

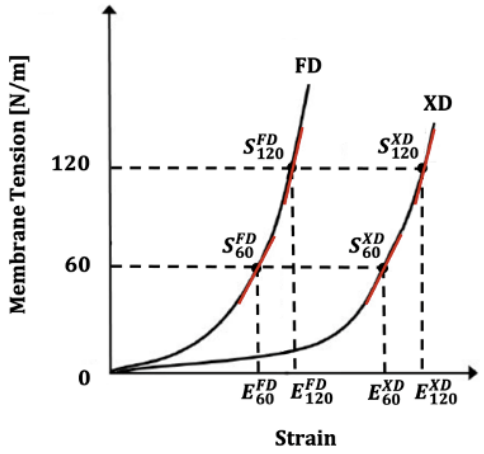

Figure 11 – Schematic stress-strain curve evaluated under membrane tensions of 60 and 120 N/m. The stiffness is the local slope of the curve at 60 and 120 N/m, respectively (denoted in red).

4.1.1 Circumferential and Regional Variations in Thickness

In the ascending, arch and thoracic descending regions of the porcine aorta, the aortic wall thickness did not vary significantly within the designated locations: anterior (A), posterior (P), and left (L) and right (R) lateral sides. The average thickness of the A, P, L and R in each anatomically relevant region is summarized in Table 3. These results suggest that aortic wall thickness is independent of the circumferential location. However, regional differences were observed in wall thickness moving distally from the heart, as expected. The average tissue thickness, defined as the mean thickness of the A, P, L, R locations in the ascending, arch and thoracic descending regions was 2.13 ± 0.21, 1.82 ± 0.23 and 1.47 ± 0.26 mm, respectively. The mean thickness measured significantly decreased moving along the length of the vascular tree, away from the heart (p=5.43E-20).

Table 3 – Average thickness of the A, P, L, R sides in the Asc., Arc. and Tho, with standard deviation.

Circumferential Location	Average Thickness [mm]		
	Asc.	Arc.	Tho.
Anterior	2.00 ± 0.15	1.98 ± 0.20	1.39 ± 0.14
Posterior	2.15 ± 0.21	1.77 ± 0.25	1.48 ± 0.25
Left Lateral	2.23 ± 0.17	1.80 ± 0.26	1.53 ± 0.29
Right Lateral	2.13 ± 0.25	1.75 ± 0.17	1.49 ± 0.35

4.1.2 Circumferential Variations in Mechanical Properties

As mentioned, mechanical properties including Green strain (E) and stiffness (S), in the circumferential or fiber-direction (FD) and longitudinal or cross-fiber direction (XD) were defined at 60 and 120 N/m membrane tensions, in the ascending, arch and thoracic descending regions of the porcine aorta. Quantile-Quantile (Q-Q) plots were produced in conjunction with correlation coefficients to conclude normality among A, P, L, R data. Average strain and stiffness along the

circumference of each region is summarized for the Fung and Guccione model in Appendix B: Supplementary Results.

One-way ANOVA with Tukey's test for post-hoc analysis revealed no statistical difference in Green strain and stiffness between the A, P, L and R regions in any segment, in both the circumferential and longitudinal directions. Consistent with the findings in *Circumferential and Regional Variations in Thickness*, these results suggest that tissue behaviour is independent of circumferential location, Figure 12 and Figure 13. Since variations in mechanical properties and thickness were not observed along the circumference, a single representative sample from each anatomically relevant region, rather than A, P, L, R was considered (Table 4).

Table 4 – Average Green strain and stiffness values at 60 and 120 N/m using one representative sample from each anatomically relevant location.

Average Material Property	Fung			Guccione		
	ASC.	ARC.	THO.	ASC.	ARC.	THO.
E_FD@60N/m [-]	0.18 ± 0.036	0.17 ± 0.031	0.18 ± 0.042	0.18 ± 0.037	0.18 ± 0.032	0.19 ± 0.061
E_XD [-]	0.16 ± 0.045	0.14 ± 0.020	0.15 ± 0.026	0.16 ± 0.049	0.14 ± 0.025	0.15 ± 0.037
E_FD/E_XD	1.1 ± 0.38	1.2 ± 0.28	1.2 ± 0.35	1.1 ± 0.41	1.3 ± 0.33	1.3 ± 0.53
S_FD [N/m]	385.56 ± 48	397.11 ± 32	410.11 ± 25	332.78 ± 37	345.22 ± 24	355.33 ± 18
S_XD [N/m]	431.22 ± 85	466.89 ± 51	467.67 ± 109	364.89 ± 58	391.56 ± 36	391.67 ± 54
S_FD/S_X	0.89 ± 0.21	0.85 ± 0.12	0.88 ± 0.21	0.91 ± 0.17	0.88 ± 0.10	0.91 ± 0.13
E_FD@120N/m [-]	0.27 ± 0.044	0.26 ± 0.035	0.26 ± 0.046	0.28 ± 0.045	0.26 ± 0.037	0.27 ± 0.070
E_XD [-]	0.24 ± 0.059	0.21 ± 0.032	0.22 ± 0.039	0.24 ± 0.063	0.21 ± 0.034	0.22 ± 0.052
E_FD/E_XD	1.1 ± 0.33	1.2 ± 0.24	1.2 ± 0.30	1.2 ± 0.37	1.2 ± 0.26	1.2 ± 0.42
S_FD [N/m]	623.67 ± 67	656.78 ± 44	708.11 ± 50	627.67 ± 56	668.67 ± 27	698.44 ± 20
S_XD [N/m]	680.56 ± 87	750.67 ± 103	792.11 ± 207	672.78 ± 75	739.00 ± 71	757.44 ± 107
S_FD/S_XD	0.92 ± 0.15	0.87 ± 0.13	0.89 ± 0.24	0.93 ± 0.13	0.90 ± 0.094	0.92 ± 0.13

E_FD/E_XD: Strain between fiber and cross-fiber direction under 60 and 120 N/m 2nd PK membrane tension, respectively.
S_FD/S_XD: Stiffness between fiber and cross-fiber direction under 60 and 120 N/m 2nd PK membrane tension, respectively.

4.1.3 Regional Variations in Mechanical Properties

Regional variations in the mechanical response in the circumferential and longitudinal directions were observed, moving distally from the heart. One-way ANOVA with Tukey's post-hoc analysis revealed significantly stiffer thoracic descending wall response, compared to the ascending aorta, in the circumferential direction at 120 N/m (p=0.011). The measured stiffness was not significantly

different along the length of the aorta in both directions at 60 N/m or 120 N/m membrane tension. However, the average stiffnesses reported in Table 4, and displayed in Figure 14 and Figure 15, suggest that stiffness may be increasing distally.

4.1.4 Directional Variations in Mechanical Properties

The circumferential and longitudinal strains and stiffnesses were assessed at 60 and 120 N/m. Comparing the circumferential and longitudinal directions, no statistically significant directional variations were detected between the circumferential and longitudinal responses in the ascending and thoracic descending aorta; preferential fiber-orientation did not influence directional variations. However, in the aortic arch, direction of applied load significantly influenced material response, such that strain was greater in the circumferential direction than in the longitudinal (Fung – p=, Guccione – p=0.020), while stiffness was greater in the longitudinal direction (Fung – p=0.0058, Guccione – p=0.0028). Figure 14 and Figure 15 display the relationship between circumferential and longitudinal directions in the Asc., Arc., and Tho., with respect to strain and stiffness, for the Fung and Guccione models, respectively. The same findings were observed using the Fung and Guccione models. The ratio between strain and stiffness in two perpendicular directions is reported in Table 4 and was used to illustrate the mostly isotropic behaviour of the porcine aorta (unit ratio for isotropy).

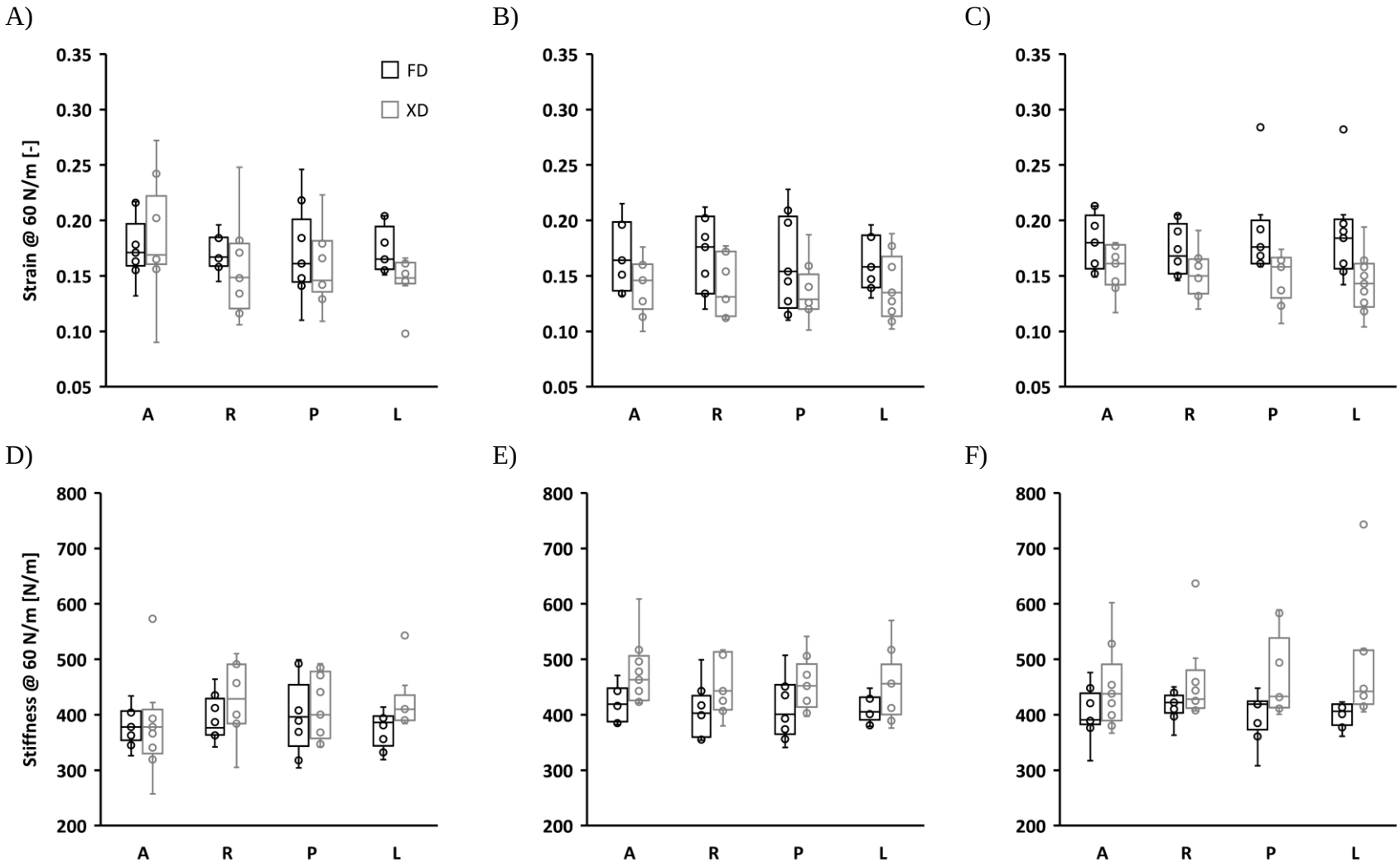

Figure 12 – Representative figures produced using the Fung model comparing the circumferential and longitudinal strain at 60 N/m membrane tension in A) the ASC; B) the ARC; C) THO; and stiffness at 60 N/m membrane tension in D) the ASC; E) the ARC; F) the THO.

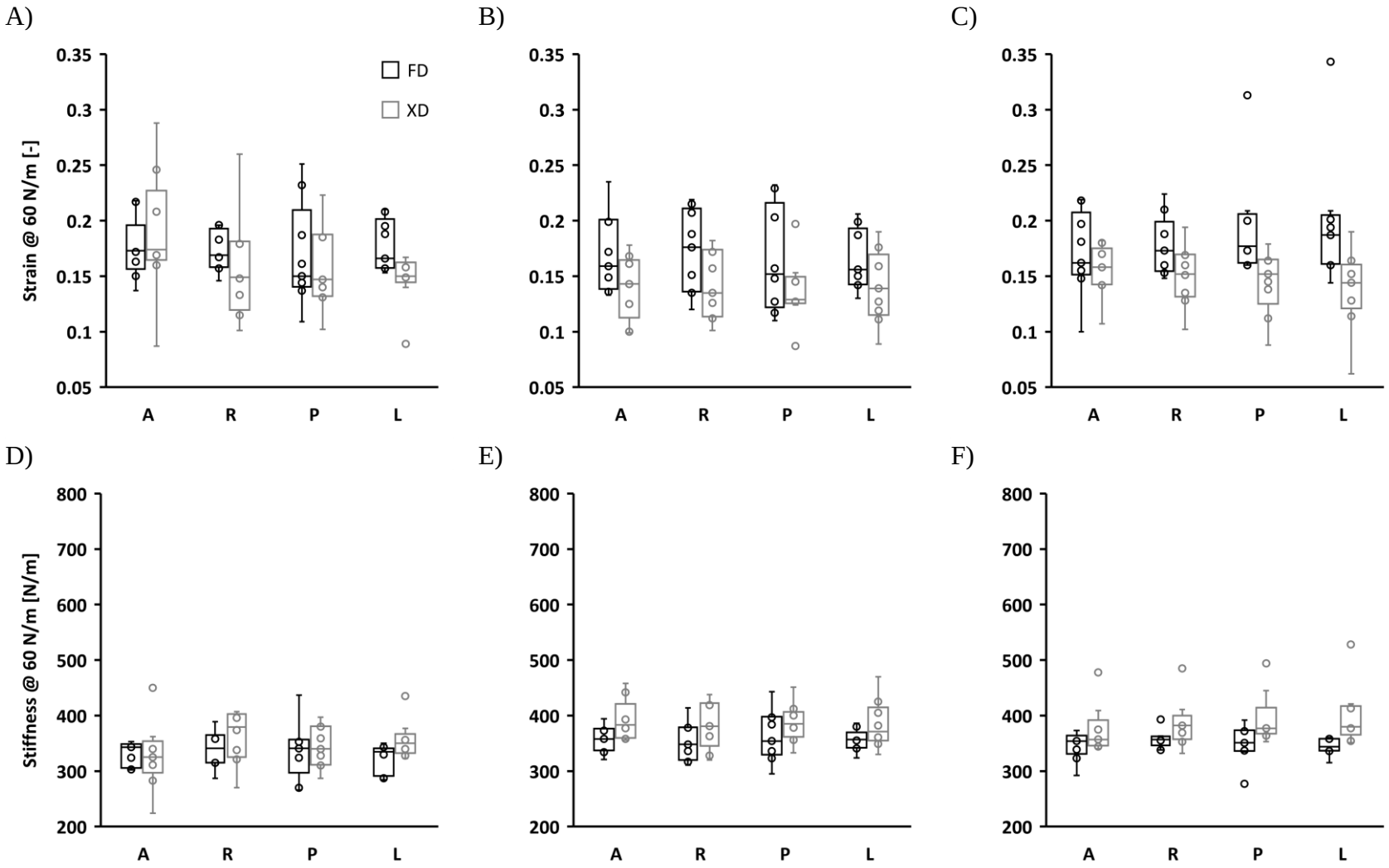

Figure 13 – Representative figures produced using the Guccione model comparing the circumferential and longitudinal strain at 60 N/m membrane tension in A) the ASC; B) the ARC; C) THO; and stiffness at 60 N/m membrane tension in D) the ASC; E) the ARC; F) the THO.

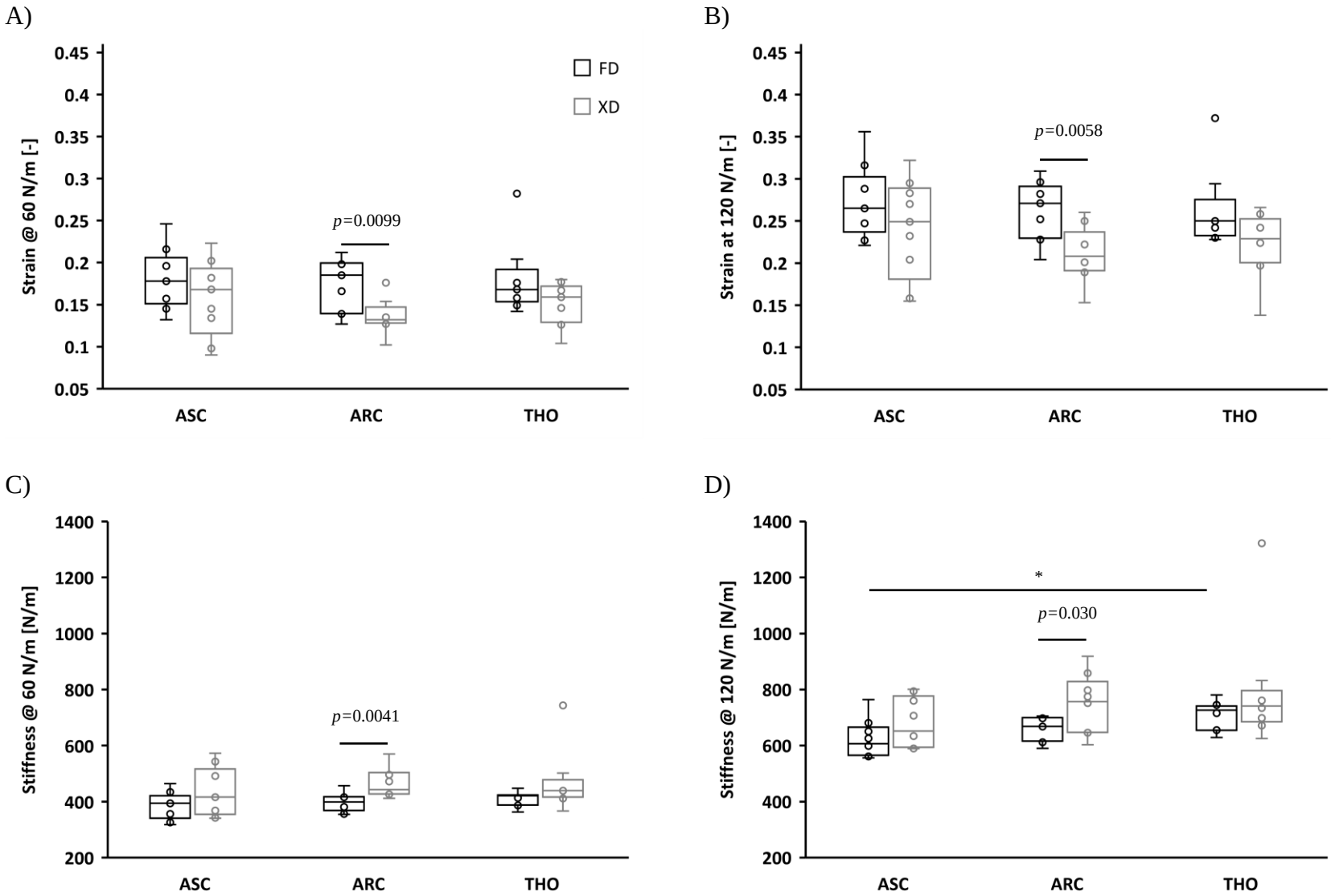

Figure 14 – Circumferential and longitudinal response in the Asc., Arc., and Tho. – Fung model A) Strain at 60 N/m; B) Strain at 120 N/m; C) Stiffness at 60 N/m D) Stiffness at 120 N/m. The p-value is specified where the FD and XD are significantly different. * Represents statistical significance between two regions.

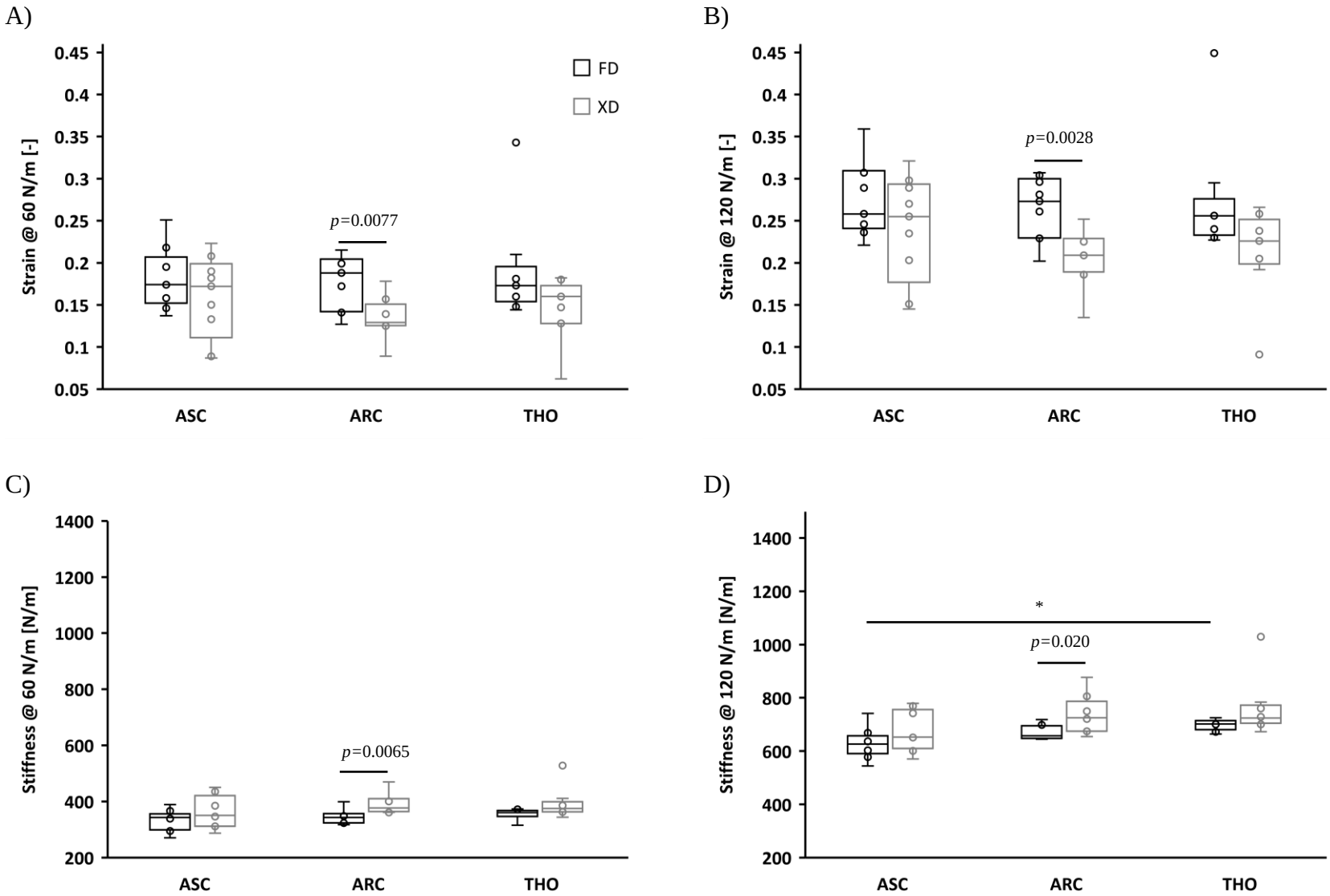

Figure 15 – Circumferential and longitudinal response in the ascending, arch and thoracic descending aorta – Guccione model A) Strain at 60 N/m; B) Strain at 120 N/m; C) Stiffness at 60 N/m D) Stiffness at 120 N/m. The p-value is specified where the FD and XD are significantly different. * Represents statistical significance between two regions.

4.1.5 Stress-Strain Plots

The average experimental data from all protocols for the ascending, arch and thoracic descending aorta are presented in Appendix C: Stress-Strain Curves (C.1). As a summary, Figure 16 shows averaged equibiaxial protocols for the anatomically relevant regions.

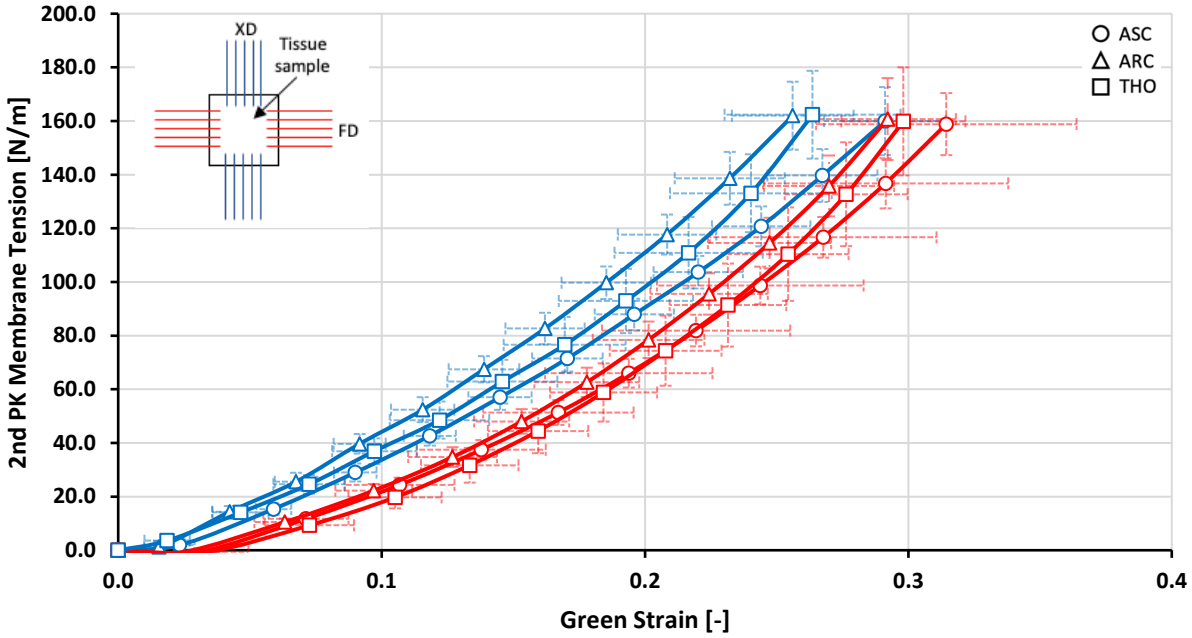

Figure 16 – Summary of the averaged experimental results for the Asc., Arc., and Tho., for the equibiaxial protocol. Both FD and XD are represented, for two curves for each anatomically relevant location ± standard deviation.

4.1.6 Material Constants

The material constants were determined using one representative circumferential location for each anatomically relevant region. Table 5 and Table 6 list the coefficients obtained from the simultaneous use of all averaged experimental protocols (1-9) for both the Fung and Guccione models, respectively. The material constants satisfy the strain energy convexity constraints, outlined in (Labrosse et al., 2016). The strong correlation between the experimental data and predicted curves is represented by the Pearson correlation coefficient (R^2). The average R^2 was

0.995 ± 0.005 for the Fung model, and 0.990 ± 0.0063 for the Guccione model; indicating an overall excellent match between experimental and predicted values.

Table 5 – Material constants for Fung model, derived from all protocols, ± the half span of the 95% confidence interval.

Material Constants	Regional Location		
	ASC	ARC	THO
c1 [N/m]	82.40 ± 1.94	70.37 ± 1.92	56.63 ± 1.54
c2 [-]	3.05 ± 0.06	3.58 ± 0.08	4.15 ± 0.08
c3 [-]	3.43 ± 0.06	4.40 ± 0.09	4.82 ± 0.10
c4 [-]	0.33 ± 0.01	0.53 ± 0.02	0.49 ± 0.02
c5 [-]	0.45 ± 2.67	0.00 ± 2.92	0.00 ± 7.16
c6 [-]	0.01± 0.03	0.01± 0.05	0.00 ± 0.04
c7 [-]	0.01 ± 0.04	-0.01 ± 0.03	0.00 ± 0.07
R^2-FD	1.00	1.00	1.00
R^2-XD	0.99	0.99	0.99

R^2-FD: Pearson correlation coefficient between the experimental and predicted membrane tensions in the fiber direction.
R^2-FD: Pearson correlation coefficient between the experimental and predicted membrane tensions in the cross-fiber direction.

Table 6 – Material constants for Guccione model, derived from all protocols, ± the half span of the 95% confidence interval.

Material Constants	Regional Location		
	ASC	ARC	THO
c1 [N/m]	34.00 ± 0.96	28.53 ± 0.84	24.96 ± 0.76
c2 [-]	3.93 ± 0.07	4.47 ± 0.08	4.76 ± 0.09
c3 [-]	4.45 ± 0.07	5.6 ± 0.10	5.70 ± 0.10
c4 [-]	0.00 ± 1.61	0.00 ± 3.28	0.02 ± 7.43
R^2-FD	1.00	0.99	0.98
R^2-XD	0.99	0.99	0.99

4.2 Experiment 2: Enzymatic Digestion

4.2.1 Enzymatic Digestion Optimization

Following the protocol outlined by (Mattson et al., 2017), 54.2 ± 5.8 % s-GAGs were removed from the samples after a 24 hour incubation period at 37°C. Doubling enzyme concentration within the buffer and decreasing incubation time to 4 hours at 37°C, GAG content was decreased by 40.1 ± 1.2%. Samples treated with 6-15 U/ml hyaluronidase, 0.075 U/ml chondroitinase ABC and

0.75 U/ml heparinase in 100 mM buffer, for 48 hours at 37°C revealed a 41.4 ± 20.4% and 89.6 ± 3.0% decrease in GAG concentration at 4- and 48-hours incubation, respectively. Herein, 4- and 48- hour incubation times are dubbed partial and near-complete digestion. The results of varying concentration and incubation time are summarized in Table 7 and Figure 17.

Table 7 – Results of increased enzyme concentration with varying incubation time ± standard deviation.

Incubation [hours]	Decrease in s-GAG content (%)		
	1x concentration	2x concentration	3x concentration
1	50.9 ± 18.3	23 ± 9.6	22.5 ± 12.7
2	48.4 ± 5.2	32.9 ± 0.49	39.0 ± 13.3
3	47.3 ± 9.9	29.2 ± 13.5	37.5 ± 6.1
4	50.8 ± 5.4	40.1 ± 1.2	41.4 ± 20.4
8	46.8 ± 6.8	–	–
24	54.2 ± 5.8	–	78.4 ± 1.7
48	–	–	89.6 ± 3.0

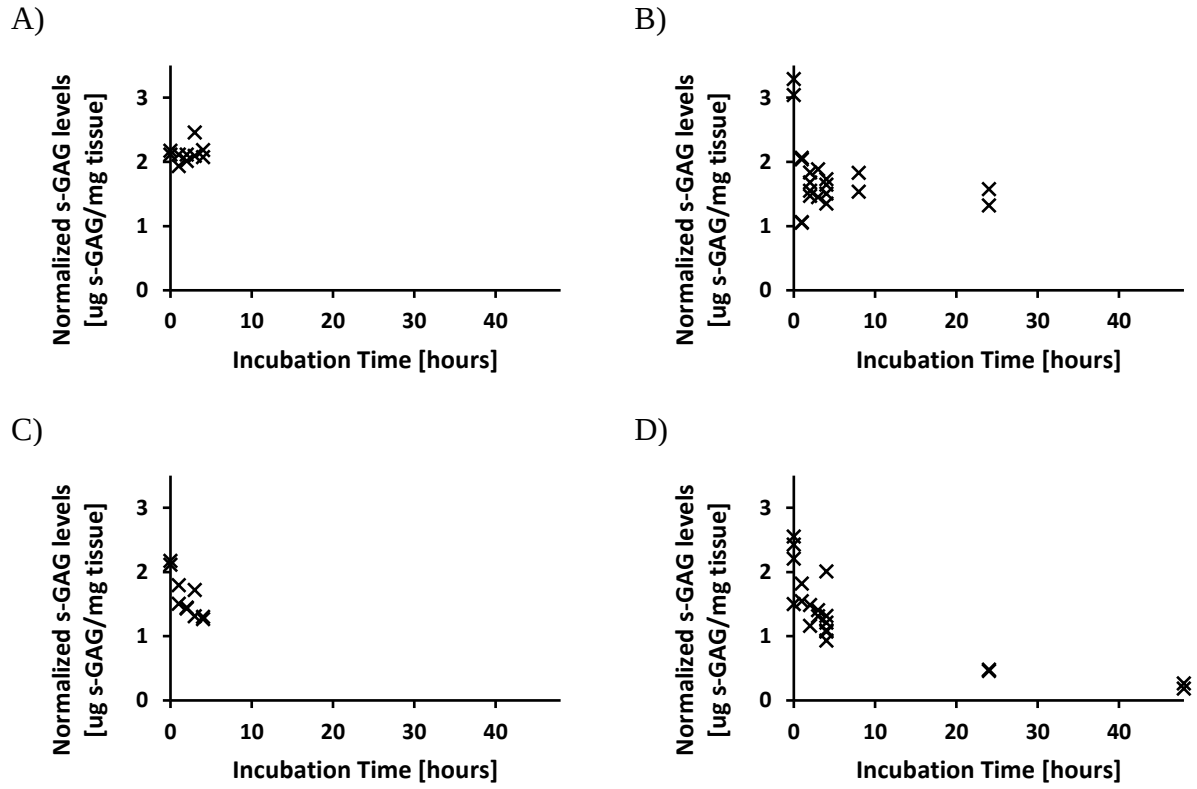

Figure 17 – A) 0x enzyme concentration. B) 1x enzyme concentration, 24-hour incubation period. C) 2x enzyme concentration, 4-hour incubation period. D) 3x enzyme concentration, 48-hour incubation period.

4.2.2 GAG Quantification

Partial and complete digestion of GAGs from the aortic wall was performed prior to mechanical testing. The results following incubation are recorded in Table 8. On average, 47.4 ± 17.9% and 84.1 ± 8.8% of GAGs were removed from the aortic wall after 4- and 48-hour incubation periods, respectively.

Table 8 – Decrease in s-GAG content (%) following 4- and 48- hour incubation in each region. Avg. decrease: control = average decrease in normalized s-GAG levels compared to the average s-GAG content at 0 hours, per region ± standard deviation.

Aorta ID	Decrease in s-GAG content (%)					
	Ascending Aorta		Aortic Arch		Thoracic Descending	
	4 hours	48 hours	4 hours	48 hours	4 hours	48 hours
1	28.2	82.4	54.3	90.2	52.4	91.7
2	32.4	84.2	33.7	90.4	60.6	95.6
3	74.8	83.6	50.3	90.1	43.0	86.0
4	39.1	87.6	55.1	94.4	12.0	88.4
5	-	77.8	24.7	80.1	58.6	87.4
6	10.1	50.6	65.6	87.7	73.0	79.0
7	47.7	68.4	53.0	86.6	51.7	89.4
8	69.1	86.8	51.7	95	53.7	66.2
Average	43.1 ± 22.9	77.7 ± 12.5	48.5 ± 13.1	89.3 ± 4.7	50.6 ± 17.8	85.5 ± 9.1

4.2.2.1 Untreated Tissue

GAGs were quantified both locally and regionally, to determine the distribution across the arterial wall, and along the length of the aorta. Local analysis of the arterial wall revealed higher quantities of GAGs in the intima than in the adventitia. The average GAG content in the intima and adventitia was 3.13 ± 1.18 and 1.21 ± 0.46 ug s-GAG/mg tissue, 2.65 ± 0.60 and 1.30 ± 0.58 ug GAG/mg tissue, and 2.15 ± 0.91 and 0.76 ± 0.45 ug s-GAG/mg tissue, in the ascending, arch and descending thoracic aorta, respectively. Significant regional variations were detected along the length of the aorta, using a one-way ANOVA (p=0.033) —the average GAG content in the ascending aorta was

1.81 ± 0.96 ug GAG/mg tissue, 1.62 ± 0.87 ug GAG/mg tissue in the arch and 1.28 ± 0.86 ug GAG/mg tissue in the descending thoracic. Refer to Figure 18.

4.2.2.2 4-hour Incubation

The zonal and regional distributions of GAGs were measured following 4-hour enzymatic digestion, since it t is known that GAGs are inhomogeneously distributed throughout the arterial wall, with increased concentration in the intimal and medial layers (Azeloglu et al., 2007). Consistent with the findings of the untreated samples, the concentration of GAGs was higher in the intima, compared to the adventitia. Average GAG levels in the intima were 1.91 ± 0.66, 1.08 ± 0.30 and 0.69 ± 0.27 ug GAG/mg tissue, in the ascending, arch and thoracic descending aorta, respectively. The GAG content in the adventitia, moving distally from the heart measured 0.79 ± 0.66, 0.46 ± 0.42 and 0.32 ± 0.21 ug GAG/mg tissue. The average concentration of GAGs significantly decreased along the length of the aorta, using a one-way ANOVA (p=0.0015). Refer to Figure 18.

4.2.2.3 48-hour Incubation

The zonal and regional distribution of GAGs were measured following 48-hour enzymatic digestion. Consistent with the findings of the untreated and partially digested samples, the complete enzymatic digestion of GAGs from arterial tissue revealed a non-uniform transmural distribution of GAGs; the concentration in the intima was greater than in the adventitia. Average GAG levels in the intima were 0.33 ± 0.089, 0.24 ± 0.077 and 0.23 ± 0.14 ug GAG/mg tissue, in the ascending, arch and thoracic descending aorta, respectively. The GAG content in the adventitia, moving distally from the heart revealed decreased levels, which measured: 0.59 ± 0.50, 0.24 ± 0.15 and 0.39 ± 0.53 ug GAG/mg tissue. A significantly higher concentration of GAGs was

detected in the ascending aorta, which decreased along the length of the artery, using a one-way ANOVA (p=0.0088). Refer to Figure 18.

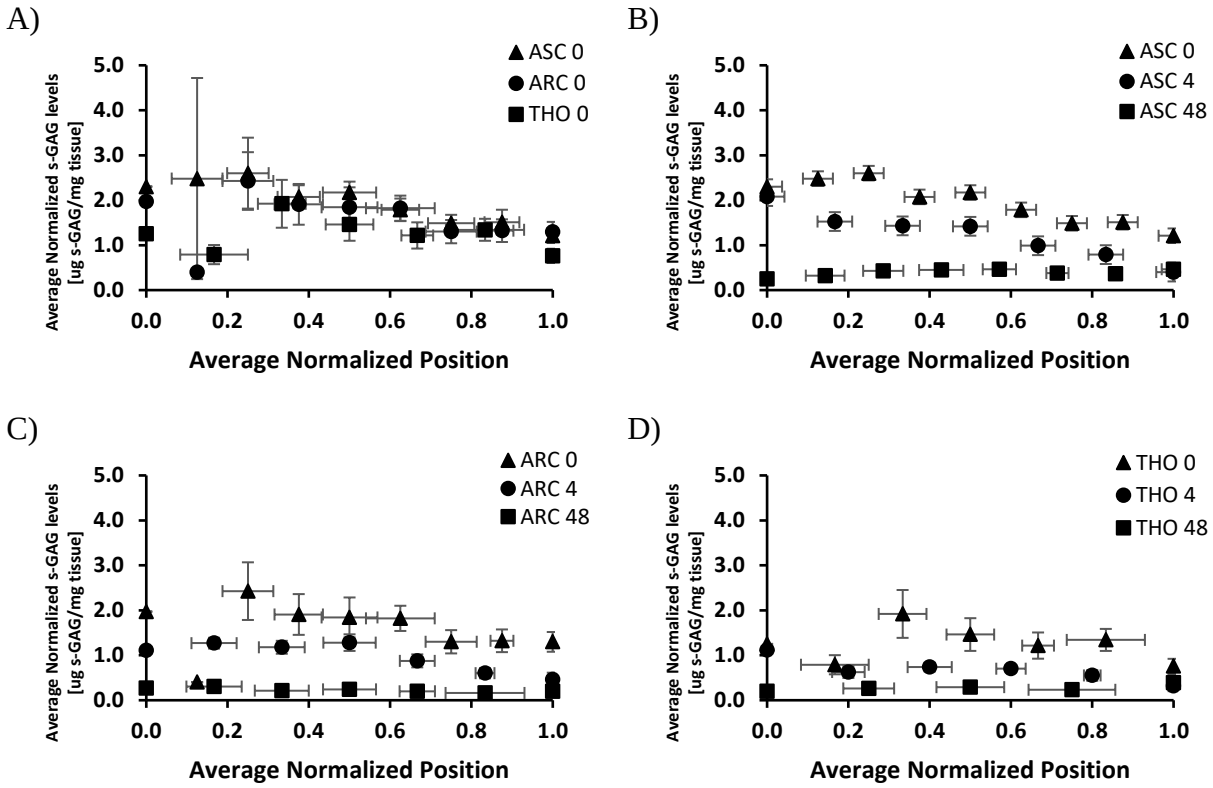

Figure 18 – Average normalized s-GAG levels A) in the Asc., Arc., and Tho.; B) in untreated, partially and fully GAG-digested tissue in the Asc.; C) Arc.; D) Tho., moving from the intima (0) to the adventitia (1) ± standard error of the mean.

4.2.3 Variations in Thickness and Area

Sample thickness was measured at 0-, 4- and 48- hour incubation—zero, partial and fully glycosaminoglycan depleted tissue, respectively. Table 9 summarizes the average thickness in the ascending, arch and thoracic descending region at varying levels of enzymatic digestion. In each anatomically relevant region, the wall thickness was independent of the incubation time, and no statistical differences were observed between untreated and treated samples. In contrast, regional differences were observed in wall thickness moving distally from the heart, consistent with the findings in Experiment 1. Variations in wall thickness revealed significantly thicker samples in the ascending aorta, compared to the descending aorta, and the arch compared to the descending aorta

at 0- and 48- hours incubation (p=9.4E-06 and p=2.9E-05, respectively, from one-way ANVOA), while 4-hour incubation yielded significant differences in average wall thickness between all regions (p=2.5E-06, from one-way ANOVA).

Table 9 – Average thickness of the Asc., Arc., Tho. at varying incubation times.

Regional Location	Average Thickness [mm] at Incubation Time [hours]		
	0	4	48
Ascending Aorta	2.11 ± 0.22	2.21 ± 0.24	1.86 ± 0.23
Aortic Arch	1.81 ± 0.29	1.71 ± 0.18	1.81 ± 0.18
Thoracic Descending Aorta	1.32 ± 0.22	1.37 ± 0.18	1.25 ± 0.24

In-plane sample dimensions were measured before and after enzymatic GAG removal treatment. Areas were calculated and averaged for each anatomically relevant region. Table 10 summarizes the average area of untreated and treated samples at 4- and 48- hour incubation periods, respectively. The partial and complete removal of GAGs from the arterial tissue did not influence the size of the sample, and/or result in dimensional changes. No significant differences were detected in the dimensions/area of the square sample, before and after treatment.

Table 10 – Average area of untreated (0 hour) and treated samples at varying incubation times in the Asc., Arc., and Tho.

	Average Area [mm^2]					
	Ascending Aorta		Aortic Arch		Thoracic Descending	
	4 hours	48 hours	4 hours	48 hours	4 hours	48 hours
Untreated	1.25 ± 0.09	1.23 ± 0.04	1.19 ± 0.05	1.21 ± 0.09	1.15 ± 0.10	1.12 ± 0.10
Treated	1.27 ± 0.08	1.25 ± 0.07	1.15 ± 0.02	1.21 ± 0.06	1.22 ± 0.04	1.13 ± 0.08

4.2.4 Mechanical Response: Untreated vs. Control

The mechanical response to loading, at membrane tensions of 60 and 120 N/m, was analyzed and used to compare tissue behaviour of control samples from Experiment 1 and untreated tissue in Experiment 2. The untreated tissue in Experiment 2 revealed directional dependency (Figure 19

and Figure 20); statistically significant differences in circumferential and longitudinal directions in the aortic arch and thoracic descending aorta were detected in both strain and stiffness, at 60 and 120 N/m tension, using the Fung and Guccione material models (Arc. E@60 N/m – Fung: p=0.00048, Arc. E@120 N/m – Fung: p=0.00042, Arc. S@60 N/m – Fung: p=0.0040, Arc. S@120 N/m – Fung: *p=0.0055,* Arc. E@60 N/m – Guccione: p=0.00051, Arc. E@120 N/m – Guccione: p=0.00033, Arc. S@60 N/m – Guccione: p=0.0019, Arc. S@120 N/m – Guccione: *p=0.0059,* Tho. E@60 N/m – Fung: p=0.0075, Tho. E@120 N/m – Fung: *p=0.0016,* Tho. S@60 N/m – Fung: p=0.012, Tho. S@120 N/m – Fung: *p=0.026,* Tho. E@60 N/m – Guccione: p=0.0019, Tho. E@120 N/m – Guccione: p=0.00044, Tho. S@60 N/m – Guccione: p=0.0025, Tho. S@120 N/m – Guccione: p=0.0030, from unpaired t-tests). Furthermore, one-way ANOVA revealed a trend towards increased stiffness moving distally away from the heart. The thoracic descending aorta was significantly stiffer (p=0.0035) than the ascending aorta in the circumferential direction, and stiffness in the thoracic descending and aortic arch was statistically greater (p=0.0019) in the longitudinal direction, compared to the ascending aorta, using the Fung model at 120 N/m. Similarly, stiffness was significantly greater (p=0.0046) in the thoracic and aortic arch, compared to the ascending aorta in the longitudinal direction, using the Guccione model at 120 N/m. The current findings reveal increased tissue anisotropy along the length of the aorta, a finding consistent with the results of Experiment 1.

4.2.5 Mechanical Properties: Untreated vs. Treated

Mechanical properties including stiffness and Green strain at 60 and 120 N/m tensions, in the circumferential and longitudinal directions were defined in the ascending, arch and thoracic descending regions of the porcine aorta. Q-Q plots were produced in conjunction with correlation coefficients to conclude normality among untreated, partially digested, and complete GAG

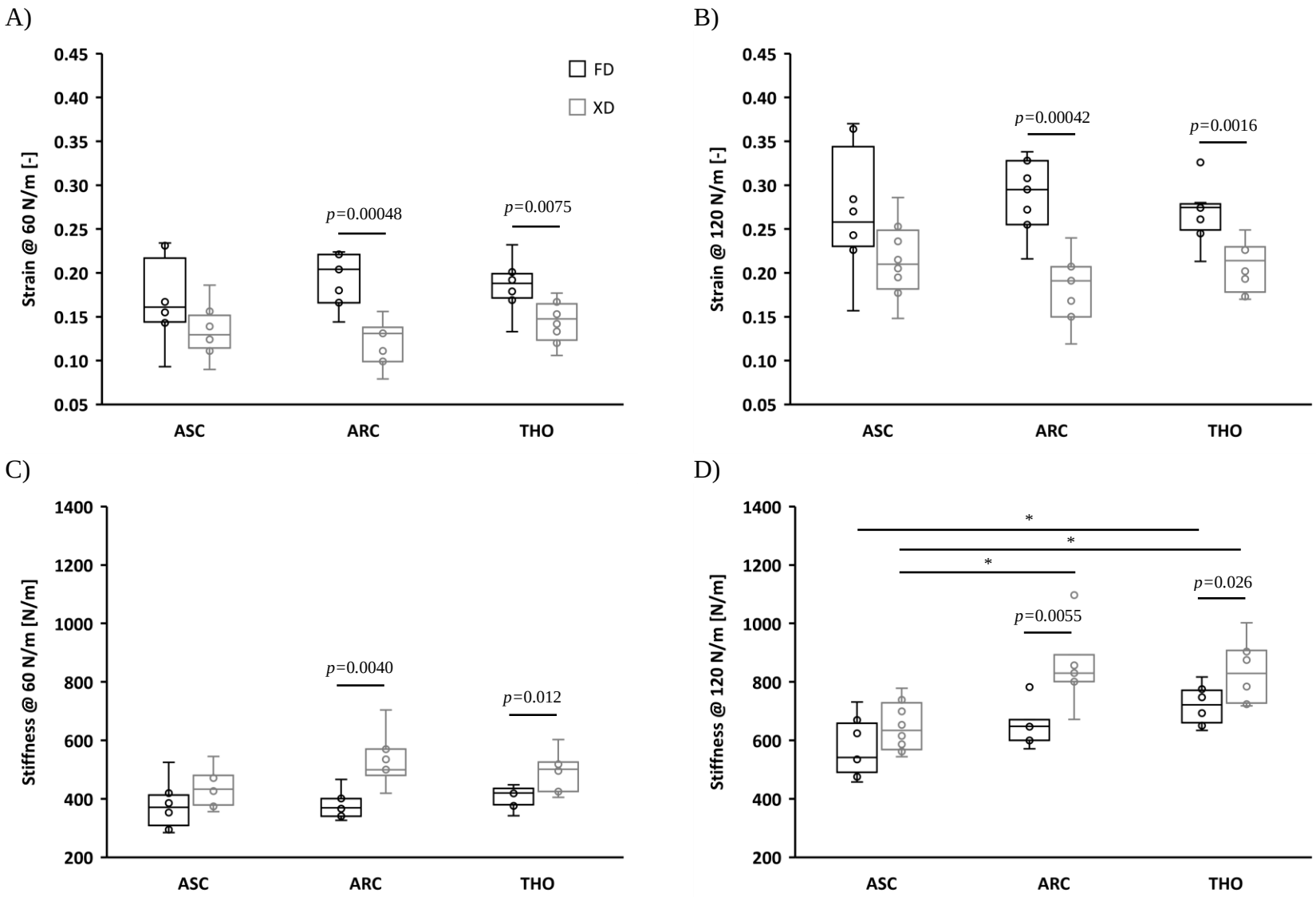

Figure 19 – Circumferential and longitudinal response of untreated tissue in the ascending, arch and thoracic descending aorta using the Fung model A) Strain at 60 N/m; B) Strain at 120 N/m; C) Stiffness at 60 N/m; D) Stiffness at 120 N/m. The p-value is specified where FD and XD are significantly different. * Represents statistical significance between two regions.

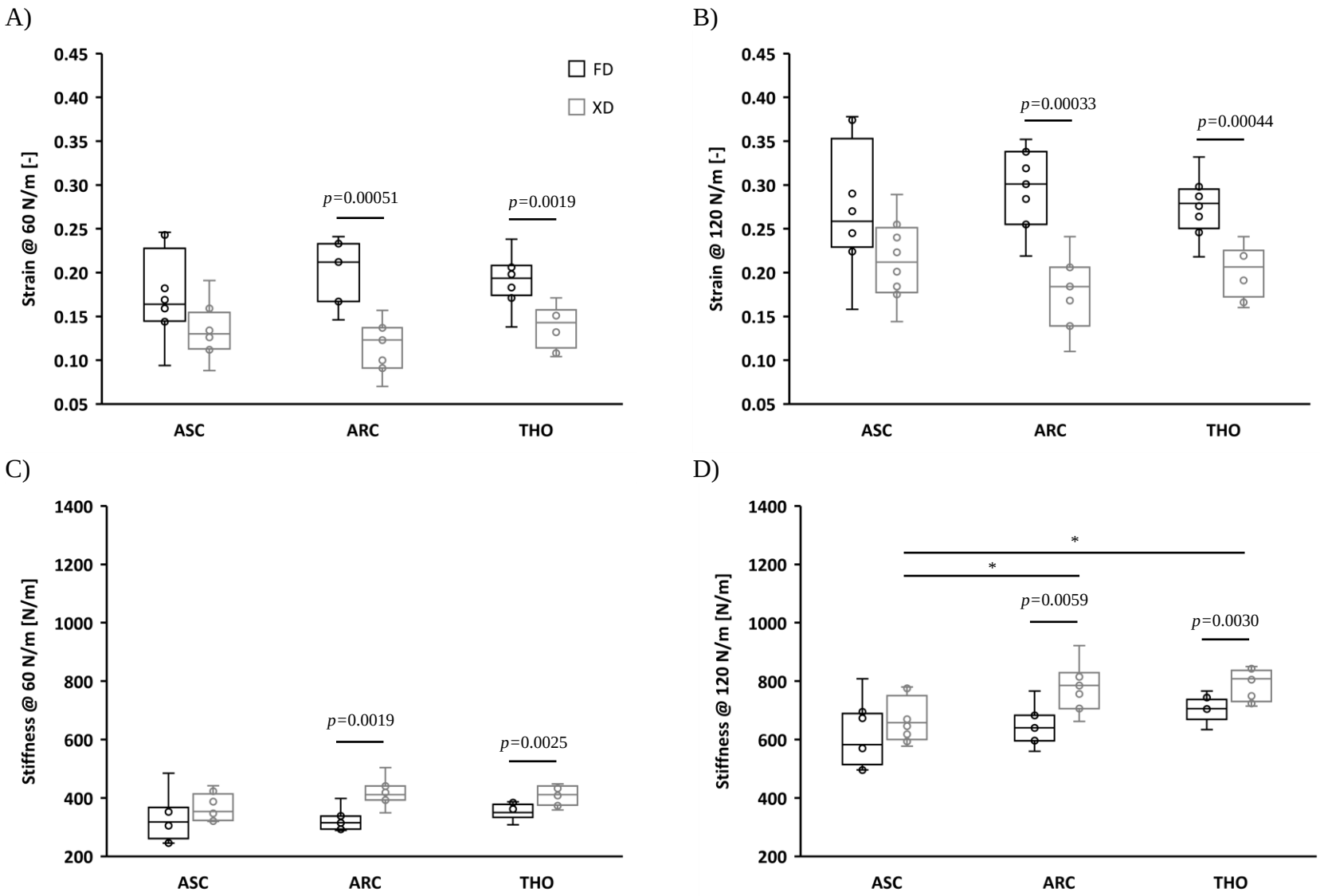

Figure 20 – Circumferential and longitudinal response of untreated tissue in the ascending, arch and thoracic descending aorta using the Guccione model A) Strain at 60 N/m; B) Strain at 120 N/m; C) Stiffness at 60 N/m; D) Stiffness at 120 N/m. The p-value is specified where FD and XD are significantly different. * Represents statistical significance between two regions.

digested tissue. Average strain and stiffness values, at varying incubation times, along the length of the aorta, are summarized for the Fung and Guccione models in Figure 21 and Figure 22, respectively (refer to Appendix B: Supplementary Results for data). One-way ANOVA with Tukey's test for post-hoc analysis revealed no statistical difference in stiffness and Green strain between the untreated and treated samples, in both the circumferential and longitudinal directions.

4.2.6 Regional and Directional Variations in Mechanical Properties

Comparing the circumferential and longitudinal directions, at 0-, 4- and 48-hours incubation, no directional variations were detected between the strains and stiffnesses at 60 and 120 N/m tensions, in the ascending aorta. Untreated and fully digested samples revealed statistically higher circumferential strain and longituindal stiffness (E@60 – 0 hours – Fung: p=0.00048, E@120 – 0 hours – Fung: p=0.00042, E@60 – 0 hours – Guccione: p=0.00051, E@120 – 0 hours – Guccione: p=0.00033, S@60 – 0 hours – Fung: p=0.0040, S@120 – 0 hours – Fung: p=0.0055, S@60 – 0 hours – Guccione: p=0.0019, S@120 – 0 hours – Guccione: p=0.0059, E@120 – 48 hours – Fung: p=0.020, E@120 – 48 hours – Guccione: p=0.020, S@120 – 48 hours – Fung: p=0.021, S@120 – 48 hours – Guccione: p=0.013) at 120 N/m, in the aortic arch; however, at 4-hours, no directional variations were detected. In the thoracic descending aorta, 0- and 4-hour incubation yielded a significantly lower stiffness in the circumferential direction (S@60 – 0 hours – Fung: p=0.012, S@120 – 0 hours – Fung: p=0.026, S@60 – 0 hours – Guccione: p=0.0025, S@120 – 0 hours – Guccione: p=0.0030, S@60 – 48 hours – Fung: p=0.0012, S@120 – 48 hours – Fung: p=0.0022, S@60 – 48 hours – Guccione: p=0.0013, S@120 – 48 hours – Guccione: p=0.0043) compared to the longitudinal direction. Identical directional trends were recorded using both the Fung and Guccione models. The ratios between strains and stiffness in two perpendicular directions are reported in the ascending aorta, compared to the arch, as well as in the thoracic descending region,

compared to the ascending aorta. The measured stiffness also increased, comparing the ascending region to the thoracic descending, at 120 N/m in the circumferential direction, Figure 21 and Figure 22. Table 11 and Table 12 illustrate the slight anisotropic behaviour of the aorta.

Regional variations in the mechanical response in the circumferential and longitudinal directions were observed, as expected, moving distally from the heart. One-way ANOVA with Tukey's post-hoc analysis revealed stiffer response along the length of the aorta. Specifically, at 0-hours, the stiffness in the longitudinal direction at 120 N/m was significantly higher in the arch and thoracic descending regions, compared to the ascending aorta, using both the Fung and Guccione models (Fung: p=0.0019, Guccione: p=0.0046). Additionally, the Fung model at 120 N/m in the circumferential direction revealed statistically greater stiffness in the thoracic descending aorta, compared to the ascending aorta (p=0.0035).

Similar trends were exhibited in tissue with partial and complete GAG depletion. At 4-hours, both the Fung and Guccione models yielded significantly higher stiffnesses in the arch and thoracic descending regions (p=0.00039, p=0.0032), compared to the ascending aorta at 120 N/m in the circumferential direction. The response in the longitudinal direction varied slightly; using the Guccione model, a significant difference was detected between ascending aorta and aortic arch (*p=0.00000059)*, compared to the thoracic descending, while the Fung model revealed increased stiffness only between the ascending aorta and aortic arch (p=0.000000081). Lastly, at 48-hours incubation, the increased stiffness moving distally was consistent with findings at 0- and 4-hours. The Fung and Guccione models displayed significantly stiffer response in the longitudinal direction at 120 N/m (p=0.011, p=0.021).

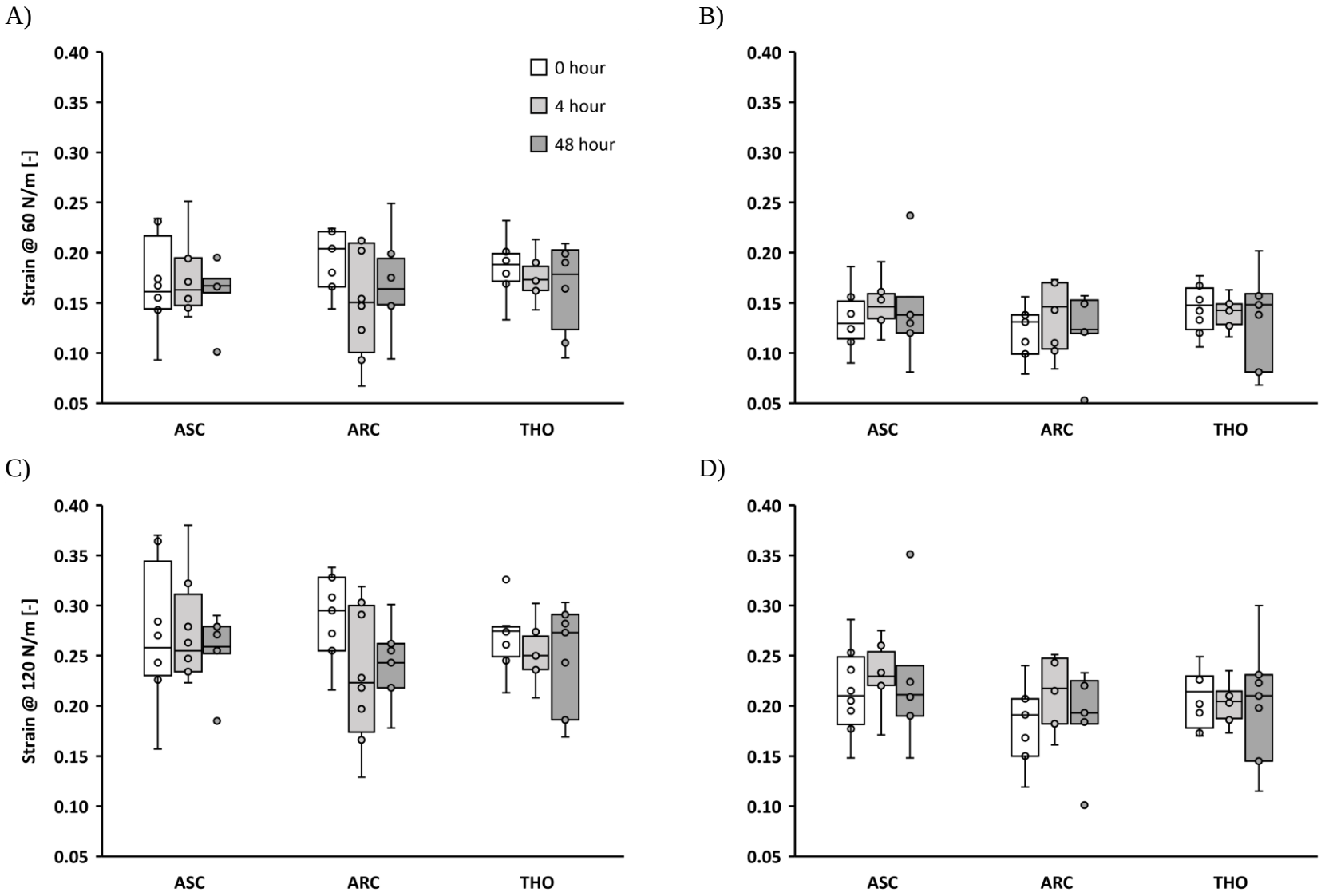

Figure 21 – Representative figures produced using the Fung model, comparing the response at 0-, 4- and 48-hours in the Asc., Arc., and Tho. A) Strain at 60 N/m in FD; B) Strain at 60 N/m in XD; C) Strain at 120 N/m in FD; D) Strain at 120 N/m in XD.

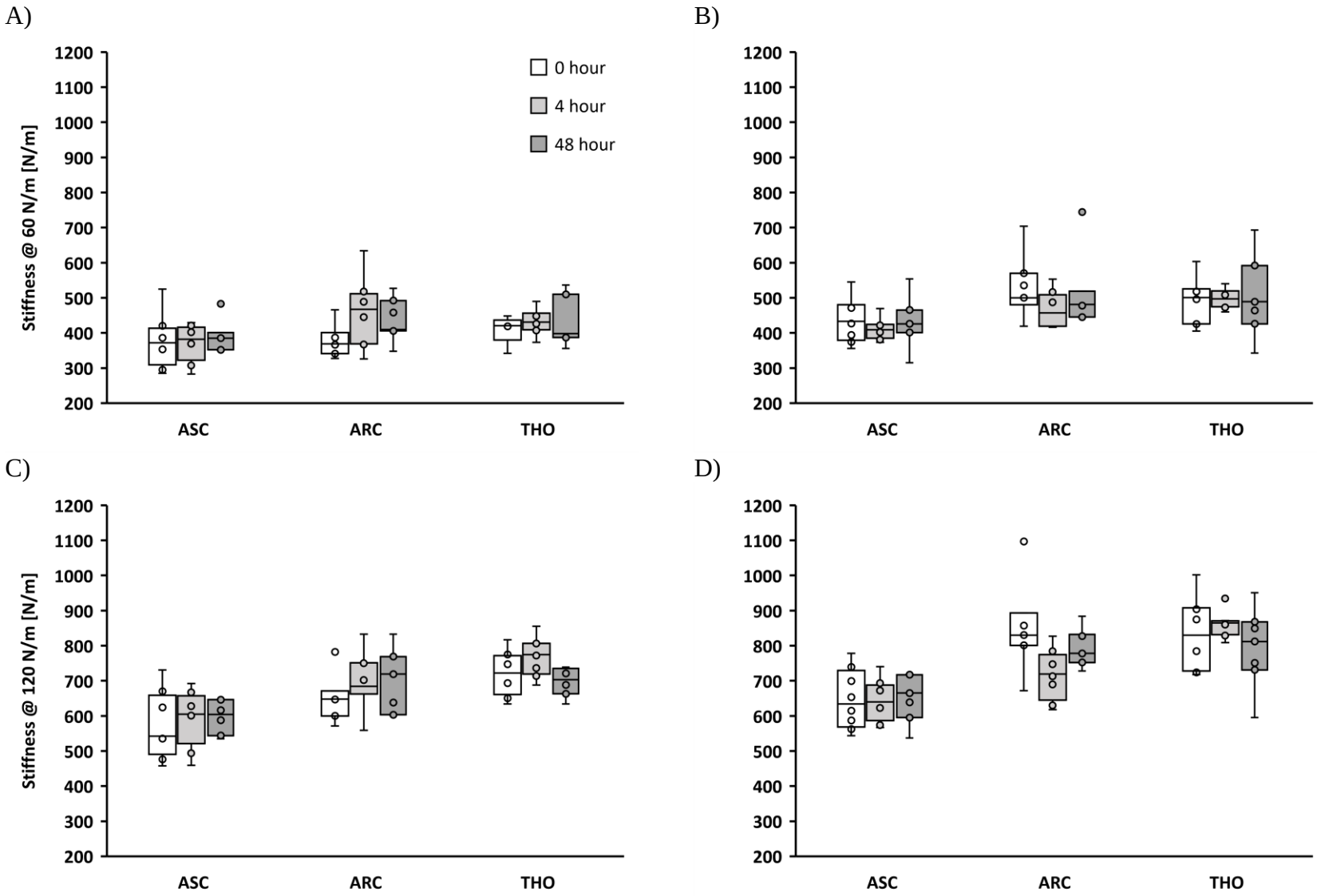

Figure 22 – Representative figures produced using the Guccione model, comparing the response at 0-, 4- and 48-hours in the Asc., Arc., and Tho. A) Stiffness at 60 N/m in FD; B) Stiffness at 60 N/m in XD; C) Stiffness at 120 N/m in FD; D) Stiffness at 120 N/m in XD.

The stiffness was greater in the ascending aorta, compared to the arch, as well as in the thoracic descending region, compared to the ascending aorta. The measured stiffness also increased, comparing the ascending region to the thoracic descending, at 120 N/m in the circumferential direction, Figure 21 and Figure 22.

Table 11 – Ratio of circumferential to longtiduinal strain and stiffness at 60 and 120 N/m respectively, using the Fung model.

Material Properties (Fung)	Incubation Time [hours]								
	ASC			ARC			THO		
	0	4	48	0	4	48	0	4	48
E_FD/E_XD@60N/m	1.26 ± 0.44	1.19 ± 0.31	1.13 ± 0.43	1.59 ± 0.42	1.10 ± 0.49	1.35 ± 0.51	1.28 ± 0.29	1.24 ± 0.20	1.23 ± 0.53
S_FD/S_XD@60N/m	0.86 ± 0.21	0.91 ± 0.14	0.90 ± 0.18	0.72 ± 0.15	0.98 ± 0.24	0.85 ± 0.21	0.84 ± 0.14	0.87 ± 0.09	0.85 ± 0.24
E_FD/E_XD@120N/m	1.26 ± 0.42	1.18 ± 0.28	1.14 ± 0.35	1.59 ± 0.42	1.09 ± 0.37	1.26 ± 0.36	1.29 ± 0.24	1.25 ± 0.18	1.23 ± 0.45
S_FD/S_XD@120N/m	0.88 ± 0.19	0.92 ± 0.15	0.92 ± 0.12	0.77 ± 0.14	0.97 ± 0.15	0.88 ± 0.13	0.87 ± 0.13	0.89 ± 0.08	0.88 ± 0.14

Table 12 – Ratio of circumferential to longtiduinal strain and stiffness at 60 and 120 N/m respectively, using the Guccione model.

Material Properties (Guccione)	Incubation Time [hours]								
	ASC			ARC			THO		
	0	4	48	0	4	48	0	4	48
E_FD/E_XD@60N/m	1.30 ± 0.49	1.20 ± 0.34	1.12 ± 0.44	1.72 ± 0.54	0.12 ± 0.50	0.14 ± 0.54	1.37 ± 0.32	1.31 ± 0.22	1.27 ± 0.57
S_FD/S_XD@60N/m	0.90 ± 0.24	0.93 ± 0.13	0.92 ± 0.18	0.78 ± 0.13	0.99 ± 0.26	0.87 ± 0.20	0.86 ± 0.10	0.89 ± 0.08	0.88 ± 0.22
E_FD/E_XD@120N/m	1.28 ± 0.45	1.18 ± 0.29	1.13 ± 0.35	1.68 ± 0.49	1.10 ± 0.37	1.26 ± 0.35	1.36 ± 0.26	1.30 ± 0.20	1.26 ± 0.47
S_FD/S_XD@120N/m	0.92 ± 0.19	0.94 ± 0.11	0.94 ± 0.11	0.82 ± 0.12	0.99 ± 0.11	0.90 ± 0.09	0.89 ± 0.08	0.91 ± 0.07	0.90 ± 0.12

4.2.7 Stress-Strain Plots

The average experimental data from all protocols for the ascending, arch and thoracic descending aorta at 0-, 4- and 48-hours incubation are presented in Appendix C: Stress-Strain Curves (C.2). As a summary, Figure 23 shows averaged equibiaxial protocols for the untreated and treated samples at anatomically relevant regions.

4.2.8 Material Constants

Table 13 and Table 14 list he coefficients obtained from the simultaneous use of all averaged experimental protocols (1-9) for both the Fung and Guccione models, respectively. The material

constants satisfy the strain energy convexity constraints, outlined in (Labrosse et al., 2016). The strong correlation between the experimental data and predicted curves is represented by the Pearson correlation coefficient (R^2). The average R^2 was 0.996 ±0.005 for the Fung model, and 0.988 ±0.004 for the Guccione model, indicating an overall excellent match between experimental and predicted values.

Table 13 – Material constants for Fung model, derived from all protocols, ± the half span of the 95% confidence interval, for untreated and treated samples.

Material Constants	Regional Location and Incubation Time [hours]								
	ASC			ARC			THO		
	0	4	48	0	4	48	0	4	48
c1 [N/m]	114.74 ± 3.25	90.67 ± 2.02	114.59 ± 3.64	53.80 ± 1.35	75.90 ± 1.97	74.10 ± 2.35	49.51 ± 1.31	48.29 ± 1.12	63.60 ± 1.66
c2 [-]	2.37 ± 0.05	2.78 ± 0.05	2.36 ± 0.06	4.11 ± 0.07	3.86 ± 0.08	3.46 ± 0.08	4.51 ± 0.09	4.90 ± 0.08	4.01 ± 0.08
c3 [-]	2.86 ± 0.07	3.17 ± 0.06	2.74 ± 0.07	6.12 ± 0.11	4.09 ± 0.08	4.63 ± 0.11	5.63 ± 0.11	5.92 ± 0.10	4.69 ± 0.09
c4 [-]	0.44 ± 0.01	0.48 ± 0.01	0.44 ± 0.02	0.60 ± 0.03	0.58 ± 0.02	0.66 ± 0.03	0.48 ± 0.03	0.59 ± 0.03	0.64 ± 0.02
c5 [-]	0.39 ± 3.19	0.01 ± 5.37	0.04 ± 0.70	0.00 ±. 3.16	0.00 ± 4.49	0.00 ± 1.79	0.00 ± 10.53	0.00 ± 14.02	0.11 ± 7.58
c6 [-]	-0.01 ± 0.02	0.01 ± 0.05	0.00 ± 0.02	0.01 ± 0.06	0.01 ± 0.08	0.01 ± 0.05	-0.01 ± 0.06	-0.01 ± 0.08	0.01 ± 0.06
c7 [-]	-0.01 ± 0.07	0.00 ± 0.04	0.01 ± 0.03	-0.01 ± 0.05	-0.01 ± 0.03	0.00 ± 0.05	0.00 ± 0.05	0.00 ± 0.07	0.01 ± 0.06
R^2-FD	1.00	1.00	1.00	1.00	1.00	1.00	1.00	1.00	1.00
R^2-XD	1.00	1.00	0.99	0.99	0.99	0.99	0.99	0.99	0.99

Table 14 – Material constants for Guccione model, derived from all protocols, ± the half span of the 95% confidence interval, for untreated and treated samples.

Material Constants	Regional Location and Incubation Time [hours]								
	ASC			ARC			THO		
	0	4	48	0	4	48	0	4	48
c1 [N/m]	41.03 ± 1.10	35.28 ± 0.86	41.16 ± 1.16	22.32 ± 0.70	31.30 ± 0.85	28.51 ± 0.87	22.44 ± 0.70	22.03 ± 0.64	26.73 ± 0.72
c2 [-]	3.56 ± 0.06	3.90 ± 0.06	3.63 ± 0.07	4.50 ± 0.08	4.96 ± 0.08	4.43 ± 0.08	4.76 ± 0.09	5.23 ± 0.09	4.87 ± 0.08
c3 [-]	4.41 ± 0.07	4.50 ± 0.07	4.22 ± 0.07	7.05 ± 0.12	5.34 ± 0.09	6.10 ± 0.11	6.32 ± 0.11	6.60 ± 0.11	5.87 ± 0.09
c4 [-]	0.00 ± 1.37	0.00 ± 1.86	0.00 ± 1.54	0.00 ± 2.50	0.63 ± 1.86	0.00 ± 1.18	1.25 ± 15.23	3.37 ± 13.02	0.00 ± 6.60
R^2-FD	0.99	0.99	0.99	0.98	0.99	0.99	0.98	0.98	0.99
R^2-XD	0.99	0.99	0.99	0.99	0.99	0.99	0.99	0.99	0.99

A)

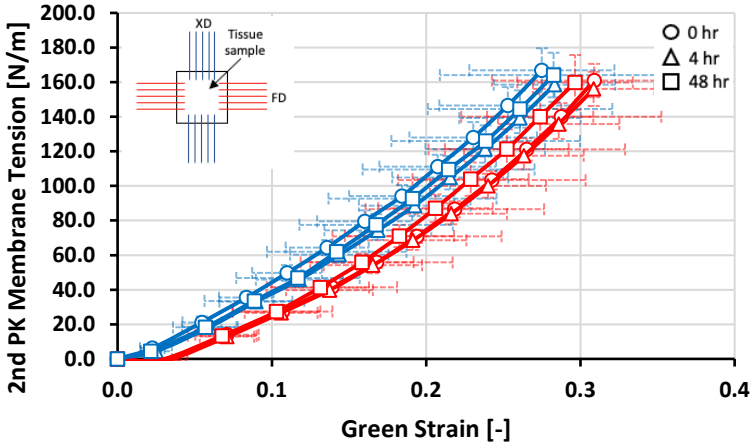

B)

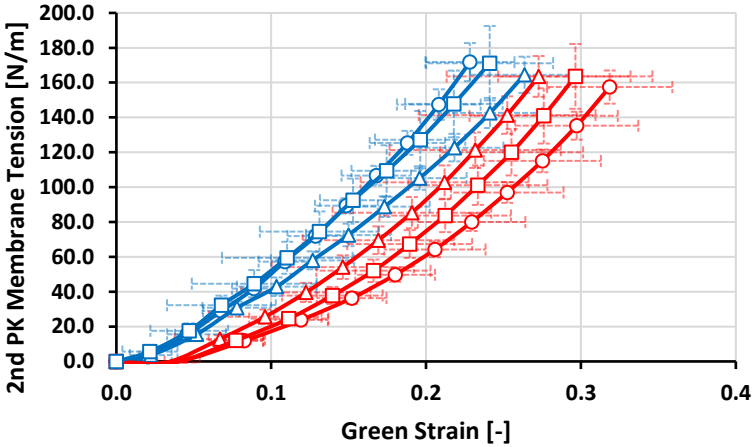

C)

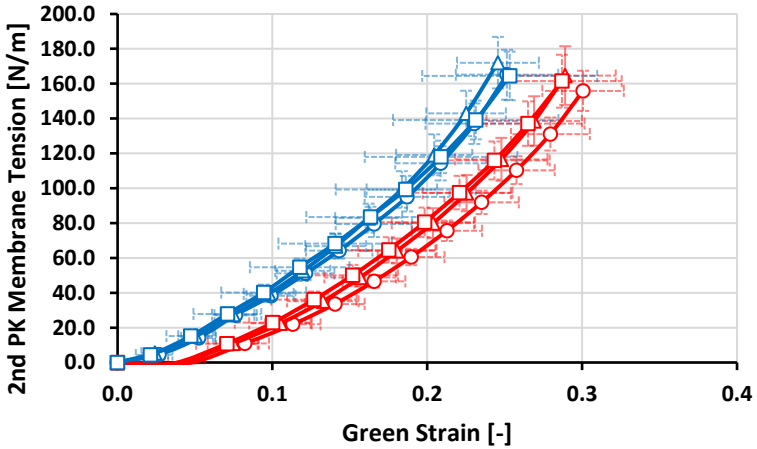

Figure 23 – Summary of the averaged experimental results, for the equibiaxial protocol, at 0-, 4-, and 48-hour incubation periods for the A) ascending aorta; B) aortic arch; C) thoracic descending aorta. Both FD and XD are represented, for two curves for each anatomically relevant location ± standard deviation.

5 Discussion

5.1 Experiment 1: Control Group

5.1.1 Circumferential and Regional Variations in Thickness

The present work revealed that tissue response was independent of location around the circumference, at three anatomically relevant regions; furthermore, one-way ANOVA confirmed no significant differences in tissue thickness, between the anterior, posterior and left and right lateral sides of the aorta. In agreement with this work, nonsignificant differences in wall thickness between the A, P, L, and R sides, and the A and P walls were reported in the human (Iliopoulos et al., 2009) and porcine (Deplano et al., 2016; Gundiah et al., 2008) ascending aorta, respectively. However, asymmetric aortic wall distention in healthy individuals (van Prehn et al., 2009), gradual changes in thickness along the porcine aortic wall circumference (Kim & Baek, 2011), and inconsistent distribution of elastic lamellae around the rat abdominal aorta circumference (O'Connell et al., 2008) have suggested that tissue behaviour is spatially dependent, due to variations in tissue composition, structure and morphometry.

As expected, morphometric analysis revealed a statistically significant decrease in tissue thickness moving from the ascending aorta to the aortic arch, and aortic arch to thoracic descending aorta, consistent with the findings of Jana et al. (2019) and Sokolis (2007). A steady decrease in tissue thickness, moving distally from the heart, may be attributed to a decrease in medial layer thickness to maintain a constant wall thickness-to-lumen ratio (Jana et al., 2019).

5.1.2 Circumferential Variations in Mechanical Properties

The GAG content and biomechanics of the healthy porcine aortic wall at three anatomically relevant regions: the ascending aorta, the aortic arch and the thoracic descending. Although it has been widely accepted that the mechanical properties of vessels vary along the length of the vascular

tree (Fung, 1993; Guo & Kassab, 2003; Han & Fung, 1995; Sokolis, 2007), circumferential variations are often overlooked due to assumed homogeneity. The present work revealed that various quadrants around the same circumference exhibited similar behaviour and tissue properties; the null-hypothesis of a one-way ANOVA test was accepted, implying no statistically significant differences in stiffness or strain between the anterior, posterior and left and right lateral sides of the aorta (Figure 12 and Figure 13). Nonsignificant differences in strain and stiffness responses were detected in all aortic regions in both the circumferential and longitudinal directions, at 60 and 120 N/m membrane tension. This finding suggests one representative circumferential sample from the A, P, L or R wall can be used to accurately describe the mechanical behaviour and tissue dimensions in a given anatomically relevant region of a healthy aorta.

Consistent with the results of the current study, Deplano et al. (2016) and Gundiah et al. (2008) highlighted the uniform mechanical response of samples excised from the anterior and posterior regions of the porcine ascending aorta. However, it is important to note that possible variations between the right and left lateral sides were not investigated in the aforementioned studies. Histomorphometric parameters of the aortic wall, including negligible variations in elastin and collagen content, and consistent intimal and medial layer thickness, imply no circumferential compositional heterogeneity (Iliopoulos et al., 2009). Since it is widely accepted that the mechanical behaviour of the aortic wall parallels tissue composition, fiber orientation and ECM structure (Fung, 1993; Holzapfel, 2008; Iliopoulos et al., 2009; Sherifova and & Holzapfel, 2020), it can be hypothesized that the homogeneity among these attributes contribute to the lack of mechanical variation circumferentially.

Nevertheless, the negligible differences in mechanical response in the circumferential region reported in this study and by Deplano et al. (2016) and Gundiah et al. (2008) in marked

contrast with the results of Kim & Baek (2011) who compared the mechanical behaviour and dimensions of the A, P, L, and R sides of the porcine descending aorta, and Nicosia et al. (2002) who evaluated variations in the A and P walls of the porcine ascending aorta. Spatial inhomogeneity with increased stiffness in the posterior region (Kim & Baek, 2011; Nicosia et al., 2002), suggest that tissue behaviour is spatially dependent, due to variations in tissue composition, structure and morphometry (O'Connell et al., 2008; van Prehn et al., 2009).

The independence of tissue stiffness with respect to circumferential location is still an area of contention in the literature. Deplano et al. (2016), Gundiah et al. (2008) and Nicosia et al. (2002) worked on the mechanical characterization of the porcine ascending aorta from biaxial testing, Kim & Baek (2011) utilized inflation testing on the proximal porcine thoracic descending aorta, and Iliopoulos et al. (2009) employed a uniaxial rig to test human ascending aorta specimens. Hence, potential discrepancies may be explained by the difficulties associated with making meaningful comparisons between the findings of the current study and reported data in literature, due to varying testing setups, protocols, stress/strain conditions and post-processing methods (Table 15).

5.1.3 Regional Variations in Mechanical Properties

The results of the present study imply regional dependency on mechanical and morphometric parameters, in agreement with many studies in the literature (Guo & Kassab, 2003; Han & Fung, 1995; Iliopoulos et al., 2009; Jana et al., 2019; Kim et al., 2013; Peña et al., 2018).

Segmental analysis along the length of the porcine aorta revealed variations in aortic mechanical response. Moving away from the heart, stiffness increased from the proximal to the distal aorta; significant stiffening along the vessel length was detected in the circumferential direction at 120 N/m tension, using the Fung and Guccione models (Figure 14, Figure 15).

Although aortic stiffness was not determined to significantly increase circumferentially or longitudinally at 60 N/m, likely the result of unengaged collagen fibers at low membrane tension, or at 120 N/m tension in the longitudinal direction, the overall trend towards greater stiffness distally is in agreement with Guo & Kassab (2003), Han & Fung (1995), Iliopoulos et al., (2009), Kim et al. (2013), and Peña et al. (2018). The aforementioned studies assessed segmental variations in the mechanical properties of various animal models and reported increased stiffness of the aortic wall along its length—a concept that is generally accepted (Fung, 1993).

Transmural assessment of the elastin network showed that elastin fiber orientation changes from a relatively uniform distribution close to the luminal surface, to a more circumferential distribution in the middle media, to a longitudinal distribution in regions close to the outer media (Yu et al., 2018), while multiphoton imaging by Mattson & Zhang (2017) revealed a uniform distribution of elastin. Significant variations in stiffness, specifically in the circumferential direction, may be attributed to an increase in circumferentially arranged collagen fibers in the medial layer, and a decrease in the elastin-to-collagen ratio, from the proximal to the distal aorta (Jana et al., 2019; Schriefl et al., 2012). While lower levels of stiffness proximally can be attributed to higher fractions of elastin (Tonar et al., 2015), it is hypothesized that a reduction in the required pulse dampening, limiting vessel elasticity and storage capacity, along the length of the aorta is a function of decreased elastin content; prompting an earlier transfer of mechanical load from elastin to collagen fibers, which are 100-1000 times stiffer (Wagenseil & Mecham, 2012). Furthermore, reduced amounts of elastin may alter ECM composition and arterial geometry, which ultimately lead to increased arterial stiffness.

5.1.4 Directional Variations in Mechanical Properties

The current work examined the directional variations in stiffness and Green strain in the ascending, arch and thoracic descending aorta at 60 and 120 N/m tension. The results did not yield statistically significant directional variations in the ascending and/or thoracic descending aorta (Figure 14, Figure 15). Similar circumferential and longitudinal responses implied a quasi-isotropic mechanical response in the aforementioned regions. However, in the thoracic descending aorta, the strain in the circumferential direction tended to be greater than in the longitudinal direction at 120 N/m—Fung (p=0.065) and Guccione (p=0.075) material models revealed a trend towards statistical significance. Furthermore, material behaviour was determined to be directionally dependent in the aortic arch; strain and stiffness were significantly greater circumferentially and longitudinally, respectively, at 60 and 120 N/m. Increased deviation from unity, with respect to strain and stiffness, distally suggests the mechanical response of the porcine aorta is slightly anisotropic away from the heart. Young porcine aortic walls exhibit fairly isotropic mechanical response, at low and high stress, consistent with Peña et al. (2018) and Choudhury et al. (2009) and Haskett et al. (2010), who examined tissue behaviour in the ascending porcine and human aorta, respectively. Furthermore, in agreement with this study, greater stiffness longitudinally, and increasing anisotropy, moving away from the heart, has been reported in the aged human heart (Haskett et al., 2010).

Deplano et al. (2016), Gundiah et al. (2008), Martin et al. (2011), Nicosia et al. (2002) and Shah et al. (2014), performed biaxial mechanical testing on porcine ascending aortas and reported directionally dependent and anisotropic mechanical response, with increased stiffness circumferentially than longitudinally. However, large variability in soft tissue response yielded significantly stiffer longitudinal than circumferential behaviour for 3/7 samples in the porcine

ascending aorta (Peña et al., 2018). In a review paper, de Beaufort et al. (2018) combined the mechanical response of equibiaxial stress-strain curves at 13.33 kPa (100 mmHg) in the ascending (Deplano et al., 2016; Martin et al., 2011; Shah et al., 2014) and descending (Marra et al., 2006; Polzer et al., 2015) porcine aorta; average circumferential and longitudinal stiffness were 0.42 ± 0.08 MPa and 0.37 ± 0.06 MPa, and 0.46 ± 0.03 and 0.44 ± 0.01 MPa, in the ascending and descending aorta, respectively (de Beaufort et al., 2018). The anisotropic index revealed a decrease in tissue anisotropy, moving along the length of the vascular tree, a finding that disagrees with current results and Peña et al. (2018), which report an increase in porcine tissue anisotropy with distance from the heart, at physiological loads (Figure 24). As previously stated, potential discrepancies in mechanical response of the aortic wall maybe due to the large variability of soft tissue response, and varying testing setups, protocols and conditions, refer to Table 15.

Significant structural and mechanical differences exist between the aged human heart and the porcine model; raising the question on the validity of using porcine models to investigate the diseased heart (Martin et al., 2011). Nevertheless, mechanical response of the young porcine aorta (4-10 months) has shown greater similarity to the young, healthy human aorta (<60 years), which exhibits no significant difference in directional stiffness (Choudhury et al., 2009; de Beaufort et al., 2018; Haskett et al., 2010; Marra et al., 2006). The quasi-isotropic response of the young porcine aorta is likely the result of age and the subsequent lack of mature collagen cross-links (Hayashi & Hirayama, 2017), bonds associated with a reduction in normal tissue elasticity (Lee & Cerami, 1992). (Haskett et al., 2010) hypothesized that the increased stiffness in the direction perpendicular to the preferred fiber orientation could be attributed to a loss in elasticity due to age, specifically in an axially oriented elastin network. A similar hypothesis cannot be made for the present findings, due to recent work which revealed transmural variation in elastin fiber

orientation, indicating an overall circumferential alignment (Yu et al., 2018). Inconsistency in the directional dependence results with the present work and the *ex-vivo* models described above may be attributed to different experimental conditions and protocols, refer to Table 15. The author speculates that the mechanical response of the porcine tissue may become directionally dependent with increased age, as the microstructure of the arterial wall varies, and mature collagen-cross links develop.

Table 15 – Summary of experimental methods including source, storage and protocol for various studies in the literature. Table adapted from (Deplano et al., 2016).

Ascending Aorta	Summary of test procedures on porcine aorta					
Author	Source	Age/Weight/Sex	Testing Method	Elapsed Time/storage	Protocol	Strain Measurement
(Nicosia et al., 2002)	SH	*/*/*	Biaxial	72 hours/4ºC	DC/Preload: */1:1, 1.7:1, 1.35:1, 1:1.35, 1:1.7	OPT, fa=15 Hz
(Gundiah et al., 2008)	SH	*/*/*	Biaxial	24 hours/ 4ºC	DC/1:1	OPT, fa=30 Hz
(Martin et al., 2011)	AC	6-9 months/*/*	Biaxial	Frozen at -80ºC	SC/Preload: */0.75:1, 0.5:1, 0.3:1, 1:1, 1:0.75, 1:0.5, 1:0.3	OPT, fa=*
(Shah et al., 2014)	SH	6 months/88 ±11.5 kg/Male	Biaxial	24 hours/4ºC	DC/Preload: 0.1 N/1:1	OPT, fa=*
(Deplano et al., 2016)	AC	4 months/27.9 ±3.6 kg/*	Biaxial	24 hours/4ºC	DC/0.75:1, 1:0.75, 0.5:1, 1:0.5, 0.25:1, 1:0.25, 1:1.	SDIC, fa=15.15, 7.56, 0.756 Hz
(Peña et al., 2018)	AC	3.5 ±0.6 months/*/Female	Biaxial	Frozen at -20 ºC	LC/0.5:0.5, 1:0.5, 0.5:1, 1:1, 2:1, 1:2, 2:2	DIC, fa=*
Present work	SH	5-6 months/90-105 kg/*	Biaxial	24 hours/4ºC	Refer to Table 2	OPT, fa=5Hz
Descending Aorta						
(Marra et al., 2006)	AC	4-5 months. **	Inflation	48 hours/4 ºC	Driving piston at 1mm/s	OPT, fa=5Hz (2.5Hz/camera)
(Polzer et al., 2015)	SH	10 months/105-120 kg/*	Biaxial	Frozen at -18 ºC	DC/Preload: 0.02 N/1:5, 1:2, 1:1, 2:1, 5:1	OPT, fa=*
(Peña et al., 2018)	AC	3.5 ±0.6 months/* /Female	Biaxial	Frozen at -20 ºC	LC/0.5:0.5, 1:0.5, 0.5:1, 1:1, 2:1, 1:2, 2:2	DIC, fa=*
Present work	SH	5-6 months/90-105 kg/*	Biaxial	24 hours/4ºC	Refer to Table 2	OPT, fa=5Hz

Abbreviations: SH: Slaughter House, AC: Animal Centre. *: Details not provided. DC: Displacement Control, SC: Stress Control, LC: Load Control. OPT: optical strain measurements using CCD camera, SDIC: Stereo Digital Image Correlation with speckle patterns and 2 CMOS cameras, DIC: Digital Image Correlation with speckle patterns and 1 CCD camera. fa: camera acquisition frequency.

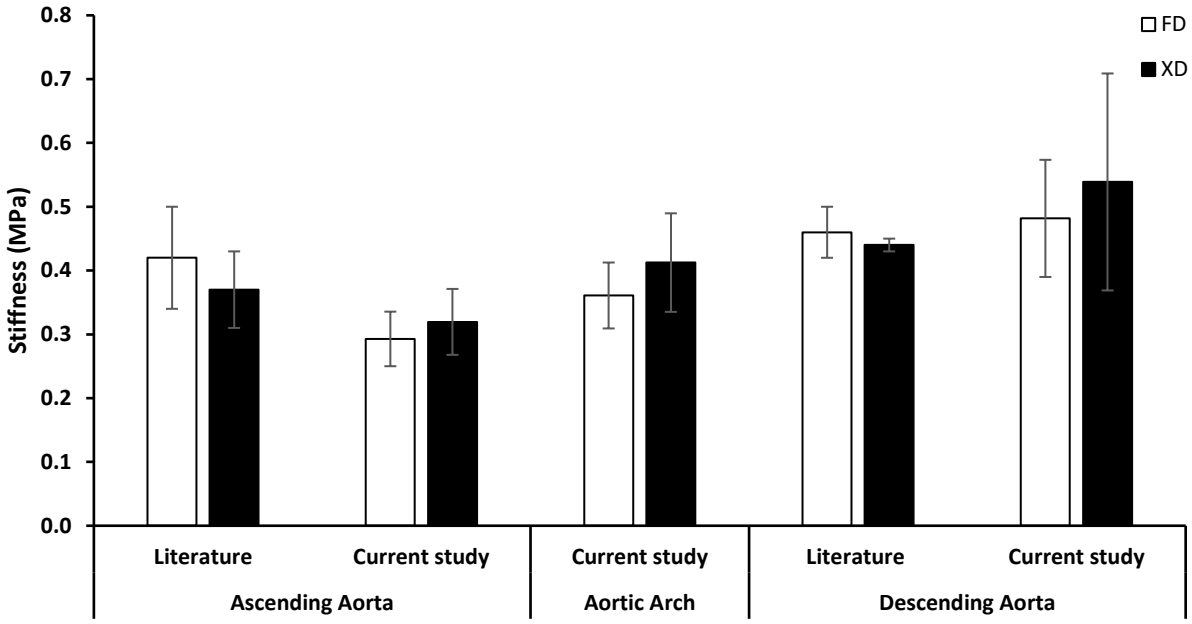

Figure 24 – Average equibiaxial stiffness values reported in literature (de Beaufort et al., 2018), compared to the findings of the current work, in anatomically relevant regions. Circumferential and longitduinal aortic stiffness were calculated corresponding to physiological pressure of 13.33 kPa (100 mmHg).

5.2 Experiment 2: Enzymatic Digestion

5.2.1 GAG Quantification

5.2.1.1 Untreated Tissue

Residual stresses develop in arteries to reduce stress gradients across wall thickness and are essential in maintaining an arterial homeostatic state (Chuong & Fung, 1986; Sigaeva et al., 2019). Heterogenous transmural distribution of GAGs induce Donnan swelling pressure, which provides a mechanism for regulating residual stresses (Azeloglu et al., 2008) and adapting to altered conditions, including pathological changes (Sigaeva et al., 2019). The heterogeneous transmural distribution of GAGs within the porcine arterial wall was quantified. The findings revealed higher concentrations of GAGs in the intima, decreasing from the inner layer to the adventitia, consistent with results of (Azeloglu et al., 2008; Gardais et al., 1973; Ghadie et al., 2020; Peña et al., 2015). Furthermore, regional variations were detected along the length of the aorta (Figure *18*); decrease

in GAG content from the proximal to distal aorta was expected due to a reported decrease in the opening angle distally (Rachev & Greenwald, 2003). GAG quantification revealed a regional dependency, suggesting lower residual stresses further away from the heart.

5.2.2 Variations in Thickness and Area

Morphometric parameters including tissue thickness and dimensions (length and width) were measured at 0-, 4- and 48-hours incubation, corresponding to zero, partial and complete enzymatic GAG removal treatments. The degradation of GAGs from the aortic tissue did not yield significant differences in sample thickness. Furthermore, the 9x9 mm square samples revealed no significant dimensional changes in length or width, following enzymatic degradation. To the best of the author's knowledge, this is the first study to assess dimensional changes associated with the treatment of GAG-depleting enzymes on arterial tissue. Remnant amounts of GAGs in the aortic wall, approximately 15.9 ± 3.9% (average), which remained after 48-hours, and hyaluronan may have contributed to the negligible variations in tissue morphometric parameters. The remaining GAGs, even in small quantities, likely serve to maintain tissue hydration properties, resist compressive loads and preserve the ECM structural network (Fessel & Snedeker, 2009).

Since GAGs occupy large volumes within the ECM, and expand significantly when hydrated, it was expected that partial and complete enzymatic degradation would yield an overall decrease in tissue thickness and dimensions, through the process of desiccation, resulting in a significant loss of water. Furthermore, (Lovekamp et al., 2006) who removed GAGs from porcine aortic cusps revealed a 20% decrease in tissue thickness, reduced amounts of water and an impaired ability to rehydrate. Both deficiency and accumulation of GAGs/PGs have been reported to influence tissue thickness (Humphrey, 2013; Lovekamp et al., 2006).

5.2.3 Mechanical Properties: Untreated vs. Control

Strain and stiffness of control tissue from Experiment 1 and untreated tissue (0-hour) from Experiment 2 revealed similar trends in regional and directional variations, although large variability exists in the mechanical response of soft tissues. Both control and untreated tissue, from Experiment 1 and 2, respectively, revealed an increase in material stiffness, moving distally, away from the heart. In addition, directional dependency of the aortic arch was consistent among both sets of data. Furthermore, the trend towards significant directional variations in the thoracic aorta, in Experiment 1, was consistent with findings in Experiment 2, which revealed significantly greater strain circumferentially and stiffness longitudinally, in the descending aorta, suggesting greater tissue anisotropy along the length of the aorta.

5.2.4 Mechanical Properties: Untreated vs. Treated

The present study integrates biomechanical characterization and spectrophotometric assays to determine how GAGs contribute to the biomechanical integrity of the porcine aorta, both proximal and distal to the heart. Biaxial tensile testing was employed to provide full characterization of the mechanical behaviour of the tissue, under repeatable, well-defined loading conditions. Overall, one-way ANOVA revealed no statistical difference in the mechanical response between 0-, 4- and 48-hours incubation, suggesting GAGs do not play a role in the mechanical response of aortic tissue, as measured from biaxial testing.

The strains and stiffnesses at set levels of tension, along with sample dimensions, reveal no change between the untreated and treated samples. In addition, equibiaxial stress-strain curves (Figure 23) confirm the results of the statistical analysis, since curves are plotted within standard deviations of each other.

5.2.5 Regional and Directional Variations in Mechanical Properties

While the overall effect of GAG digestion on the mechanical properties of the porcine aorta was negligible, as discussed in the previous section, there were observations of more subtle effects, as discussed now. The partial and complete GAG degradation altered the biomechanical behaviour and response of the tissue in the circumferential and longitudinal directions. After partial enzymatic removal, the response of the aortic arch was somewhat isotropic, while the thoracic descending region maintained significantly stiffer longitudinal than circumferential response. Interestingly, mechanical response to complete GAG removal was not consistent with the 4-hour incubation. At 48-hours, the arch revealed significant directional differences in stress and strain, while directional variations in the thoracic descending aorta were nonsignificant.

Consistent with the findings of untreated tissue, the aorta was significantly stiffer moving distally away from the heart at high pressure. While the untreated tissue only exhibited significant increased stiffening in the circumferential direction at 120 N/m, the partially and fully digested samples were significantly stiffer in both the circumferential and longitudinal directions. Since GAGs are associated with collagen fiber organization, it was noted that the removal of GAGs may have resulted in poorly organized fiber bundles with increased variation in fiber orientation. Non-uniform collagen fiber orientation may be the reason for significant increases in circumferential and longitudinal stiffness at 120 N/m, from the proximal to the distal aorta (Couchman & Pataki, 2012; Mattson et al., 2019).

6 Conclusion

6.1 General Comments

The methods presented allow for the successful and robust characterization of planar mechanical behaviour of untreated, partial, and fully GAG-depleted porcine aorta from the ascending, arch and thoracic descending aorta. The planar biaxial testing setup minimized shear deformations in the circumferential and longitudinal directions, illustrated in Appendix C: Stress-Strain Curves. Therefore, only the Pearson correlation coefficients for the circumferential and longitudinal directions are stated, as resulting stresses from shear are negligible compared to direct components. The Pearson correlation coefficients listed in Table 5, Table 6, Table 13, and Table 14 indicate an overall excellent match between experimental and predicted values, with the Fung and Guccione models. Because the same biaxial setup, testing protocols and post-processing software were used for untreated and treated samples, meaningful comparisons of mechanical behaviour and material constants between treatments can be made.

Evidenced in this report, the location around the circumference at a particular region, and the partial or complete enzymatic degradation of GAGs, from biaxial testing, do not influence mechanical properties or morphometric parameters. Therefore, it can be suggested that aortic tissue mechanical behaviour is independent of GAG contribution.

6.2 Clinical Relevance

Current interventions for aortic pathologies, including aneurysm and aortic dissection are not adequate. Hence, standards of medical care are shifting from a curative to a preventative approach by adopting an evidence-based medicine practice. Understanding the contributions of each component of the arterial wall to its mechanical response will aid in enhancing current models and

developing new mathematical models to help better predict arterial wall behaviour, especially of pathological tissue, as well as develop mechanically equivalent biomaterials to native tissues.

6.3 Limitations

Certain inconsistencies may have contributed to inaccuracies in obtaining data. The circumferential and longitudinal directions of the porcine aorta were determined by maintaining the circumferential and longitudinal orientation of the excised ring. Due to a lack of more accurate modalities, the orientation of the fibers may not have been precisely aligned circumferentially and axially. Identifying the circumferential regions: anterior, posterior, left and right lateral, was performed optically, which may have led to inconsistent identification of relevant locations. Another limitation was the DMMB assay used to quantify GAGs. DMMB only quantifies sulfated GAGs and disregards the hyaluronan content in the tissue, which may have contributed to aortic wall mechanical response. In the untreated aortic media, hyaluronan content has been reported between approximately 4-24% of total GAG content (Salisbury & Wagner, 1981). Although it is difficult to quantify the consequence of not detecting hyaluronan concentration following incubation, the remainder of any quantity of hyaluronan may result in a higher percentage of remaining GAGs, following what was assumed partial and complete degradation. Lastly, partial and complete enzymatic GAG degradation from tissue was 47.4 ± 17.9% and 84.1 ± 8.8%, respectively. Future work could focus on improving enzymatic GAG removal protocol.

6.4 Future Work

While the current work suggests that GAGs are mostly independent of aortic tissue mechanical behaviour as measured from biaxial testing, the quantification of the transmural distribution of GAGs, locally and regionally, supports the idea that GAGs do affect residual stresses in the aortic wall, as established from opening angle experiments (Azeloglu et al., 2008; Ghadie et al., 2020).

Therefore, numerical models should superimpose GAG-imposed swelling through osmotic pressure as a contributor to mechanical response independent of underlying material characteristics. These observations will contribute to the fundamental understanding of aortic tissue mechanics and help better determine the biomechanical relationship between individual arterial wall constituents and their response. Ultimately, future work will build on the current findings toward improved prediction of aortic wall rupture in aneurysm and aortic dissection.

7 References

Aird, W. C. (2007). Phenotypic Heterogeneity of the Endothelium. *Circulation Research*, *100*(2), 158–173. https://doi.org/10.1161/01.RES.0000255691.76142.4a

Al Jamal, R., Roughley, P. J., & Ludwig, M. S. (2001). Effect of glycosaminoglycan degradation on lung tissue viscoelasticity. *American Journal of Physiology-Lung Cellular and Molecular Physiology*, *280*(2), L306–L315. https://doi.org/10.1152/ajplung.2001.280.2.L306

Avril, S. (2018). Aortic and Arterial Mechanics. In M. R. Labrosse (Ed.), *Cardiovascular Mechanics* (1st ed., pp. 183–226). CRC Press. https://doi.org/10.1201/b21917-6

Ayad, S., Boot-Handford, R., Humphries, M., Kadler, K., & Shuttleworth, A. (1998). *The Extracellular Matrix Factsbook, Second Edition* (2 edition). Academic Press.

Azeloglu, E. U., Albro, M. B., Thimmappa, V. A., Ateshian, G. A., & Costa, K. D. (2008). Heterogeneous transmural proteoglycan distribution provides a mechanism for regulating residual stresses in the aorta. *American Journal of Physiology-Heart and Circulatory Physiology*, *294*(3), H1197–H1205. https://doi.org/10.1152/ajpheart.01027.2007

Bergström, J. (2015). Experimental Characterization Techniques. In *Mechanics of Solid Polymers* (pp. 19–114). Elsevier. https://doi.org/10.1016/B978-0-323-31150-2.00002-9

Brown, B. A., Williams, H., & George, S. J. (2017). Evidence for the Involvement of Matrix-Degrading Metalloproteinases (MMPs) in Atherosclerosis. In *Progress in Molecular Biology and Translational Science* (Vol. 147, pp. 197–237). Elsevier. https://doi.org/10.1016/bs.pmbts.2017.01.004

Brüel, A., Ørtoft, G., & Oxlund, H. (1998). Inhibition of cross-links in collagen is associated with reduced stiffness of the aorta in young rats. *Atherosclerosis*, *140*(1), 135–145. https://doi.org/10.1016/S0021-9150(98)00130-0

Carmo, M., Colombo, L., Bruno, A., Corsi, F. R. M., Roncoroni, L., Cuttin, M. S., Radice, F., Mussini, E., & Settembrini, P. G. (2002). Alteration of Elastin, Collagen and their Cross-links in Abdominal Aortic Aneurysms. *European Journal of Vascular and Endovascular Surgery*, *23*(6), 543–549. https://doi.org/10.1053/ejvs.2002.1620

Carpenter, L., & Best, J. (2013). *When Should an Abdominal Aortic Aneurysm Be Treated?* [Patient Care]. The Hospitalist. https://www.the-hospitalist.org/hospitalist/article/126034/when-should-abdominal-aortic-aneurysm-be-treated

Casale, J., & Crane, J. S. (2020). Biochemistry, Glycosaminoglycans. In *StatPearls*. StatPearls Publishing. http://www.ncbi.nlm.nih.gov/books/NBK544295/

Cattell, M. A., Hasleton, P. S., & Anderson, J. C. (1994). Glycosaminoglycan content is increased in dissecting aneurysms of human thoracic aorta. *Clinica Chimica Acta*, *226*(1), 29–46. https://doi.org/10.1016/0009-8981(94)90100-7

Chaves, E. W. V. (2013). Plasticity. In E. Oñate (Ed.), *Notes on Continuum Mechanics* (pp. 465–546). Springer Netherlands. https://doi.org/10.1007/978-94-007-5986-2_10

Choudhury, N., Bouchot, O., Rouleau, L., Tremblay, D., Cartier, R., Butany, J., Mongrain, R., & Leask, R. L. (2009). Local mechanical and structural properties of healthy and diseased human ascending aorta tissue. *Cardiovascular Pathology*, *18*(2), 83–91. https://doi.org/10.1016/j.carpath.2008.01.001

Chuong, C. J., & Fung, Y. C. (1986). On Residual Stresses in Arteries. *Journal of Biomechanical Engineering*, *108*(2), 189–192. https://doi.org/10.1115/1.3138600

Collins, J. A., Munoz, J.-V., Patel, T. R., Loukas, M., & Tubbs, R. S. (2014). The anatomy of the aging aorta: Anatomy of the Aging. *Clinical Anatomy*, *27*(3), 463–466. https://doi.org/10.1002/ca.22384

Couchman, J. R., & Pataki, C. A. (2012). An introduction to proteoglycans and their localization. *The Journal of Histochemistry and Cytochemistry: Official Journal of the Histochemistry Society*, *60*(12), 885–897. https://doi.org/10.1369/0022155412464638

Cowin, S. C., & Humphrey, J. D. (Eds.). (2001). *Cardiovascular Soft Tissue Mechanics*. Springer Netherlands. https://doi.org/10.1007/0-306-48389-0

Cramer, G. D. (2014). The Thoracic Region. In *Clinical Anatomy of the Spine, Spinal Cord, and Ans* (pp. 210–245). Elsevier. https://doi.org/10.1016/B978-0-323-07954-9.00006-2

de Beaufort, H. W. L., Ferrara, A., Conti, M., Moll, F. L., van Herwaarden, J. A., Figueroa, C. A., Bismuth, J., Auricchio, F., & Trimarchi, S. (2018). Comparative Analysis of Porcine and Human Thoracic Aortic Stiffness. *European Journal of Vascular and Endovascular Surgery*, *55*(4), 560–566. https://doi.org/10.1016/j.ejvs.2017.12.014

Deplano, V., Boufi, M., Boiron, O., Guivier-Curien, C., Alimi, Y., & Bertrand, E. (2016). Biaxial tensile tests of the porcine ascending aorta. *Journal of Biomechanics*, *49*(10), 2031–2037. https://doi.org/10.1016/j.jbiomech.2016.05.005

Driessen, N. J. B., Wilson, W., Bouten, C. V. C., & Baaijens, F. P. T. (2004). A computational model for collagen fibre remodelling in the arterial wall. *Journal of Theoretical Biology*, *226*(1), 53–64. https://doi.org/10.1016/j.jtbi.2003.08.004

Eckert, C. E., Fan, R., Mikulis, B., Barron, M., Carruthers, C. A., Friebe, V. M., Vyavahare, N. R., & Sacks, M. S. (2013). On the biomechanical role of glycosaminoglycans in the aortic heart valve leaflet. *Acta Biomaterialia*, *9*(1), 4653–4660. https://doi.org/10.1016/j.actbio.2012.09.031

Ernst, O., & Zor, T. (2010). Linearization of the Bradford Protein Assay. *Journal of Visualized Experiments : JoVE*, *38*. https://doi.org/10.3791/1918

Félétou, M. (2011). *The Endothelium: Part 1: Multiple Functions of the Endothelial Cells—Focus on Endothelium-Derived Vasoactive Mediators*. Morgan & Claypool Life Sciences. http://www.ncbi.nlm.nih.gov/books/NBK57149/

Fessel, G., & Snedeker, J. G. (2009). Evidence against proteoglycan mediated collagen fibril load transmission and dynamic viscoelasticity in tendon. *Matrix Biology*, *28*(8), 503–510. https://doi.org/10.1016/j.matbio.2009.08.002

Flamini, V., Kerskens, C., Simms, C., & Lally, C. (2013). Fibre orientation of fresh and frozen porcine aorta determined non-invasively using diffusion tensor imaging. *Medical Engineering & Physics*, *35*(6), 765–776. https://doi.org/10.1016/j.medengphy.2012.08.008

Frantz, C., Stewart, K. M., & Weaver, V. M. (2010). The extracellular matrix at a glance. *Journal of Cell Science*, *123*(24), 4195–4200. https://doi.org/10.1242/jcs.023820

Fung, Y.-C. (1993). *Biomechanics*. Springer New York. https://doi.org/10.1007/978-1-4757-2257-4

Ganong, W. F. (1981). *Review of Medical Physiology* (Tenth Edition edition). Lange.

Gardais, A., Picard, J., & Hermelin, B. (1973). Glycosaminoglycan (GAG) distribution in aortic wall from five species. *Comparative Biochemistry and Physiology Part B: Comparative Biochemistry*, *44*(2), 507–515. https://doi.org/10.1016/0305-0491(73)90025-4

Gasser, T. C., Ogden, R. W., & Holzapfel, G. A. (2006). Hyperelastic modelling of arterial layers with distributed collagen fibre orientations. *Journal of The Royal Society Interface*, *3*(6), 15–35. https://doi.org/10.1098/rsif.2005.0073

Ghadie, N., St-Pierre, J.-P., & Labrosse, M. R. (2020). Intramural Glycosaminoglycans Distribution vs. Residual Stress in Porcine Ascending Aorta: A Computational Study*. *2020 42nd Annual International Conference of the IEEE Engineering in Medicine Biology Society (EMBC)*, 2816–2819. https://doi.org/10.1109/EMBC44109.2020.9176381

Guccione, J. M., McCulloch, A. D., & Waldman, L. K. (1991). Passive Material Properties of Intact Ventricular Myocardium Determined From a Cylindrical Model. *Journal of Biomechanical Engineering*, *113*(1), 42–55. https://doi.org/10.1115/1.2894084

Gundiah, N., Matthews, P., Karimi, R., Azadani, A., Guccione, J., Guy, T., Saloner, D., & Tseng, E. (2008). Significant Material Property Differences Between the Porcine Ascending Aorta and Aortic Sinuses. *The Journal of Heart Valve Disease*, *17*, 606–613.

Guo, X., & Kassab, G. S. (2003). Variation of mechanical properties along the length of the aorta in C57bl/6 mice. *American Journal of Physiology-Heart and Circulatory Physiology*, *285*(6), H2614–H2622. https://doi.org/10.1152/ajpheart.00567.2003

Guyton, A. C. (1981). *Textbook of Medical Physiology 6th edition by Guyton, Arthur C. (1981) Hardcover* (6th edition). Saunders.

Han, H.-C., & Fung, Y.-C. (1995). Longitudinal strain of canine and porcine aortas. *Journal of Biomechanics*, *28*(5), 637–641. https://doi.org/10.1016/0021-9290(94)00091-H

Hao, H., Giulio, G., & Bochaton-Piallat, M.-L. (2003). Arterial Smooth Muscle Cell Heterogeneity. *Arteriosclerosis, Thrombosis, and Vascular Biology*, *23*(9), 1510–1520. https://doi.org/10.1161/01.ATV.0000090130.85752.ED

Haskett, D., Johnson, G., Zhou, A., & Utzinger, U. (2010). *Microstructural and biomechanical alterations of the human aorta as a function of age and location*. 12.

Hayashi, K., & Hirayama, E. (2017). Age-related changes of wall composition and collagen cross-linking in the rat carotid artery – In relation with arterial mechanics. *Journal of the Mechanical Behaviour of Biomedical Materials*, *65*, 881–889. https://doi.org/10.1016/j.jmbbm.2016.10.007

Heegaard, A.-M., Corsi, A., Danielsen, C. C., Nielsen, K. L., Jorgensen, H. L., Riminucci, M., Young, M. F., & Bianco, P. (2007). Biglycan Deficiency Causes Spontaneous Aortic Dissection and Rupture in Mice. *Circulation*, *115*(21), 2731–2738. https://doi.org/10.1161/CIRCULATIONAHA.106.653980

Holzapfel, G. A. (2000). Biomechanics of Soft Tissue. *Computational Biomechanics*, 15.

Holzapfel, G. A. (2008). Collagen in Arterial Walls: Biomechanical Aspects. In P. Fratzl (Ed.), *Collagen* (pp. 285–324). Springer US. https://doi.org/10.1007/978-0-387-73906-9_11

Holzapfel, G. A., Gasser, T. C., & Ogden, R. W. (2000). A New Constitutive Framework for Arterial Wall Mechanics and a Comparative Study of Material Models. *Journal of Elasticity and the Physical Science of Solids*, *61*(1), 1–48. https://doi.org/10.1023/A:1010835316564

Humphrey, J. D. (2002). *Cardiovascular Solid Mechanics: Cells, Tissues, and Organs*. Springer Science & Business Media.

Humphrey, J. D. (2013). Possible Mechanical Roles of Glycosaminoglycans in Thoracic Aortic Dissection and Associations with Dysregulated Transforming Growth Factor. *Journal of Vascular Research*, *50*(1), 1–10. https://doi.org/10.1159/000342436

Humphrey, J. D., & McCulloch, A. D. (2003). The Cardiovascular System—Anatomy, Physiology and Cell Biology. In G. A. Holzapfel & R. W. Ogden (Eds.), *Biomechanics of Soft Tissue in Cardiovascular Systems* (pp. 1–14). Springer Vienna. https://doi.org/10.1007/978-3-7091-2736-0_1

Humphrey, J. D., & Tellides, G. (2019). Central artery stiffness and thoracic aortopathy. *American Journal of Physiology-Heart and Circulatory Physiology*, *316*(1), H169–H182. https://doi.org/10.1152/ajpheart.00205.2018

Iliopoulos, D. C., Kritharis, E. P., Giagini, A. T., Papadodima, S. A., & Sokolis, D. P. (2009). Ascending thoracic aortic aneurysms are associated with compositional remodelling and vessel stiffening but not weakening in age-matched subjects. *The Journal of Thoracic and Cardiovascular Surgery*, *137*(1), 101–109. https://doi.org/10.1016/j.jtcvs.2008.07.023

Iozzo, R. V., & Schaefer, L. (2015). Proteoglycan form and function: A comprehensive nomenclature of proteoglycans. *Matrix Biology : Journal of the International Society for Matrix Biology*, *42*, 11–55. https://doi.org/10.1016/j.matbio.2015.02.003

Jana, S., Hu, M., Shen, M., & Kassiri, Z. (2019). Extracellular matrix, regional heterogeneity of the aorta, and aortic aneurysm. *Experimental & Molecular Medicine*, *51*(12), 1–15. https://doi.org/10.1038/s12276-019-0286-3

Jonker, F. H. W., Verhagen, H. J. M., Lin, P. H., Heijmen, R. H., Trimarchi, S., Lee, W. A., Moll, F. L., Athamneh, H., & Muhs, B. E. (2010). Outcomes of Endovascular Repair of Ruptured Descending Thoracic Aortic Aneurysms. *Circulation*, *121*(25), 2718–2723. https://doi.org/10.1161/CIRCULATIONAHA.109.908871

Kannus, P. (2000). Structure of the tendon connective tissue. *Scandinavian Journal of Medicine & Science in Sports*, *10*(6), 312–320. https://doi.org/10.1034/j.1600-0838.2000.010006312.x

Kelley, J. D., Kerndt, C. C., & Ashurst, J. V. (2021). Anatomy, Thorax, Aortic Arch. In *StatPearls*. StatPearls Publishing. http://www.ncbi.nlm.nih.gov/books/NBK499911/

Kim, J., & Baek, S. (2011). Circumferential variations of mechanical behaviour of the porcine thoracic aorta during the inflation test. *Journal of Biomechanics*, *44*(10), 1941–1947. https://doi.org/10.1016/j.jbiomech.2011.04.022

Kim, J., Hong, J.-W., & Baek, S. (2013). Longitudinal differences in the mechanical properties of the thoracic aorta depend on circumferential regions. *Journal of Biomedical Materials Research Part A*, *101A*(5), 1525–1529. https://doi.org/10.1002/jbm.a.34445

Kohn, J. C., Lampi, M. C., & Reinhart-King, C. A. (2015). Age-related vascular stiffening: Causes and consequences. *Frontiers in Genetics*, *06*. https://doi.org/10.3389/fgene.2015.00112

Krauss, G. (2001). Strengthening Mechanisms in Steels. In K. H. J. Buschow, R. W. Cahn, M. C. Flemings, B. Ilschner, E. J. Kramer, S. Mahajan, & P. Veyssière (Eds.), *Encyclopedia of Materials: Science and Technology* (pp. 8870–8881). Elsevier. https://doi.org/10.1016/B0-08-043152-6/01595-3

Labrosse, M. R., Jafar, R., Ngu, J., & Boodhwani, M. (2016). Planar biaxial testing of heart valve cusp replacement biomaterials: Experiments, theory and material constants. *Acta Biomaterialia*, *45*, 303–320. https://doi.org/10.1016/j.actbio.2016.08.036

Ladich, E., Butany, J., & Virmani, R. (2016). Aneurysms of the Aorta. In *Cardiovascular Pathology* (pp. 169–211). Elsevier. https://doi.org/10.1016/B978-0-12-420219-1.00005-7

Lee, A. T., & Cerami, A. (1992). Role of glycation in aging. *Annals of the New York Academy of Sciences*, *663*, 63–70. https://doi.org/10.1111/j.1749-6632.1992.tb38649.x

Linka, K., Khiêm, V. N., & Itskov, M. (2016). Multi-scale modelling of soft fibrous tissues based on proteoglycan mechanics. *Journal of Biomechanics*, *49*(12), 2349–2357. https://doi.org/10.1016/j.jbiomech.2016.02.049

Lovekamp, J. J., Simionescu, D. T., Mercuri, J. J., Zubiate, B., Sacks, M. S., & Vyavahare, N. R. (2006). Stability and function of glycosaminoglycans in porcine bioprosthetic heart valves. *Biomaterials*, *27*(8), 1507–1518. https://doi.org/10.1016/j.biomaterials.2005.08.003

Marra, S. P., Kennedy, F. E., Kinkaid, J. N., & Fillinger, M. F. (2006). Elastic and Rupture Properties of Porcine Aortic Tissue Measured Using Inflation Testing. *Cardiovascular Engineering*, *6*(4), 123–131. https://doi.org/10.1007/s10558-006-9021-5

Martin, C., Pham, T., & Sun, W. (2011). Significant differences in the material properties between aged human and porcine aortic tissues. *European Journal of Cardio-Thoracic Surgery*, *40*(1), 28–34. https://doi.org/10.1016/j.ejcts.2010.08.056

Martufi, G., & Gasser, T. C. (2012). Turnover of fibrillar collagen in soft biological tissue with application to the expansion of abdominal aortic aneurysms. *Journal of The Royal Society Interface*, *9*(77), 3366–3377. https://doi.org/10.1098/rsif.2012.0416

Martyn, C. N., & Greenwald, S. E. (1997). Impaired synthesis of elastin in walls of aorta and large conduit arteries during early development as an initiating event in pathogenesis of systemic hypertension. *THE LANCET*, *350*, 3.

Mattson, J. M., Turcotte, R., & Zhang, Y. (2017). Glycosaminoglycans contribute to extracellular matrix fiber recruitment and arterial wall mechanics. *Biomechanics and Modelling in Mechanobiology*, *16*(1), 213–225. https://doi.org/10.1007/s10237-016-0811-4

Mattson, J. M., Wang, Y., & Zhang, Y. (2019). Contributions of Glycosaminoglycans to Collagen Fiber Recruitment in Constitutive Modelling of Arterial Mechanics. *Journal of Biomechanics*, *82*, 211–219. https://doi.org/10.1016/j.jbiomech.2018.10.031

Mattson, J. M., & Zhang, Y. (2017). Structural and Functional Differences Between Porcine Aorta and Vena Cava. *Journal of Biomechanical Engineering*, *139*(7), 071007. https://doi.org/10.1115/1.4036261

Mayo Clinic. (2016). *Cardiac catheterization procedure approaches*. Mayo Clinic. https://www.mayoclinic.org/diseases-conditions/spontaneous-coronary-artery-dissection/multimedia/cardiac-catheter-procedure-approaches/img-20239890

Mccullagh, K. A., & Balian, G. (1975). Collagen characterisation and cell transformation in human atherosclerosis. *Nature*, *258*(5530), 73–75. https://doi.org/10.1038/258073a0

Mundi, S., Massaro, M., Scoditti, E., Carluccio, M. A., van Hinsbergh, V. W. M., Iruela-Arispe, M. L., & De Caterina, R. (2018). Endothelial permeability, LDL deposition, and cardiovascular risk factors—A review. *Cardiovascular Research*, *114*(1), 35–52. https://doi.org/10.1093/cvr/cvx226

Murata, K., Motayama, T., & Kotake, C. (1986). Collagen types in various layers of the human aorta and their changes with the atherosclerotic process. *Atherosclerosis*, *60*(3), 251–262. https://doi.org/10.1016/0021-9150(86)90172-3

Murata, K., Nakazawa, K., & Hamai, A. (1975). Distribution of acidic glycosaminoglycans in the intima, media and adventitia of bovine aorta and their anticoagulant properties. *Atherosclerosis*, *21*(1), 93–103. https://doi.org/10.1016/0021-9150(75)90096-9

Nasopoulou, A., Shetty, A., Lee, J., Nordsletten, D., Rinaldi, C. A., Lamata, P., & Niederer, S. (2017). Improved identifiability of myocardial material parameters by an energy-based cost function. *Biomechanics and Modelling in Mechanobiology*, *16*(3), 971–988. https://doi.org/10.1007/s10237-016-0865-3

Nataatmadja, M. (2006). Overexpression of Transforming Growth Factor- Is Associated With Increased Hyaluronan Content and Impairment of Repair in Marfan Syndrome Aortic Aneurysm. *Circulation*, *114*(1_suppl), I-371-I–377. https://doi.org/10.1161/CIRCULATIONAHA.105.000927

Nicosia, M. A., Kasalko, J. S., Cochran, R. P., Einstein, D. R., & Kunzelman, K. S. (2002). Biaxial mechanical properties of porcine ascending aortic wall tissue. *Journal of Heart Valve Disease*, *11*(5), 680–687. Scopus.

O'Connell, M. K., Murthy, S., Phan, S., Xu, C., Buchanan, J., Spilker, R., Dalman, R. L., Zarins, C. K., Denk, W., & Taylor, C. A. (2008). The Three-Dimensional Micro- and Nanostructure of the Aortic Medial Lamellar Unit Measured Using 3D Confocal & Electron Microscopy Imaging. *Matrix Biology : Journal of the International Society for Matrix Biology*, *27*(3), 171–181. https://doi.org/10.1016/j.matbio.2007.10.008

Peltonen, L., Halila, R., & Ryhänen, L. (1985). Enzymes converting procollagens to collagens: Procollagen to Collagen Conversion. *Journal of Cellular Biochemistry*, *28*(1), 15–21. https://doi.org/10.1002/jcb.240280104

Peña, J. A., Corral, V., Martínez, M. A., & Peña, E. (2018). Over length quantification of the multiaxial mechanical properties of the ascending, descending and abdominal aorta using Digital Image Correlation. *Journal of the Mechanical Behaviour of Biomedical Materials*, *77*, 434–445. https://doi.org/10.1016/j.jmbbm.2017.10.007

Peña, J. A., Martínez, M. A., & Peña, E. (2015). Layer-specific residual deformations and uniaxial and biaxial mechanical properties of thoracic porcine aorta. *Journal of the Mechanical Behaviour of Biomedical Materials*, *50*, 55–69. https://doi.org/10.1016/j.jmbbm.2015.05.024

Polzer, S., Gasser, T. C., Novak, K., Man, V., Tichy, M., Skacel, P., & Bursa, J. (2015). Structure-based constitutive model can accurately predict planar biaxial properties of aortic wall tissue. *Acta Biomaterialia*, *14*, 133–145. https://doi.org/10.1016/j.actbio.2014.11.043

Rachev, A., & Greenwald, S. E. (2003). Residual strains in conduit arteries. *Journal of Biomechanics*, *36*(5), 661–670. https://doi.org/10.1016/S0021-9290(02)00444-X

Robinson, P. S., Lin, T. W., Reynolds, P. R., Derwin, K. A., Iozzo, R. V., & Soslowsky, L. J. (2004). Strain-rate sensitive mechanical properties of tendon fascicles from mice with genetically engineered alterations in collagen and decorin. *Journal of Biomechanical Engineering*, *126*(2), 252–257. https://doi.org/10.1115/1.1695570

Rodriguez, C., Martinez-Gonzalez, J., Raposo, B., Alcudia, J. F., Guadall, A., & Badimon, L. (2008). Regulation of lysyl oxidase in vascular cells: Lysyl oxidase as a new player in cardiovascular diseases. *Cardiovascular Research*, *79*(1), 7–13. https://doi.org/10.1093/cvr/cvn102

Sacks, M. S. (2000). Biaxial Mechanical Evaluation of Planar Biological Materials. *Journal of Elasticity and the Physical Science of Solids*, *61*(1), 199. https://doi.org/10.1023/A:1010917028671

Salisbury, B. G., & Wagner, W. D. (1981). Isolation and preliminary characterization of proteoglycans dissociatively extracted from human aorta. *Journal of Biological Chemistry*, *256*(15), 8050–8057. https://doi.org/10.1016/S0021-9258(18)43386-8

Schriefl, A. J., Zeindlinger, G., Pierce, D. M., Regitnig, P., & Holzapfel, G. A. (2012). Determination of the layer-specific distributed collagen fibre orientations in human thoracic and abdominal aortas and common iliac arteries. *Journal of The Royal Society Interface*, *9*(71), 1275–1286. https://doi.org/10.1098/rsif.2011.0727

Shah, S. B., Witzenburg, C., Hadi, M. F., Wagner, H. P., Goodrich, J. M., Alford, P. W., & Barocas, V. H. (2014). Prefailure and Failure Mechanics of the Porcine Ascending Thoracic Aorta: Experiments and a Multiscale Model. *Journal of Biomechanical Engineering*, *136*(021028). https://doi.org/10.1115/1.4026443

Shekhonin, B. V., Domogatsky, S. P., Muzykantov, V. R., Idelson, G. L., & Rukosuev, V. S. (1985). Distribution of Type I, III, IV and V Collagen in Normal and Atherosclerotic Human Arterial Wall: Immunomorphological Characteristics. *Collagen and Related Research*, *5*(4), 355–368. https://doi.org/10.1016/S0174-173X(85)80024-8

Sherifova and, S., & Holzapfel, G. A. (2020). Biochemomechanics of the thoracic aorta in health and disease. *Progress in Biomedical Engineering*, *2*(3), 032002. https://doi.org/10.1088/2516-1091/ab9a29

Sigaeva, T., Sommer, G., Holzapfel, G. A., & Di Martino, E. S. (2019). Anisotropic residual stresses in arteries. *Journal of The Royal Society Interface*, *16*(151), 20190029. https://doi.org/10.1098/rsif.2019.0029

Sokolis, D. P. (2007). Passive mechanical properties and structure of the aorta: Segmental analysis. *Acta Physiologica*, *190*(4), 277–289. https://doi.org/10.1111/j.1748-1716.2006.01661.x

Sun, W., & Sacks, M. S. (2005). Finite element implementation of a generalized Fung-elastic constitutive model for planar soft tissues. *Biomechanics and Modelling in Mechanobiology*, *4*(2–3), 190–199. https://doi.org/10.1007/s10237-005-0075-x

Tanaka, T. T., & Fung, Y.-C. (1974). Elastic and inelastic properties of the canine aorta and their variation along the aortic tree. *Journal of Biomechanics*, *7*(4), 357–370. https://doi.org/10.1016/0021-9290(74)90031-1

Teo, E. P., & Isselbacher, E. M. (2019). Diseases of the Aorta. In *Essential Echocardiography* (pp. 354-368.e1). Elsevier. https://doi.org/10.1016/B978-0-323-39226-6.00034-5

Tonar, Z., Kubíková, T., Prior, C., Demjén, E., Liška, V., Králíčková, M., & Witter, K. (2015). Segmental and age differences in the elastin network, collagen, and smooth muscle phenotype in the tunica media of the porcine aorta. *Annals of Anatomy - Anatomischer Anzeiger*, *201*, 79–90. https://doi.org/10.1016/j.aanat.2015.05.005

Tsamis, A., Krawiec, J. T., & Vorp, D. A. (2013). Elastin and collagen fibre microstructure of the human aorta in ageing and disease: A review. *Journal of the Royal Society Interface*, *10*(83). https://doi.org/10.1098/rsif.2012.1004

UAB Medicine. (n.d.). *Aortic Aneurysm*. Retrieved April 8, 2021, from https://www.uabmedicine.org/patient-care/conditions/aneurysm

van Prehn, J., Vincken, K. L., Sprinkhuizen, S. M., Viergever, M. A., van Keulen, J. W., van Herwaarden, J. A., Moll, F. L., & Bartels, L. W. (2009). Aortic Pulsatile Distention in Young Healthy Volunteers is Asymmetric: Analysis with ECG-gated MRI. *European Journal of Vascular and Endovascular Surgery*, *37*(2), 168–174. https://doi.org/10.1016/j.ejvs.2008.11.007

Wagenseil, J. E., & Mecham, R. P. (2009). Vascular Extracellular Matrix and Arterial Mechanics. *Physiological Reviews*, *89*(3), 957–989. https://doi.org/10.1152/physrev.00041.2008

Wagenseil, J. E., & Mecham, R. P. (2012). Elastin in large artery stiffness and hypertension. *Journal of Cardiovascular Translational Research*, *5*(3), 264–273. https://doi.org/10.1007/s12265-012-9349-8

Wagenseil, J. E., Nerurkar, N. L., Knutsen, R. H., Okamoto, R. J., Li, D. Y., & Mecham, R. P. (2005). Effects of elastin haploinsufficiency on the mechanical behaviour of mouse arteries. *American Journal of Physiology-Heart and Circulatory Physiology*, *289*(3), H1209–H1217. https://doi.org/10.1152/ajpheart.00046.2005

Watanabe, M., Sawai, T., Nagura, H., & Suyama, K. (1996). Age-Related Alteration of Cross-Linking Amino Acids of Elastin in Human Aorta. *The Tohoku Journal of Experimental Medicine*, *180*(2), 115–130. https://doi.org/10.1620/tjem.180.115

Wells, R. G. (2013). Tissue mechanics and fibrosis. *Biochimica et Biophysica Acta (BBA) - Molecular Basis of Disease*, *1832*(7), 884–890. https://doi.org/10.1016/j.bbadis.2013.02.007

Wight, T. N. (1980). Vessel proteoglycans and thrombogenesis. *Progress in Hemostasis and Thrombosis*, *5*, 1–39.

Wilson, D. P. (2011). Vascular Smooth Muscle Structure and Function. In R. Fitridge & M. Thompson (Eds.), *Mechanisms of Vascular Disease: A Reference Book for Vascular Specialists*. University of Adelaide Press. http://www.ncbi.nlm.nih.gov/books/NBK534250/

Woo, S., Moon, D., & Dede, O. (2016, July 22). Basic Science of Ligaments and Tendons Related to Rehabilitation. *Musculoskeletal Key*. https://musculoskeletalkey.com/basic-science-of-ligaments-and-tendons-related-to-rehabilitation/

World Health Organization. (2017, May 17). *Cardiovascular diseases (CVDs)*. https://www.who.int/news-room/fact-sheets/detail/cardiovascular-diseases-(cvds)

Xu, J., & Shi, G.-P. (2014). Vascular wall extracellular matrix proteins and vascular diseases. *Biochimica et Biophysica Acta (BBA) - Molecular Basis of Disease*, *1842*(11), 2106–2119. https://doi.org/10.1016/j.bbadis.2014.07.008

Yu, X., Wang, Y., & Zhang, Y. (2018). Transmural variation in elastin fiber orientation distribution in the arterial wall. *Journal of the Mechanical Behaviour of Biomedical Materials*, *77*, 745–753. https://doi.org/10.1016/j.jmbbm.2017.08.002

Appendix A: Supplementary Calculations and Derivations

A.1 Specific Strain Energy Functions

A.1.1 Fung Model: Calculation of the tangent modulus

In general, $\frac{\partial^2 W}{\partial E_\alpha^2} = \frac{c_1}{2}\exp(\boldsymbol{Q})\left(\frac{\partial^2 Q}{\partial E_\alpha^2} + \left(\frac{\partial Q}{\partial E_\alpha^2}\right)^2\right)$

Calculation of second partial derivative with respect to E_{11}:

$$\frac{\partial Q}{\partial E_{11}} = 2c_2E_{11} + 2c_4E_{22} + 2c_6E_{12}$$

$$\frac{\partial^2 Q}{\partial E_{11}^2} = 2c_2$$

$$\frac{\partial^2 W}{\partial E_{11}^2} = \frac{c_1}{2}\exp(Q)\,[2c_2 + (2c_2E_{11} + 2c_4E_{22} + 2c_6E_{12})^2]$$

Calculation of second partial derivative with respect to E_{22}:

$$\frac{\partial Q}{\partial E_{22}} = 2c_3E_{22} + 2c_4E_{11} + 2c_7E_{12}$$

$$\frac{\partial^2 Q}{\partial E_{22}^2} = 2c_3$$

$$\frac{\partial^2 W}{\partial E_{22}^2} = \frac{c_1}{2}\exp(Q)\,[2c_3 + (2c_3E_{22} + 2c_4E_{11} + 2c_7E_{12})^2]$$

Calculation of second partial derivative with respect to E_{12}:

$$\frac{\partial Q}{\partial E_{12}} = 2c_5E_{12} + 2c_6E_{11} + 2c_7E_{22}$$

$$\frac{\partial^2 Q}{\partial E_{12}^2} = 2c_5$$

$$\frac{\partial^2 W}{\partial E_{12}^2} = \frac{c_1}{2}\exp(Q)\,[2c_5 + (2c_5E_{12} + 2c_6E_{11} + 2c_7E_{22})^2]$$

Calculation of second partial derivative with respect to E_α and E_β:

In general, $\frac{\partial^2 W}{\partial E_\alpha \partial E_\beta} = \frac{c_1}{2}\exp(Q)\left(\frac{\partial^2 Q}{\partial E_\alpha \partial E_\beta} + \left(\frac{\partial Q}{\partial E_\alpha}\right)\left(\frac{\partial Q}{\partial E_\beta}\right)\right)$

Calculation of second partial derivative with respect to E_{11} and E_{12}:

$$\frac{\partial Q}{\partial E_{11}} = 2c_2E_{11} + 2c_4E_{22} + 2c_6E_{12}$$

$$\frac{\partial Q}{\partial E_{12}} = 2c_5E_{12} + 2c_6E_{11} + 2c_7E_{22}$$

$$\frac{\partial^2 Q}{\partial E_{11}\partial E_{12}} = 2c_7$$

$$\frac{\partial^2 W}{\partial E_{11}\partial E_{12}} = \frac{c_1}{2}\exp(Q)\left[2c_6 + (2c_2E_{11} + 2c_4E_{22} + 2c_6E_{12})(2c_5E_{12} + 2c_6E_{11} + 2c_7E_{22})\right]$$

Calculation of second partial derivative with respect to E_{22} and E_{12}:

$$\frac{\partial Q}{\partial E_{22}} = 2c_3E_{22} + 2c_4E_{11} + 2c_7E_{12}$$

$$\frac{\partial Q}{\partial E_{12}} = 2c_5E_{12} + 2c_6E_{11} + 2c_7E_{22}$$

$$\frac{\partial^2 Q}{\partial E_{22}\partial E_{12}} = 2c_7$$

$$\frac{\partial^2 W}{\partial E_{22}\partial E_{12}} = \frac{c_1}{2}\exp(Q)\left[2c_7 + (2c_3E_{22} + 2c_4E_{11} + 2c_7E_{12})(2c_5E_{12} + 2c_6E_{11} + 2c_7E_{22})\right]$$

Calculation of second partial derivative with respect to E_{11} and E_{22}:

$$\frac{\partial Q}{\partial E_{11}} = 2c_2E_{11} + 2c_4E_{22} + 2c_6E_{12}$$

$$\frac{\partial Q}{\partial E_{22}^2} = 2c_5E_{12} + 2c_6E_{11} + 2c_7E_{22}$$

$$\frac{\partial^2 Q}{\partial E_{11}\partial E_{22}} = 2c_4$$

$$\frac{\partial^2 W}{\partial E_{11}\partial E_{22}} = \frac{c_1}{2}\exp(Q)\,[2c_4 + (2c_2E_{11} + 2c_4E_{22} + 2c_6E_{12})(2c_3E_{22} + 2c_4E_{11} + 2c_7E_{12})]$$

A.1.2 Guccione Model: Calculation of the tangent modulus

In general, $\frac{\partial^2 W}{\partial E_\alpha^2} = \frac{c_1}{2}\exp(Q)\left(\frac{\partial^2 Q}{\partial E_\alpha^2} + \left(\frac{\partial Q}{\partial E_\alpha^2}\right)^2\right)$

Calculation of second partial derivative with respect to E_{11}:

$$\frac{\partial Q}{\partial E_{11}} = 2c_2E_{11} - \frac{c_3}{\Delta(2E_{11}+1)}\left(\frac{1}{\Delta} - 1\right)$$

$$\frac{\partial^2 Q}{\partial E_{11}^2} = 2c_2 + \frac{c_3}{(2E_{11}+1)^2}\left(\frac{6}{\Delta^2} - \frac{4}{\Delta}\right)$$

$$\frac{\partial^2 W}{\partial E_{11}^2} = \frac{c_1}{2}\exp(Q)\left[2c_2 + \frac{c_3}{(2E_{11}+1)^2}\left(\frac{6}{\Delta^2} - \frac{4}{\Delta}\right) + \left(2c_2E_{11} - \frac{c_3}{\Delta(2E_{11}+1)}\left(\frac{1}{\Delta} - 1\right)\right)^2\right]$$

Calculation of second partial derivative with respect to E_{22}:

$$\frac{\partial Q}{\partial E_{22}} = 2c_3E_{22} - \frac{c_3}{\Delta(2E_{22}+1)}\left(\frac{1}{\Delta} - 1\right)$$

$$\frac{\partial^2 Q}{\partial E_{22}^2} = 2c_3 + \frac{c_3}{(2E_{22}+1)^2}\left(\frac{6}{\Delta^2} - \frac{4}{\Delta}\right)$$

$$\frac{\partial^2 W}{\partial E_{22}^2} = \frac{c_1}{2}\exp(Q)\left[2c_3 + \frac{c_3}{(2E_{22}+1)^2}\left(\frac{6}{\Delta^2} - \frac{4}{\Delta}\right) + \left(2c_3E_{22} - \frac{c_3}{\Delta(2E_{22}+1)}\left(\frac{1}{\Delta} - 1\right)\right)^2\right]$$

Calculation of second partial derivative with respect to E_{12}:

$$\frac{\partial Q}{\partial E_{12}} = 2c_4E_{12}$$

$$\frac{\partial^2 Q}{\partial E_{12}^2} = 2c_4$$

$$\frac{\partial^2 W}{\partial E_{12}^2} = \frac{c_1}{2}\exp(Q)\,[2c_4 + (2c_4E_{12})^2]$$

Calculation of second partial derivative with respect to E_α and E_β:

In general, $\frac{\partial^2 W}{\partial E_\alpha \partial E_\beta} = \frac{c_1}{2}\exp(Q)\left(\frac{\partial^2 Q}{\partial E_\alpha \partial E_\beta} + \left(\frac{\partial Q}{\partial E_\alpha}\right)\left(\frac{\partial Q}{\partial E_\beta}\right)\right)$

Calculation of second partial derivative with respect to E_{11} and E_{12}:

$$\frac{\partial Q}{\partial E_{11}} = 2c_2E_{11} - \frac{c_3}{\Delta(2E_{22}+1)}\left(\frac{1}{\Delta} - 1\right)$$

$$\frac{\partial Q}{\partial E_{12}} = 2c_4E_{12}$$

$$\frac{\partial^2 Q}{\partial E_{11}\partial E_{12}} = 0$$

$$\frac{\partial^2 W}{\partial E_{11}\partial E_{12}} = \frac{c_1}{2}\exp(Q)\left(2c_2E_{11} - \frac{c_3}{\Delta(2E_{11}+1)}\left(\frac{1}{\Delta} - 1\right)\right)2c_4E_{12}$$

Calculation of second partial derivative with respect to E_{22} and E_{12}:

$$\frac{\partial Q}{\partial E_{22}} = 2c_3E_{22} - \frac{c_3}{\Delta(2E_{22}+1)}\left(\frac{1}{\Delta} - 1\right)$$

$$\frac{\partial Q}{\partial E_{12}} = 2c_4E_{12}$$

$$\frac{\partial^2 Q}{\partial E_{22}\partial E_{12}} = 0$$

$$\frac{\partial^2 W}{\partial E_{22}\partial E_{12}} = \frac{c_1}{2}\exp(Q)\left(2c_3E_{22} - \frac{c_3}{\Delta(2E_{22}+1)}\left(\frac{1}{\Delta} - 1\right)\right)2c_4E_{12}$$

Calculation of second partial derivative with respect to E_{11} and E_{22}:

$$\frac{\partial Q}{\partial E_{11}} = 2c_2E_{11-} \frac{c_3}{\Delta(2E_{11}+1)}\left(\frac{1}{\Delta} - 1\right)$$

$$\frac{\partial Q}{\partial E_{22}^2} = 2c_3E_{22} - \frac{c_3}{\Delta(2E_{22}+1)}\left(\frac{1}{\Delta} - 1\right)$$

$$\frac{\partial^2 Q}{\partial E_{11}\partial E_{22}} = c_3\left(\frac{4}{\Delta^3} - \frac{2}{\Delta^2}\right)$$

$$\frac{\partial^2 W}{\partial E_{11}\partial E_{22}} = \frac{c_1}{2}\exp(Q)\left(c_3\left(\frac{4}{\Delta^3}-\frac{2}{\Delta^2}\right)\right.$$

$$\left.+\left(2c_2E_{11}-\frac{c_3}{\Delta(2E_{11}+1)}\left(\frac{1}{\Delta}-1\right)\right)\left(2c_3E_{22}-\frac{c_3}{\Delta(2E_{22}+1)}\left(\frac{1}{\Delta}-1\right)\right)\right)$$

Appendix B: Supplementary Results

B.1 Experiment 1

Table 16 – Average strain and stiffness values at 60 and 120 N/m using the Fung strain energy function for the anterior, posterior, left and right lateral sides of Asc., Arc., Tho.

Average Material Property	Ascending Aorta				Aortic Arch				Thoracic Descending			
	A	R	P	L	A	R	P	L	A	R	P	L
E_FD@60N/m [-]	0.17 ± 0.03	0.17 ± 0.02	0.17 ± 0.04	0.17 ± 0.02	0.17 ± 0.03	0.17 ± 0.03	0.16 ± 0.04	0.16 ± 0.02	0.18 ± 0.02	0.17 ± 0.02	0.19 ± 0.04	0.19 ± 0.04
E_XD [-]	0.18 ± 0.05	0.16 ± 0.04	0.16 ± 0.03	0.15 ± 0.02	0.14 ± 0.02	0.14 ± 0.03	0.14 ± 0.03	0.14 ± 0.03	0.16 ± 0.02	0.15 ± 0.02	0.15 ± 0.02	0.14 ± 0.03
S_FD [N/m]	381.00 ± 34.50	391.88 ± 41.66	399.00 ± 15.97	374.33 ± 16.00	420.67 ± 31.32	406.67 ± 46.99	412.78 ± 53.85	409.44 ± 23.35	404.00 ± 46.11	416.22 ± 25.67	398.00 ± 42.85	400.56 ± 21.53
S_XD [N/m]	382.89 ± 86.58	427.88 ± 70.91	413.44 ± 59.80	422.44 ± 49.83	475.44 ± 60.28	457.56 ± 55.18	455.44 ± 48.20	452.00 ± 62.16	449.22 ± 74.66	458.44 ± 73.34	466.33 ± 72.82	482.44 ± 105.79
E_FD@120N/m [-]	0.27 ± 0.03	0.26 ± 0.03	0.26 ± 0.06	0.27 ± 0.03	0.25 ± 0.03	0.26 ± 0.04	0.26 ± 0.06	0.25 ± 0.03	0.26 ± 0.03	0.25 ± 0.02	0.28 ± 0.05	0.27 ± 0.04
E_XD [-]	0.28 ± 0.08	0.24 ± 0.06	0.24 ± 0.05	0.23 ± 0.03	0.2 ± 0.03	0.22 ± 0.04	0.22 ± 0.04	0.22 ± 0.04	0.23 ± 0.03	0.24 ± 0.06	0.22 ± 0.04	0.21 ± 0.04
S_FD [N/m]	609.11 ± 41.54	632.88 ± 79.15	638.56 ± 130.11	597.33 ± 49.91	696.56 ± 59.81	667.33 ± 39.94	662.56 ± 69.05	666.44 ± 55.81	703.33 ± 26.52	713.00 ± 26.70	698.22 ± 26.42	691.44 ± 26.30
S_XD [N/m]	610.00 ± 100.40	676.88 ± 91.31	658.56 ± 129.25	658.67 ± 67.26	770.44 ± 114.29	735.56 ± 83.16	718.56 ± 110.92	721.78 ± 106.02	763.11 ± 146.82	771.89 ± 143.14	794.67 ± 20.05	808.44 ± 203.67

E_FD@: Green strain in the fiber direction under 60 and 120 N/m 2nd PK membrane tension, respectively. E_XD@: Green strain in the cross-fiber direction under 60 and 120 N/m 2nd PK membrane tension, respectively.S stands for stiffness, as defined in text.

Table 17 – Average strain and stiffness values at 60 and 120 N/m using the Guccione strain energy function for the anterior, posterior, left, right lateral sides of Asc., Arc., Tho.

Average Material Property	Ascending Aorta				Aortic Arch				Thoracic Descending			
	A	R	P	L	A	R	P	L	A	R	P	L
E_FD@60N/m [-]	0.18 ± 0.03	0.17 ± 0.02	0.17 ± 0.05	0.18 ± 0.02	0.17 ± 0.04	0.17 ± 0.04	0.16 ± 0.05	0.16 ± 0.03	0.17 ± 0.04	0.18 ± 0.04	0.20 ± 0.05	0.20 ± 0.06
E_XD [-]	0.19 ± 0.06	0.16 ± 0.05	0.16 ± 0.04	0.15 ± 0.02	0.14 ± 0.03	0.14 ± 0.03	0.14 ± 0.03	0.14 ± 0.03	0.15 ± 0.02	0.15 ± 0.03	0.15 ± 0.03	0.14 ± 0.04
S_FD [N/m]	330.67 ± 21.41	339.63 ± 34.12	336.33 ± 15.97	322.44 ± 16.00	357.33 ± 24.26	351.67 ± 34.20	363.78 ± 45.72	355.89 ± 19.08	345.89 ± 25.61	357.89 ± 16.13	348.33 ± 33.06	344.00 ± 14.34
S_XD [N/m]	328.00 ± 61.17	362.00 ± 48.44	344.00 ± 37.77	355.89 ± 33.93	392.00 ± 36.47	384.78 ± 43.31	387.00 ± 34.37	384.78 ± 42.65	374.56 ± 43.97	385.11 ± 43.76	393.56 ± 45.70	398.67 ± 53.74
E_FD@120N/m [-]	0.27 ± 0.03	0.26 ± 0.03	0.26 ± 0.06	0.27 ± 0.03	0.25 ± 0.04	0.26 ± 0.04	0.25 ± 0.06	0.25 ± 0.03	0.27 ± 0.03	0.26 ± 0.03	0.28 ± 0.06	0.27 ± 0.07
E_XD [-]	0.28 ± 0.08	0.24 ± 0.07	0.24 ± 0.05	0.23 ± 0.03	0.21 ± 0.04	0.22 ± 0.04	0.21 ± 0.04	0.22 ± 0.04	0.23 ± 0.03	0.22 ± 0.04	0.21 ± 0.04	0.21 ± 0.05
S_FD [N/m]	626.11 ± 38.33	639.00 ± 59.05	624.56 ± 65.37	618.22 ± 41.63	687.33 ± 36.29	640.78 ± 99.48	685.33 ± 52.15	678.78 ± 33.56	680.78 ± 26.09	702.56 ± 26.51	694.89 ± 26.36	691.44 ± 26.07
S_XD [N/m]	621.22 ± 90.99	670.38 ± 75.12	637.33 ± 66.32	667.44 ± 54.80	740.00 ± 68.57	691.11 ± 132.27	721.56 ± 69.17	722.00 ± 77.20	725.33 ± 89.11	744.56 ± 86.63	766.78 ± 20.05	808.44 ± 107.5

B.2 Experiment 2

Table 18 – Average strain and stiffness values at 60 and 120 N/m using the Fung strain energy function at various incubation times.

Material Properties (Fung)	Incubation Time [hours]								
	ASC			ARC			THO		
	0	4	48	0	4	48	0	4	48
E_FD@60N/m [-]	0.17 ± 0.047	0.18 ± 0.037	0.16 ± 0.029	0.19 ± 0.030	0.15 ± 0.055	0.17 ± 0.045	0.19 ± 0.028	0.17 ± 0.021	0.17 ± 0.043
E_XD [-]	0.13 ± 0.029	0.15 ± 0.023	0.14 ± 0.048	0.12 ± 0.026	0.14 ± 0.035	0.13 ± 0.033	0.14 ± 0.024	0.14 ± 0.015	0.14 ± 0.047
S_FD [N/m]	376.63 ± 75.80	371.88 ± 52.01	388.71 ± 45.60	379.57 ± 45.70	455.75 ± 99.58	435.57 ± 60.56	408.75 ± 35.99	431.50 ± 35.50	426.43 ± 68.15
S_XD [N/m]	436.13 ± 62.58	410.50 ± 30.13	431.57 ± 71.77	527.29 ± 91.09	466.13 ± 52.23	514.00 ± 104.64	488.50 ± 66.21	497.13 ± 27.30	500.29 ± 113.49
E_FD @120N/m [-]	0.27 ± 0.071	0.27 ± 0.054	0.26 ± 0.034	0.29 ± 0.043	0.23 ± 0.068	0.24 ± 0.039	0.27 ± 0.032	0.25 ± 0.028	0.25 ± 0.053
E_XD [-]	0.21 ± 0.044	0.23 ± 0.031	0.22 ± 0.063	0.18 ± 0.040	0.21 ± 0.034	0.19 ± 0.045	0.21 ± 0.029	0.20 ± 0.019	0.20 ± 0.060
S_FD [N/m]	572.25 ± 94.85	593.75 ± 79.81	597.14 ± 44.80	654.29 ± 66.60	698.50 ± 81.65	699.86 ± 88.41	721.63 ± 63.58	769.38 ± 54.71	697.57 ± 38.78
S_XD [N/m]	647.13 ± 85.21	643.63 ± 58.19	649.14 ± 65.66	852.14 ± 128.18	716.88 ± 71.40	795.43 ± 54.35	831.88 ± 105.20	860.13 ± 37.38	793.86 ± 114.67

Table 19 – Average strain and stiffness values at 60 and 120 N/m using the Guccione strain energy function at various incubation times.

Material Properties (Guccione)	Incubation Time [hours]								
	ASC			ARC			THO		
	0	4	48	0	4	48	0	4	48
E_FD@60N/m [-]	0.17 ± 0.051	0.18 ± 0.042	0.16 ± 0.030	0.20 ± 0.036	0.15 ± 0.058	0.17 ± 0.049	0.19 ± 0.029	0.18 ± 0.024	0.17 ± 0.046
E_XD [-]	0.13 ± 0.031	0.15 ± 0.025	0.15 ± 0.050	0.12 ± 0.030	0.14 ± 0.033	0.13 ± 0.036	0.14 ± 0.024	0.14 ± 0.014	0.13 ± 0.048
S_FD [N/m]	330.25 ± 77	327.75 ± 41	340.29 ± 38	323.71 ± 38	396.75 ± 91	377.29 ± 46	351.25 ± 27	370.25 ± 23	373.57 ± 54
S_XD [N/m]	366.50 ± 47	353.88 ± 21	371.14 ± 62	417.29 ± 48	400.63 ± 49	432.00 ± 82	407.75 ± 34	418.13 ± 24.44	425.86 ± 85
E_FD@120 N/m [-]	0.27 ± 0.074	0.27 ± 0.056	0.26 ± 0.032	0.30 ± 0.047	0.23 ± 0.070	0.24 ± 0.040	0.28 ± 0.034	0.26 ± 0.029	0.25 ± 0.055
E_XD [-]	0.21 ± 0.047	0.23 ± 0.033	0.23 ± 0.064	0.18 ± 0.043	0.21 ± 0.031	0.19 ± 0.043	0.20 ± 0.029	0.20 ± 0.020	0.20 ± 0.061
S_FD [N/m]	612.88 ± 107	626.38 ± 62	627.86 ± 31	641.71 ± 68	708.75 ± 71	702.57 ± 61	702.25 ± 42	737.00 ± 38	703.57 ± 35
S_XD [N/m]	667.00 ± 76	665.75 ± 46	670.71 ± 69	782.14 ± 85	719.00 ± 37	777.71 ± 44	789.50 ± 53	811.00 ± 47	779.29 ± 92

Appendix C: Stress-Strain Curves

C.1 Experiment 1: Experimental and model-fit membrane tensions vs. strains

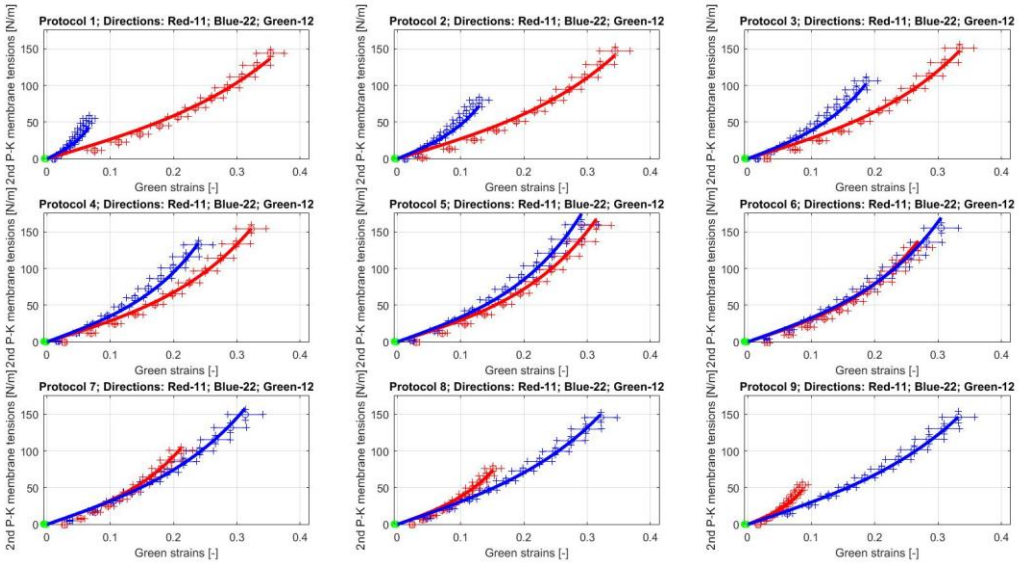

Figure 25 – Experimental data and model fit with Fung model for Asc.

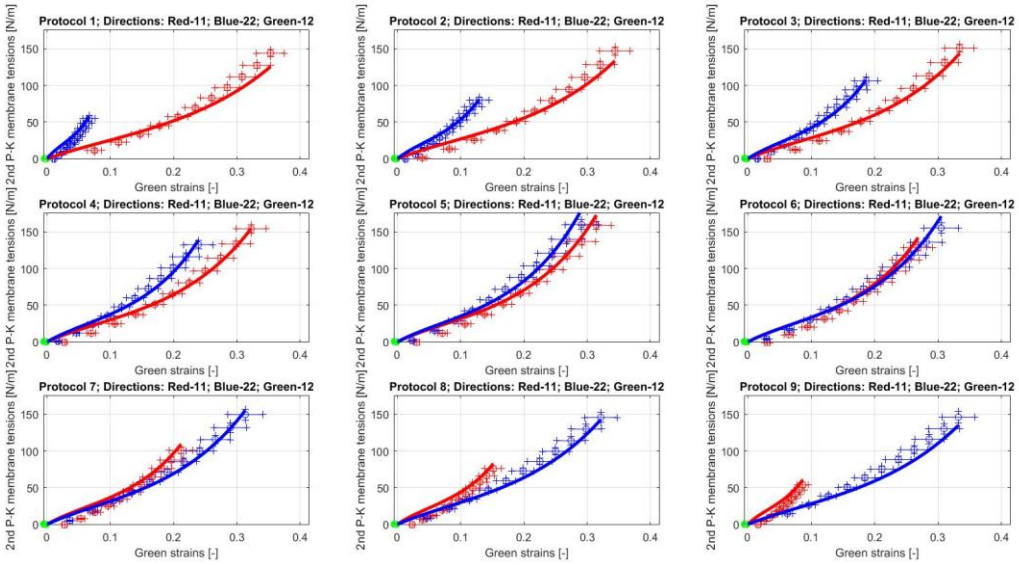

Figure 26 – Experimental data and model fit with Guccione model for Asc.

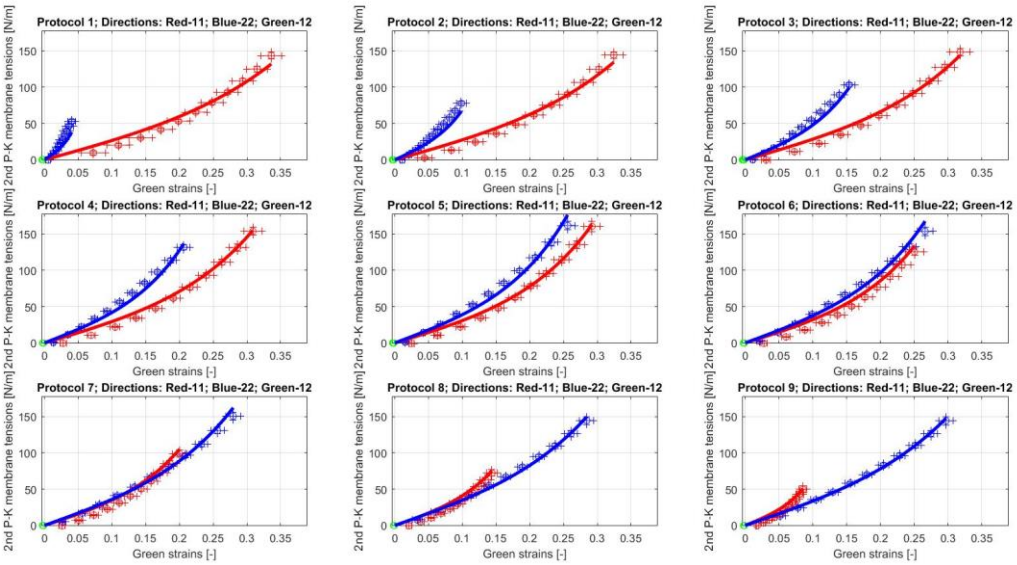

Figure 27 –Experimental data and model fit with Fung model for Arc.

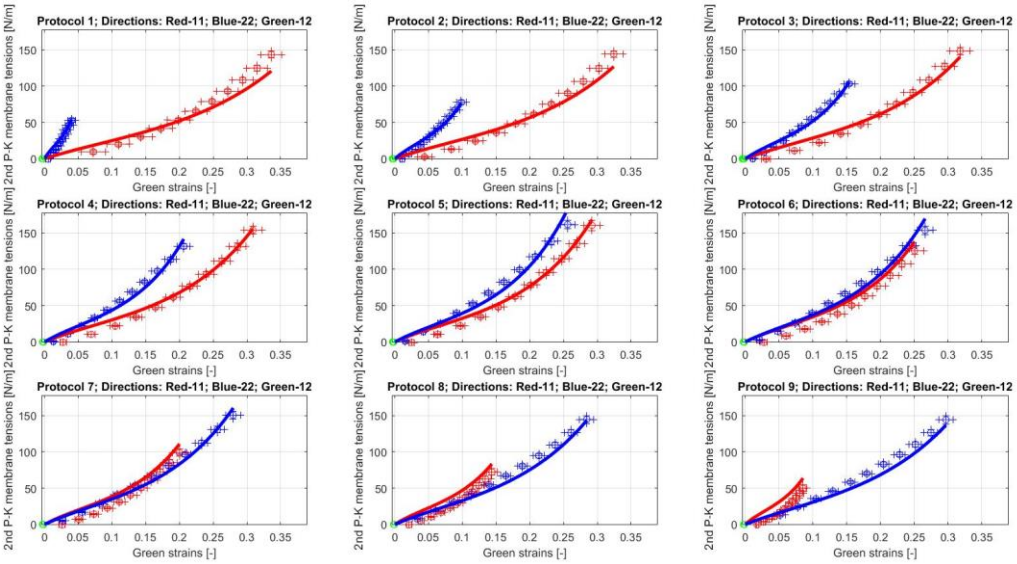

Figure 28 – Experimental data and model fit with Guccione model for Arc.

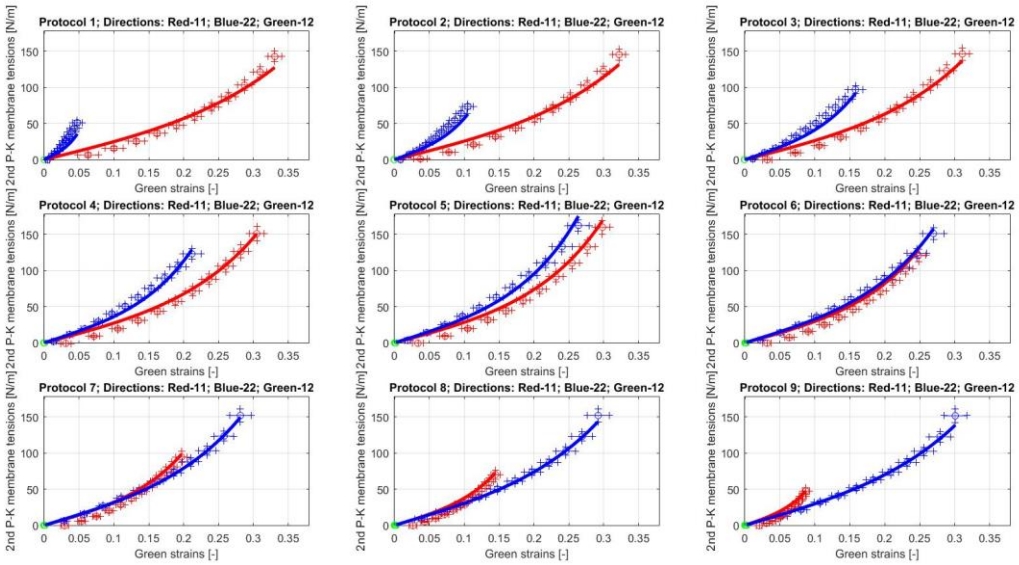

Figure 29 – Experimental data and model fit with Fung model for Tho.

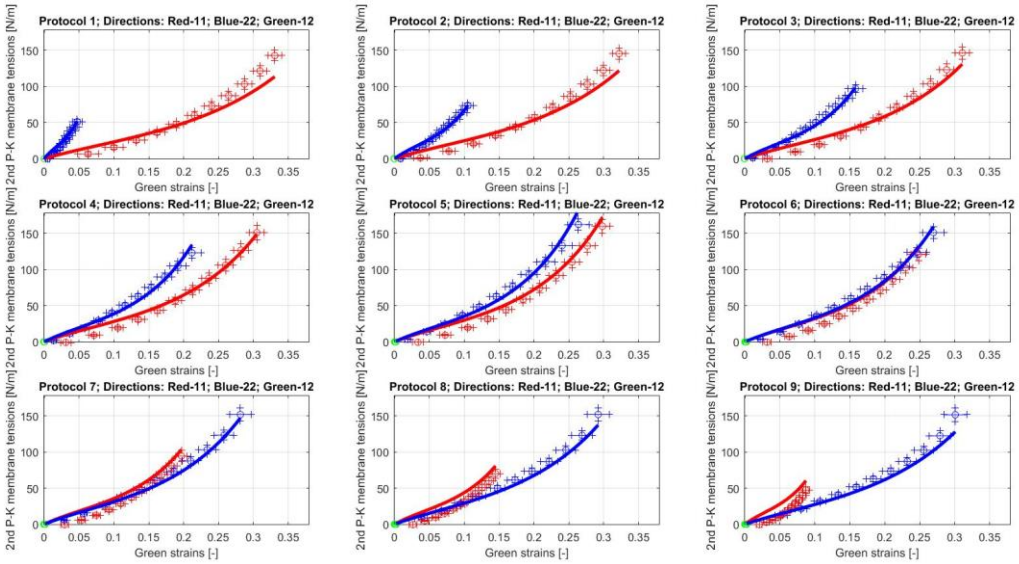

Figure 30 – Experimental data and model fit with Guccione model for Tho.

C.2 Experiment 2: Experimental and model-fit membrane tensions vs. strains

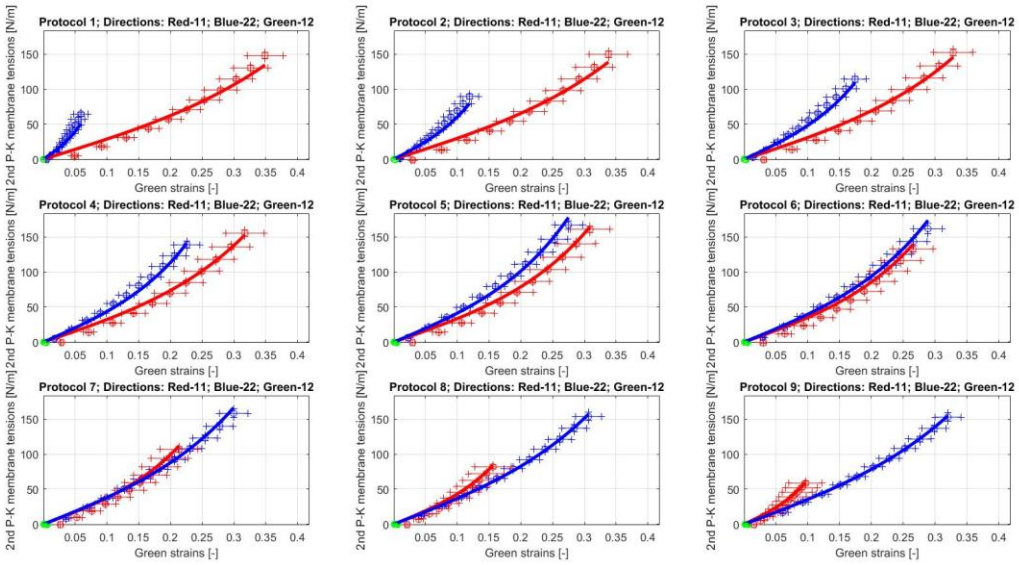

Figure 31 – Experimental data and model fit with Fung model for Asc.(untreated).

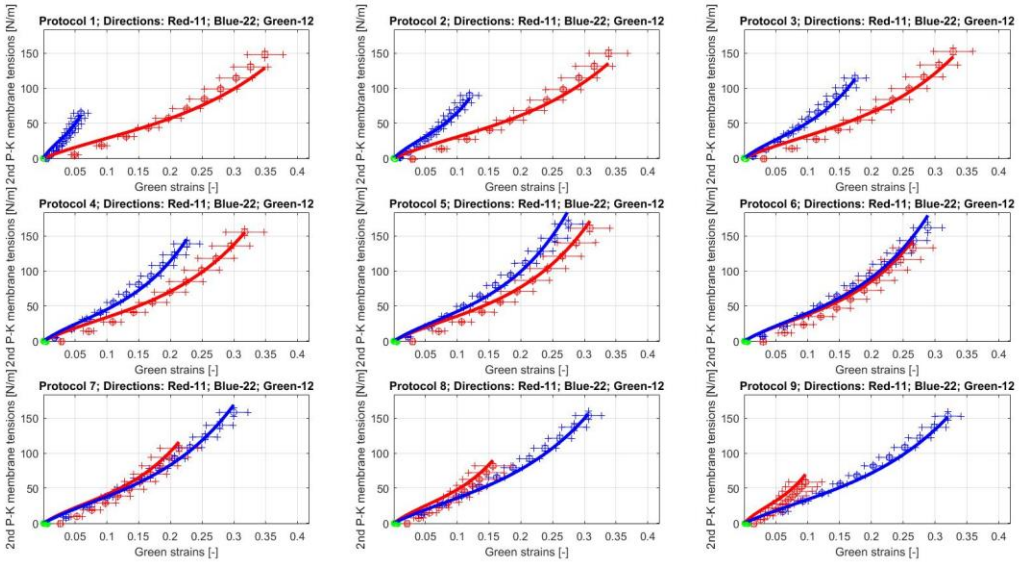

Figure 32 – Experimental data and model fit with Guccione model for Asc. (untreated).

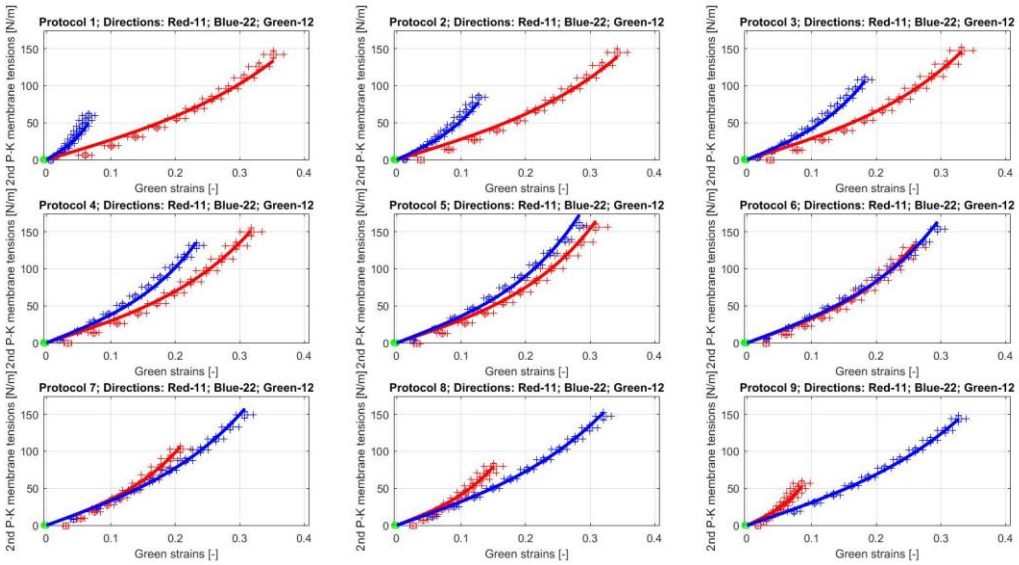

Figure 33 – Experimental data and model fit with Fung for Asc. at 4-hours incubation

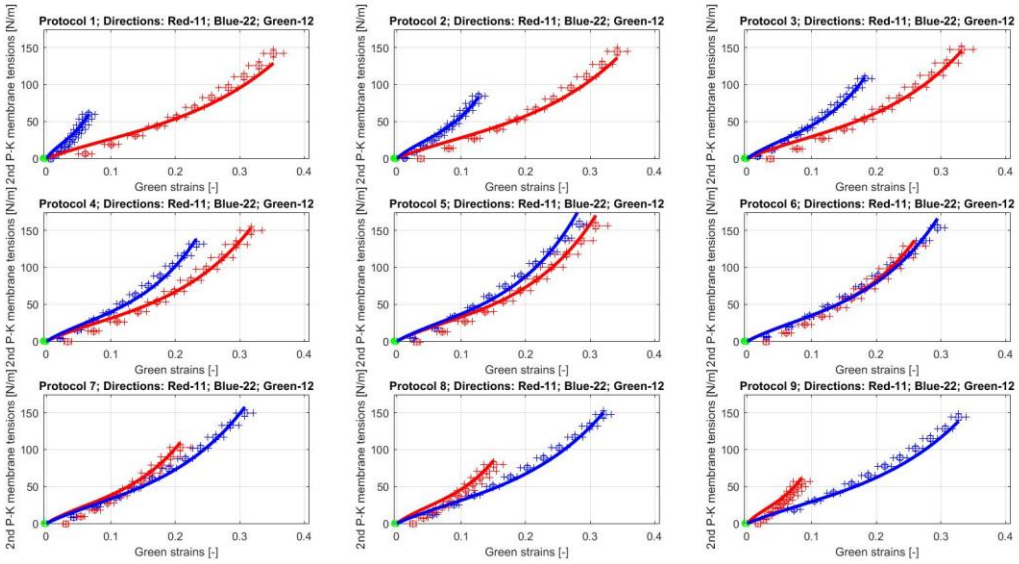

Figure 34 – Experimental data and model fit with Guccione for Asc. at 4-hours incubation.

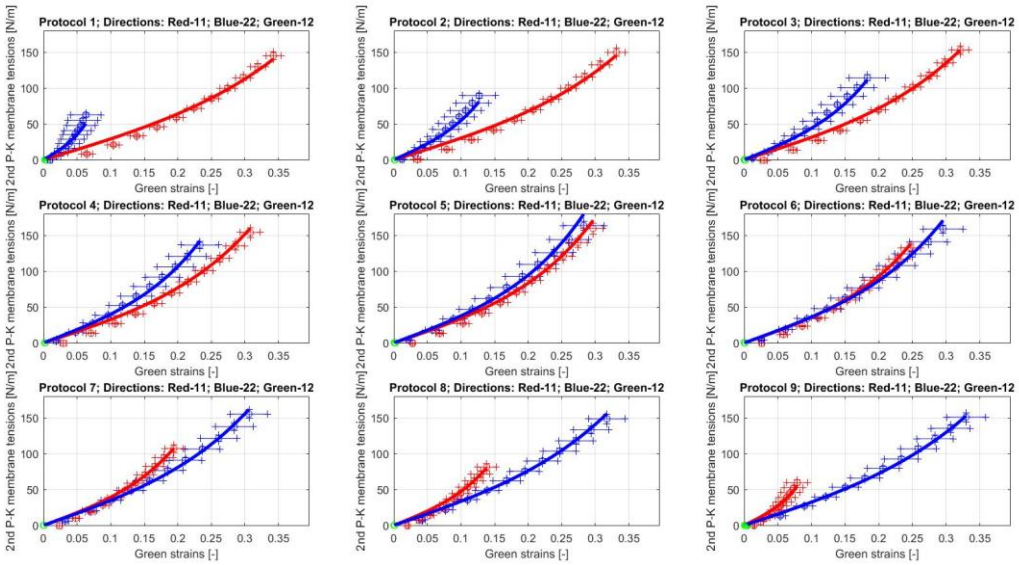

Figure 35 – Experimental data and model fit with Fung for Asc. at 48-hours incubation.

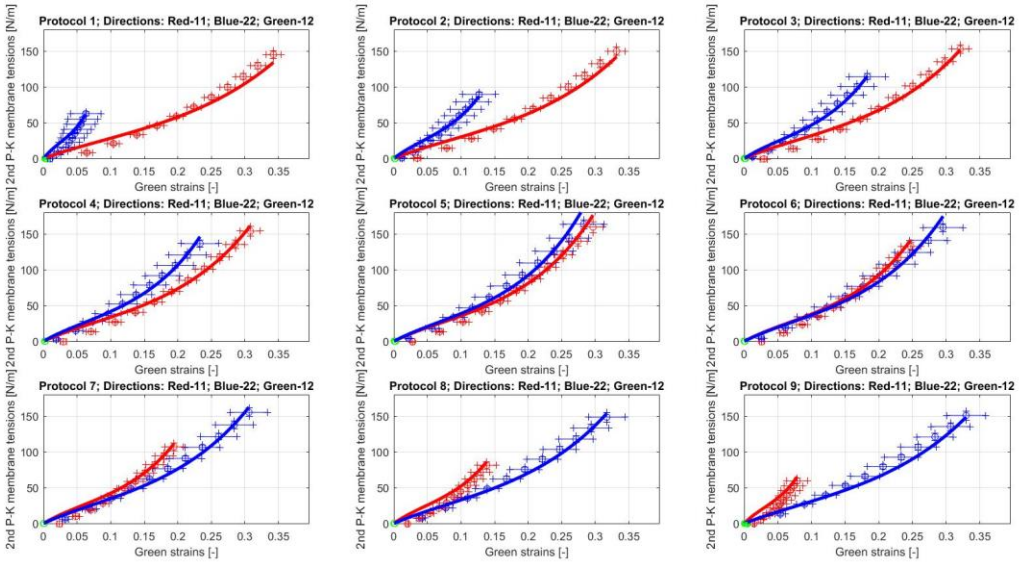

Figure 36 – Experimental data and model fit with Guccione for Asc. at 48-hours incubation.

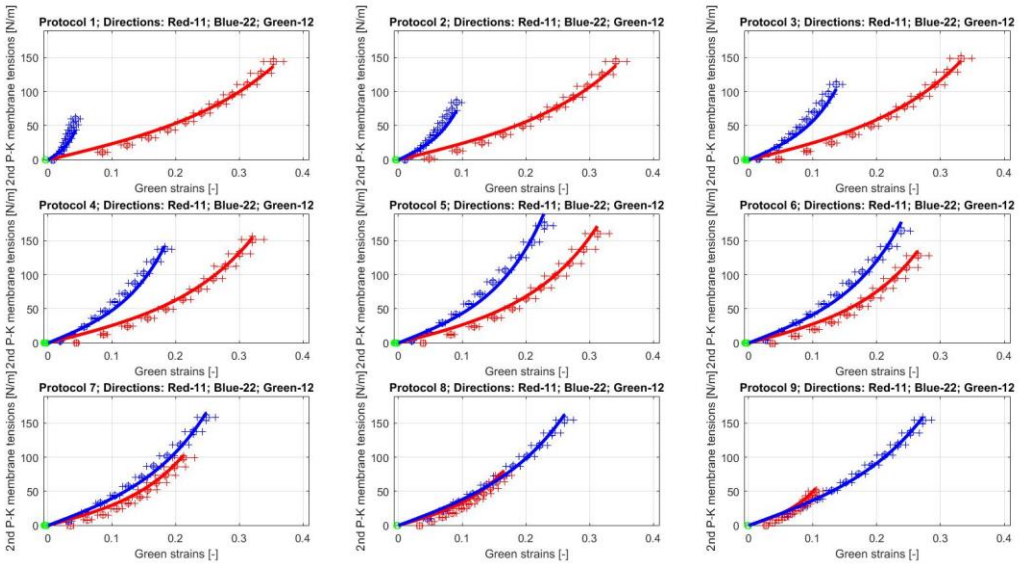

Figure 37 – Experimental data and model fit with Fung for Arc. (untreated).

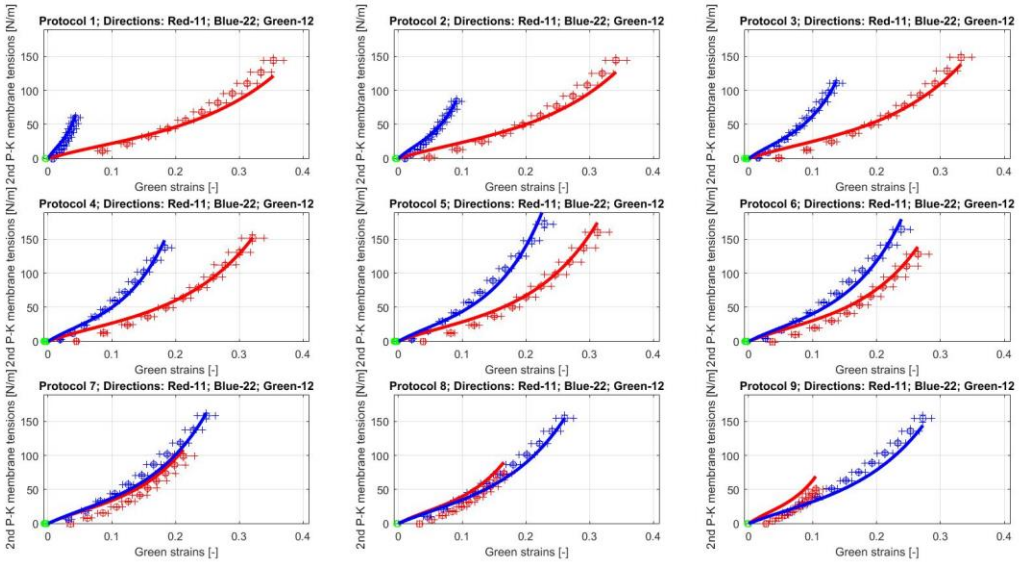

Figure 38 – Experimental data and model fit with Guccione for Arc. (untreated).

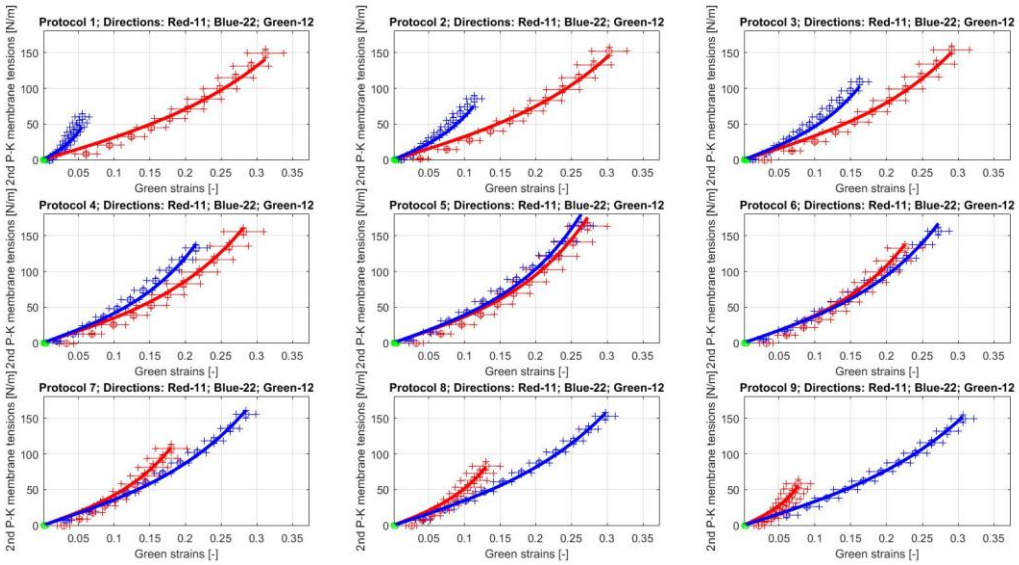

Figure 39 – Experimental data and model fit with Fung for Arc. at 4-hours incubation.

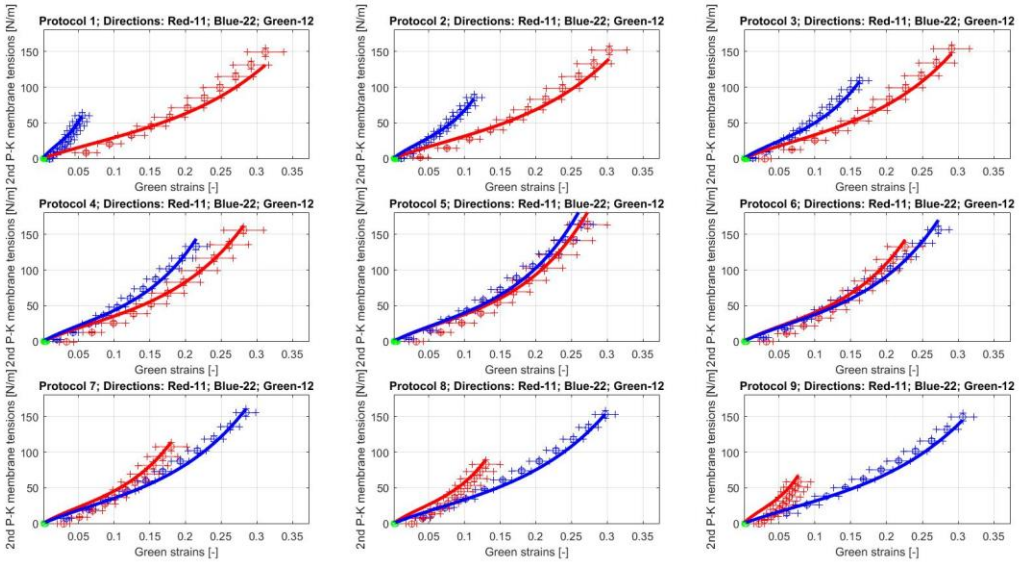

Figure 40 – Experimental data and model fit with Guccione for Arc. at 4-hours incubation.

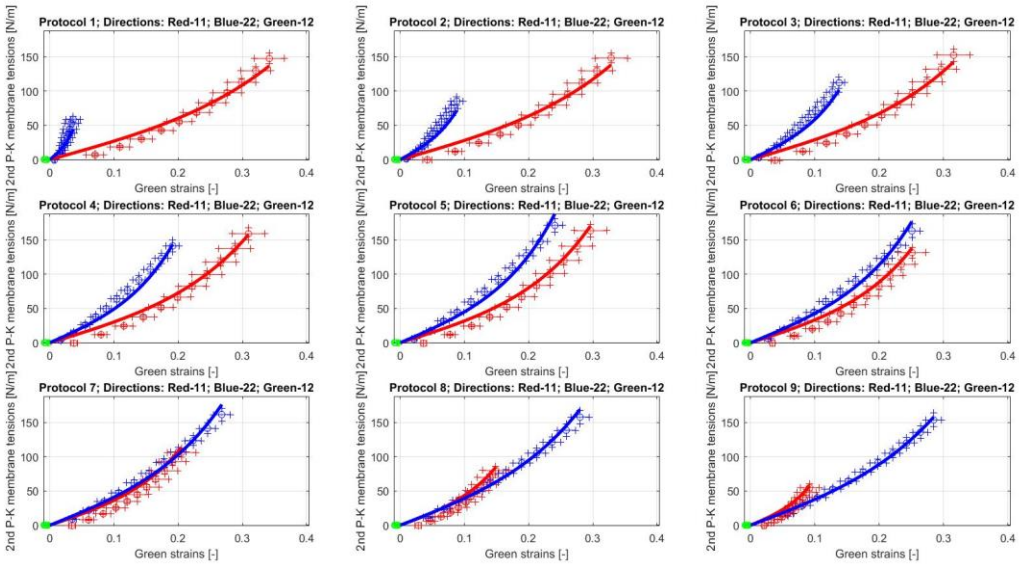

Figure 41 – Experimental data and model fit with Fung for Arc. at 48-hours incubation.

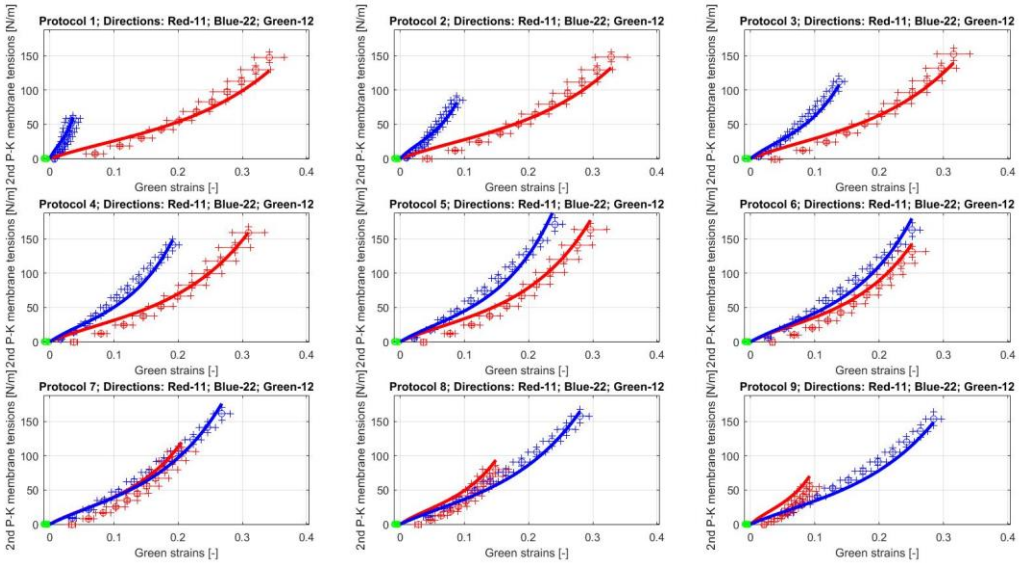

Figure 42 – Experimental data and model fit with Guccione for Arc. at 48-hours incubation.

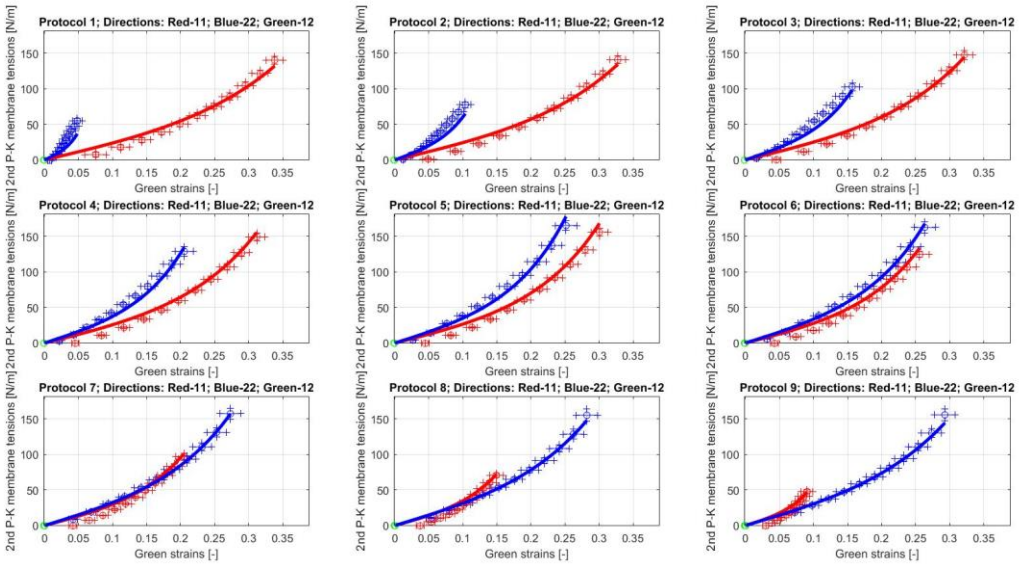

Figure 43 – Experimental data and model fit with Fung for Tho. (untreated).

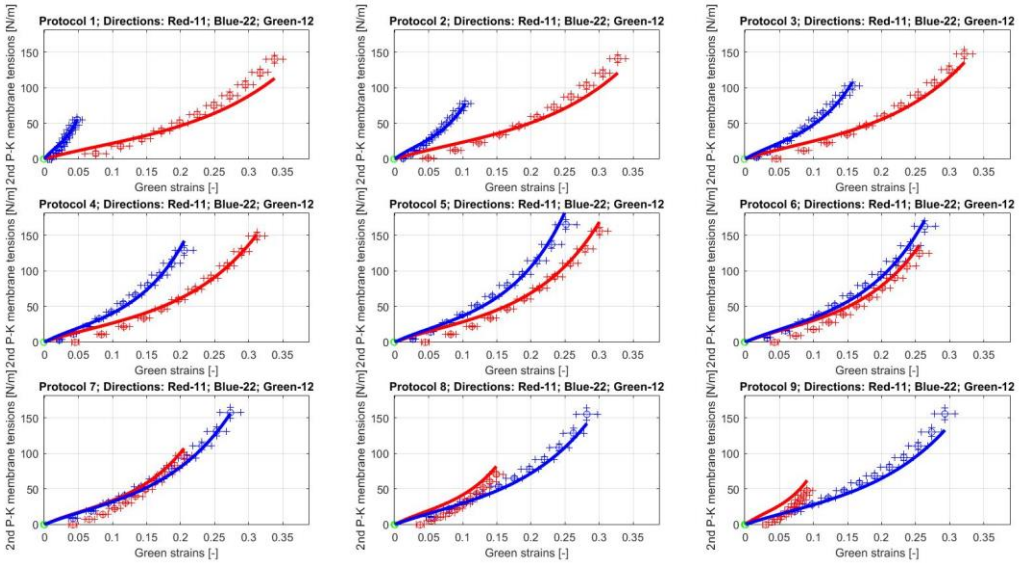

Figure 44 – Experimental data and model fit with Guccione for Tho. (untreated).

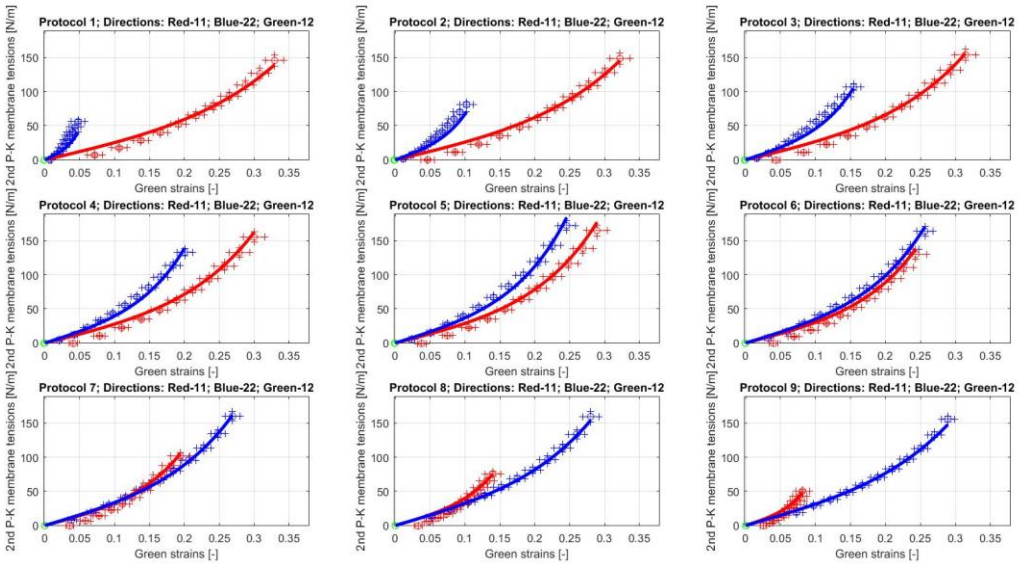

Figure 45 – Experimental data and model fit with Fung for Tho. at 4-hours incubation.

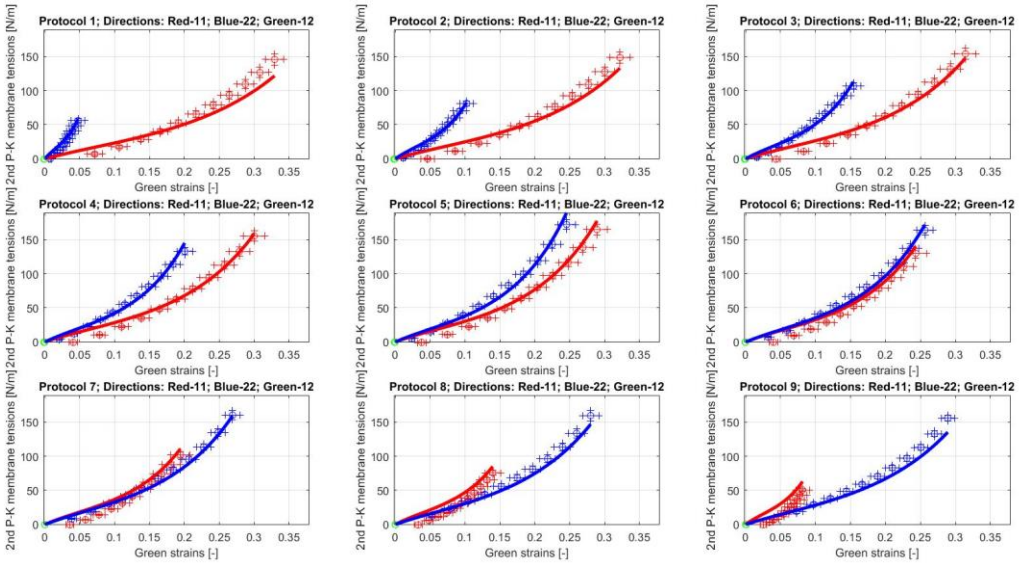

Figure 46 – Experimental data and model fit with Guccione for Tho. at 4-hours incubation.

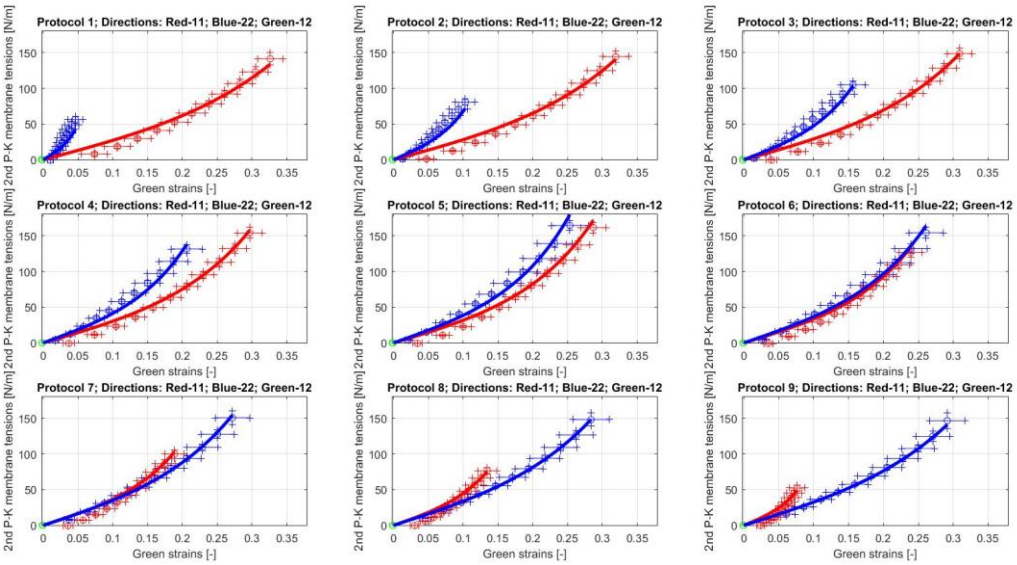

Figure 47 – Experimental data and model fit with Fung for Tho. at 48-hours incubation.

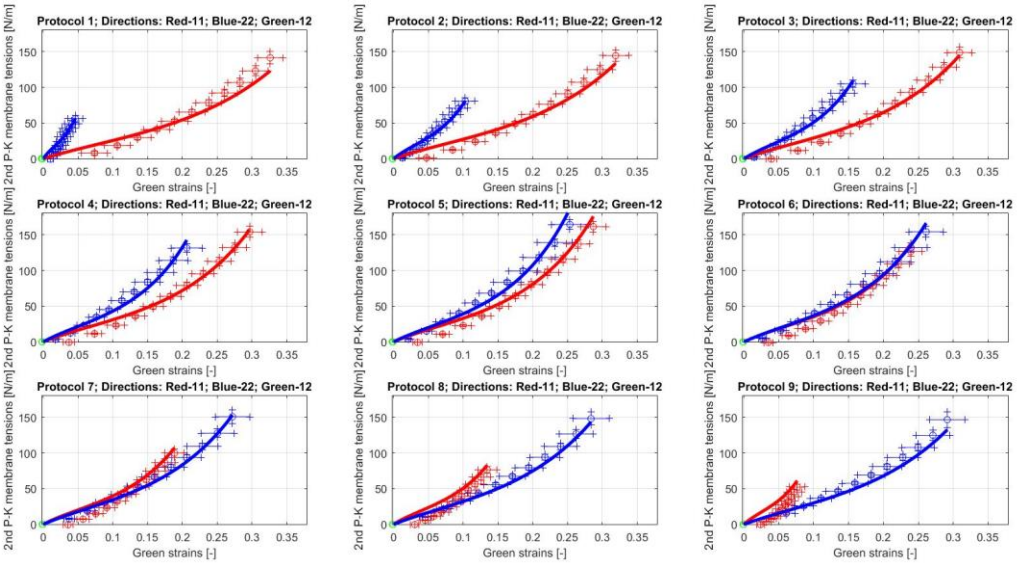

Figure 48 – Experimental data and model fit with Guccione for Tho. at 48-hours incubation.